

Compound semiconductor layers for optoelectronic and photovoltaic purposes

PhD Thesis

Zsófia Baji

Supervisor:

Dr György Molnár

**Budapest University of Technology and Economics and
Research Centre for Natural Sciences, Institute for Technical Physics and
Materials science**

2013

Contents

I. Introduction	3
1. Motivation.....	3
2. Overview of the research field	5
2.1 Atomic Layer Deposition	5
2.2 Properties and preparation of ZnO layers	16
2.3 CIGS solar cells	23
3. Experimental methods	31
3.1 The atomic layer deposition system.....	31
3.2 Thermal evaporation and sputtering	32
3.3 Hall measurement.....	32
3.4 Spectroscopic ellipsometry	33
3.5 Microscopy	33
3.6 SNMS and XPS	34
3.7 XRD	35
3.8 UV-VIS transmittance spectroscopy	35
II. Results and discussion	36
4. Atomic layer deposition of Al doped ZnO layers	36
4.1 The structure and morphology of Al doped ZnO layers.....	38
4.1.2 The resistivity of the ALD deposited AZO layers	45
5. Nucleation and growth of atomic layer deposited ZnO layers	52
6. The growth of epitaxial ZnO layers	59
7. Deposition of CIGS layers with post selenization of the metallic components.....	66
7.1 The morphology of the evaporated metals	67
7.2 Post annealing of stacked metallic layers	70
7.3 Selenization of metallic components with Se vapour	73
7.4 Post selenization of flash evaporated metallic layers	77
Summary	82
Theses.....	84
List of abbreviations	87
Acknowledgement.....	88
References	89

I. Introduction

1. Motivation

Solar cells, as most members of renewable energy production, have recently been gaining a growing interest. Due to reports on global warming and energy needs the importance of developing new technologies in a cost-competitive way is the main motivation of thin film solar cells research.

As the visible light spectrum is between 1.6-3.4 eV, the active layer of a solar cell needs to have a band-gap not exceeding these values. A number of materials fulfil this requirement, and result in solar cells with various efficiencies and costs. The great advantage of thin film solar cells is that they have a low material requirement. The active layer of these devices has a thickness in the range of a few microns between two glass panes.

My theses focuses on thin films of two materials, both crucial for a number of photovoltaic applications: CIGS ($\text{Cu}(\text{InGa})\text{Se}_2$), which is the absorber material of one of the most promising thin film solar cell family, and ZnO, which is the most commonly used transparent electrode material. As a wide band-gap semiconductor ZnO is also important for a number of optoelectronic applications as well.

CIGS materials are one of the most popular members of the thin film solar family as they combine cost efficiency with stability and a reasonably good efficiency. (20% for CIGS in laboratory scale) [1.1]. They can be prepared with a number of methods, but the processes that result in the best efficiency cells are extremely complex. Therefore there is a perspective of improving the fabrication of such solar cells significantly by the application of more economical and simpler deposition methods. The post selenization of copper, indium and gallium precursors is one of the most promising new directions for chalcopyrite fabrication. This technique is extremely simple and no expensive apparatus is needed, as the process is defined by the stoichiometry, and the parameters do not require precise tuning.

ZnO is a material with a direct band-gap of 3.37 eV, an exciton binding energy of 60 meV, and a very high radiation and thermal stability. It is piezoelectric, and can even be ferromagnetic if doped with transition metals. Unfortunately, up to now the lack of good quality single crystalline ZnO has hindered the advances concerning this material, but recently epitaxial growth on GaN has renewed interest in it. On the other hand transparent conductive oxides are crucial for a number of optoelectronic and electronic device applications as well, due to their very high exciton binding energy (60meV) [1.2]. A few examples are as TFTs, LEDs, field emitters, and flexible electronic devices. This application would require the growth of high quality epitaxial layers, preferably with a tuneable band gap and resistivity.

Another excellent application for ZnO would be as the buffer layer in CIGS solar cells. Usually CdS is used as this thin film between the active layer and the window electrode, but it is highly toxic and environmentally hazardous. It is also very impractical as its wet deposition interrupts the vacuum process [1.3]. However, sputtered ZnO does not grow with the required conformity on the CIGS film, therefore the use of a buffer layer is indispensable. Atomic layer deposited (ALD) ZnO would be

a vacuum-compatible alternative, which even meets the requirements on conformality, uniformity and reproducibility.

In the case of organic and hybrid solar cells it is crucial that the transparent conductive electrodes are always within a diffusion length from the location where the charges were generated. This requires high quality transparent conductive oxide materials grown in a number of high aspect ratio and surface/volume ratio structures on a nanometre scale. ALD ZnO is a perfect candidate to fulfil this immensely high requirement.

The aim of the present work is therefore to examine the basic qualities and physical properties of thin films of two chosen materials: ZnO and Cu(In,Ga)Se₂.

- On the one hand to examine the basic physics of ALD deposited ZnO layers. The systematic investigation of Al doping and its effects on the conductivity is aimed, and the elaboration of novel structures from ALD ZnO for solar cell and opto-electronic purposes is targeted.
- On the other hand new, cheaper and simpler methods were tried to deposit the CIGS active material. One of the possibilities is the post-selenization method, that is, to anneal the CuInGa metals in Se atmosphere. This is an easily available method that enabled us to examine the processes and physical phenomena that take place during the selenization process of metallic precursors, and the required parameters of the absorber material.

2. Overview of the research field

2.1 Atomic Layer Deposition

Atomic layer deposition (ALD) is a self-limiting layer by layer growth method. It was invented by Tuomo Suntola et.al. [2.1.1.], and was first used for the deposition of epitaxial layers of compound semiconductors. Hence the original name of the method: atomic layer epitaxy. The low growth rate limited the applications at first, but with the further size reduction of semiconductor device dimensions the method gained a renewed interest. Nowadays it is considered to be one of the most promising thin film and nano-structure fabrication methods. Further improvements to the technique have made it possible to grow a huge number of compound materials and even elements can be grown. Also, due to a low growth rate and the governing chemisorption process, an epitaxial growth of a number of materials can relatively easily be achieved with the ALD method with a proper tuning of the growth parameters [2.1.2].

The operation principle of the technique is very similar to that of CVD growth: it is based on the introduction of precursor gases into the vacuum chamber, and their subsequent deposition on a heated substrate surface. The difference is that here the precursors are consecutively introduced into the reactor, and between the precursor pulses the reactor is purged by an inert gas. Therefore they can only react with the substrate surface and never with one another in gas phase, which prevents the formation of particles in the gas phase that could be adsorbed on the surface and build a granular film. The chemisorption on the heated substrate surface ensures a uniform and conformal coverage independent of the surface morphology. This means that any given aspect ratio substrate may be evenly coated by this method, in an ideal case even after just one mono-layer of deposition. As the surface reactions are self-limiting, one deposition cycle always forms only one mono-layer of the grown compound on the saturated surface. With the sequential repetition of the deposition cycles conformal and uniform films may form at an atomic layer control. The self-terminating characteristic of the method also means that the precursor fluxes need not be uniform, only a saturated chemisorption has to be achieved. At the same time the composition of the layer can be tailored under a nanometre scale [2.1.3].

The advantages of the ALD method

The versatility of the ALD method is especially important in micro-technology, where, due to the miniaturization, extremely thin films are required with their composition and uniformity controlled at an atomic level. Also in micro-technology complicated structures with extremely high aspect ratios need to be covered with continuous layers.

As a summary, the main advantages of the method are:

- conformal and uniform coverage
- possibility to coat high aspect ratio structures
- precise thickness and composition control
- easy and precise doping
- pinhole free layers
- easy scale-up
- low temperature deposition
- possibility of growing epitaxial layers

The ALD growth

Fig 2.1.1. explains the ALD process through the ALD sequence for ZnO deposition. The deposition steps are the following:

1. First, diethyl-zinc, the metalorganic precursor for Zn, is introduced into the reactor
2. It chemisorbs on the substrate surface, one of its C_2H_5 ligands reacts with the hydrogen from the surface OH groups, and thus the Zn connects to the oxygen.
3. Afterwards, an inert gas (typically nitrogen) purges the unreacted precursor residue and the ethylene out of the chamber.
4. Next, the oxidant (usually water vapour) is introduced. It reacts with the Zn on the substrate surface, giving a H ion to the other C_2H_5 ligand, resulting in a C_2H_6 molecule.
5. Then a final purging clears out the reactor and the result of the growth cycle is one mono-layer of ZnO [2.1.4].

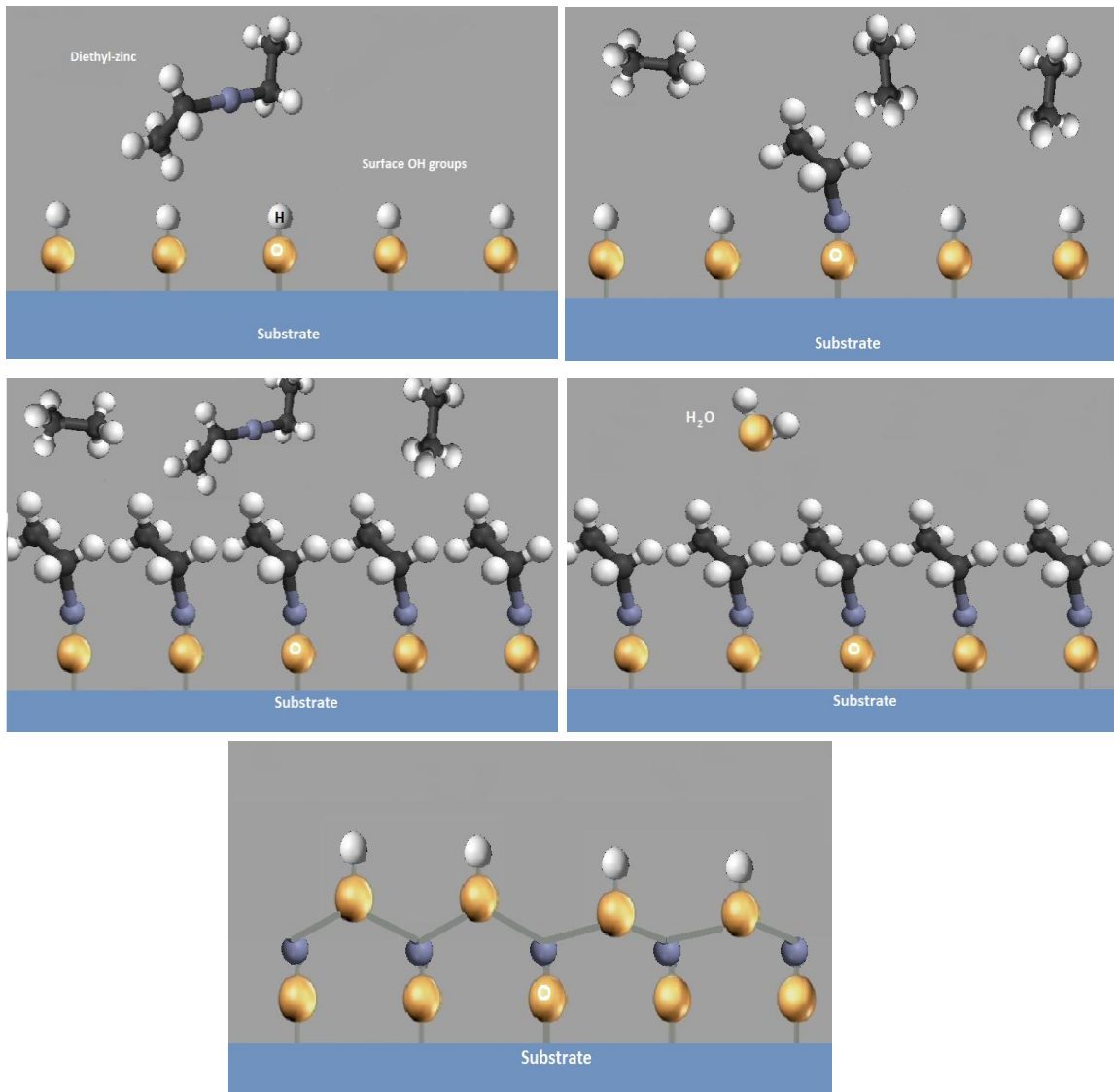


Fig. 2.1.1. The Atomic layer deposition cycles of ZnO

The tuning of the deposition parameters means the setting of the deposition temperature, the gas flow rates and purging times so that the growth rate is stable and constant. The purging times are especially important, because if they are not set long enough, the precursors meet in gas phase as well, and a CVD-like growth occurs.

The growth rate depends strongly on the deposition temperature. It affects both the number of adsorption sites on the substrate, and the quality of the chemical reactions that take place on the surface.

The range of the ideal growth temperatures is the so-called ALD window, which is shown in fig. 2.1.2. As the idea of the method means that only chemisorption is

possible, it is necessary that the adsorbates only form strong bonds with the surface. At the temperature of the deposition any bond between the adsorbate molecules has to be weak. At the temperature range below the ALD window the growth rate may increase with the temperature, if the precursors need an activation energy to form bonds with the substrate surface and each other. In some cases though, the growth per cycle decreases with the increasing temperature in the low temperature regime. This is due to a low temperature multi-layer growth by physisorption with the precursors simply condensing on each other. At too high temperatures once again the growth rate may increase or decrease with the temperature. In most cases it decreases as the adsorbed molecules now have enough energy to desorb again after adsorption. On the other hand an increasing growth may be experienced if the temperature is so high that the adsorbate molecules form bonds with each other, and particles form, which results in a higher than one molecular layer per cycle growth rate. In this case the deposition is not atomic layer controlled; this region is also called the CVD region [2.1.3].

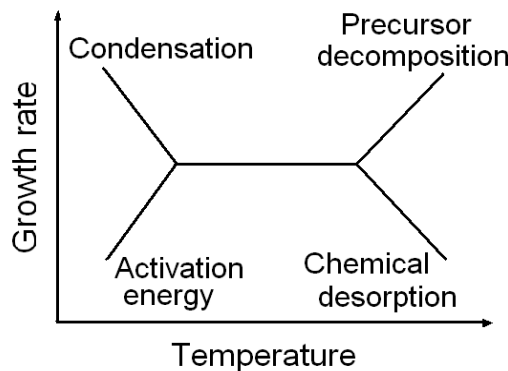


Fig 2.1.2. The ALD window of the ideal growth

Even within the ALD window, that is, within the temperature range where the layer growth is stable and self-limiting, the growth per cycle depends on the temperature. Increasing the temperature may decrease the growth rate, typically through decreasing the number of adsorption sites. The growth rate may also increase with the temperature if the higher temperature provides extra energy, which is then sufficient to overcome some barrier, and another type of reaction may start. The growth rate-temperature connection may be constant, if the available sites are not the limiting circumstances, but the steric hindrance is. The growth- temperature relation may also grow to a certain point, and then decrease. This is usually the case, if the typical surface reactions need a certain activation energy that can be provided by the heat, but by further increasing the temperature the available reactive sites start to decrease.

The morphology and the crystallinity of the layers are determined by the surface mobility of the material, through which also by the temperature, and the crystalline structure of the substrate. The choice of precursor materials only has an effect on these qualities in rare cases (e.g. TiO₂ films show superior qualities if deposited from titanium alkoxides). The crystallinity of the layers may be tuned with the

temperature ranging from amorphous to different crystalline structures (as in the case of -once again- TiO_2 which grows amorphous at low temperatures, then in anatase structure, and at temperatures above 300° as rutile). The crystalline orientation may also be influenced by the growth temperature. Polycrystalline film growth always results in rough films with a roughness in the range of nanometres and increasing with the film thickness [2.1.5].

Coating high aspect ratio structures

Atomic layer deposition is an outstandingly versatile method to coat arbitrary ultrahigh aspect ratio structures [2.1.6, 2.1.7]. Due to the chemisorption a full coverage can be expected over the whole surface, even at the bottom of high aspect ratio holes if the precursor exposures are high enough for all the reactant gases to diffuse into and out of the holes. George et al. [2.1.8] developed a model to describe the coverage of high aspect ratio structures by ALD. Using a Monte Carlo simulation they found that depending on the sticking coefficient and the aspect ratio, the coating of the pores could be diffusion or reaction controlled, which two cases lead to different coverage profiles. The process is reaction controlled if $S \ll H$, where S is the sticking coefficient and $H = 16(d/L)^2$, with d/L being the aspect ratio. In this case the holes are filled randomly and the reactants fill the space evenly before reacting. In the diffusion limited regime when $S \gg H$, the pores are filled up inwards from the opening of the pore with an abrupt boundary between the coated and uncoated parts, and the process is independent of the value of S . In this case the coverage has a $t^{1/2}$ time dependence. For the diffusion controlled case the minimum exposure times for the conformal deposition on high-aspect-ratio pores could be determined generally, and be applied to various ALD surface chemistries. The reactive sticking coefficients (the probability that an incoming molecule sticks to the surface) are $S=10^{-3}$ for Al_2O_3 , and $7*10^{-3}$ for ZnO . The expected exposure times for the case of DEZ are shown in fig. 2.1.3.a.

Fig. 2.1.3. b and c show my experiments on some high aspect ratio structures:

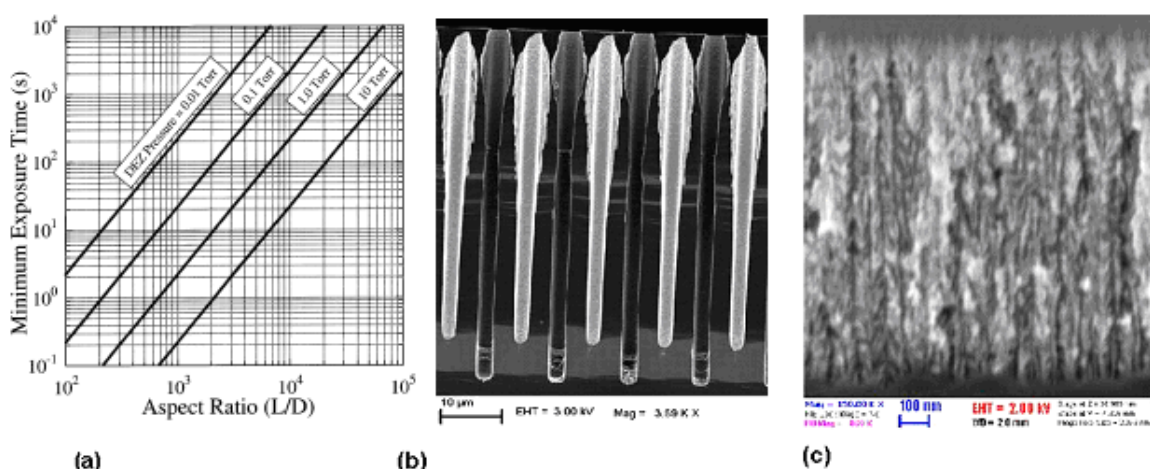


Fig. 2.1.3 a: the required exposure times vs aspect ratio, from [2.2.10]. b: DRIE

etched holes coated with 50 nm thick ALD ZnO, c: porous silicon with a typical pore size around 50nm, coated with 5 nm ALD ZnO

The growth rate

A common misunderstanding about the atomic layer deposition is that the growth actually takes place mono-layer by mono-layer, which would indicate a growth rate of one lattice spacing in each cycle. In the case of chemisorption controlled processes a mono-layer is generally defined as the amount of adsorbates that occupies all the available sites on the substrate surface. This means that the monolayer is considered complete if further growth is impossible, even if a full molecular layer of a crystal has not yet been grown. In reality the growth rate is almost never one full molecular layer per cycle. The ALD window and the tuning of the deposition parameters means that the reactant is in saturation, therefore the only hindering process is that of the chemisorption.

The chemisorption process itself must always be irreversible for ALD purposes, that is, once an adsorbate connects to the surface, it must not desorb again. The chemisorption may commence through three different mechanisms: Ligand exchange, where the reactant arrives at the surface, releases a ligand, and then further ligands get consumed via reactions with surface groups; dissociation, where a reactant molecule is split upon reaching the surface thus engaging two or more surface groups; association, when the reactive molecule forms a coordinative bond with a surface site without releasing ligands.

Two processes always hinder the chemisorption and define the saturation of the surface: the number of connecting sites on the surface, and the steric hindrance of the precursor molecules. The number of available sites on the surface might not be enough to achieve a full mono-layer of the grown crystal, or the adsorbate molecules might be so large, that they engage more than one connection site. A third hindering process that occurs at times is that bulky ligands of a chemisorbed precursor molecule get adsorbed on the surface, thus engaging bonding sites, and further hindering the growth by their steric hindrance. Nevertheless, the chemisorption coverage is considered complete, after a self-termination has been achieved [2.1.7].

The most detailed model describing the growth rates experienced during ALD depositon has been developed by Ylilammi [2.1.9], and considers both the adsorbate sizes, and a substrate surface structure. During the adsorption of the precursors their size and the available bonding sites define the maximum density of the adsorbate molecules. The latter depends on the crystalline structure of the surface. This can be very different in amorphous or crystalline substrates, but even the surface of crystalline samples experiences some reconstruction. The dislocations or impurities also influence the nucleation, while a roughness increases the area of the surface [2.1.10]. The precursors used in ALD processes are often large. We can assume that the adsorbates occupy the surface in the densest possible distribution. The packing density is the ratio of the adsorbed atoms to the adsorption sites occupied. This is the process through which the steric hindrance affects the growth rate. On the other hand the surface coverage may not be complete if the surface chemistry also hinders the process. Calculating the packing density is

straightforward according to [2.1.9]. As the molecules may rotate around the bonding sites, we may approximate their geometry with circles. The packing density depends on the ratio of the distance between the adsorption sites, and the size of the adsorbates. However, the first step of the adsorption, before the chemisorption, is when the molecules physisorb on the surface, therefore they cannot get too close to each other, as the repulsion between the adsorbates is stronger than the physisorption.

Due to the above-mentioned effects the growth per cycle in atomic layer deposition is always considerably less than a mono-layer. In fact a growth of 0.5 atomic spacing per deposition cycles is regarded as very high [2.1.10].

The nucleation is also a crucially important factor of the initial phase of the growth as the ALD process can only start if there are adequate chemical species to which the precursors may connect. If the surface is inert, the reaction may only start at defect sites and an island-like growth takes place at the initial stages of the film growth. Having the islands grown together a stable growth rate sets in, and a uniform layer-by-layer growth starts. Note, that in the initial stages of growth, in the first few cycles, the layers are not continuous. This phenomenon occurs when the reactants grow rather on the ALD-grown material, and not so much on the substrate. It has been reported for instance in the case of Al₂O₃ growth on Si and carbon surfaces, e.g. graphene [2.1.10]. Ref [2.1.11] also found agglomerates of ALD grown ZnS after the first few (~ 10) growth cycles, which then grew in size and then formed a continuous film with a very rough surface. A random deposition is also possible, where the landing of the adsorbate molecules is just as likely on the substrate as on the islands of the grown material.

During the first few cycles of growth the adsorption of the precursors is completely different from the later ones, as the reaction with the substrate surface might be different from the reaction with the material itself. Between these two there is a transient regime, where both the substrate surface and the ALD grown material surfaces are present. A substrate enhanced growth is possible if the substrate offers more reactive sites than the material surface, while in the case of substrate inhibited growth an island-like growth is also possible. In some cases the growth does not depend on this effect, and the growth rate is linear even in the initial phases of the growth.

The agglomeration of the adsorbed molecules can also occur if the system tries to minimize the interface energy between the two materials. In this case, after a mono-layer has been grown, the adsorbates can migrate and form islands. In fact, according to Ritala and Leskela this is a more likely explanation of the island-like growth in atomic layer deposition [2.1.5].

Another possible explanation is that during film growth certain intermediate species have a higher mobility on the surface, and they are responsible for the migration and the agglomeration.

Precursors in ALD

Precursor chemistry is a key question of ALD. The research is always active for new precursors, for example there is still no effective ALD process known for SiO₂

deposition. The deposition of elements is always complicated as well, as it is especially challenging to find precursors reactive enough to reduce to elements with chemisorption to a surface simply by thermal assistance.

The reactants used in ALD should be volatile at a reasonable temperature achievable with the ALD instrumentation, should not decompose at the reaction temperature, and they should perform chemisorption and a reaction on a heated surface. This means that an especially strong reaction between them and the surface must be possible. On the other hand, the surface reactions must also be complete, even at low temperatures, and no residues should remain on the surface. Also, the by-products of the surface reaction must be un-reactive so that they can easily be swept out of the reactor. In rare cases an etching may occur between the pulses, especially in the case of multi-layer structures where the precursor of one component may etch back the deposited layer of the other. Another negative effect is the dissolution of the precursors into the substrate of the ALD deposited material. These phenomena are detrimental to the film growth and must be avoided.

The precursors can be gases, liquids or solids. As the ALD process does not require a homogeneous or constant flux, the only necessary requirement is that they should have a large enough vapour pressure at the required temperature. The source chemicals used in ALD may be used at room temperature, if their vapour pressure is sufficient to provide the required flux. These are kept in vessels, from which the vapour is led into the reactor directly and pulsed with fast operating valves. The lower vapour pressure materials need to be kept in boosters and heated to the required temperature [2.1.12, 2.1.13].

Applications of the ALD method

The ALD method is the most popular for growing composites, especially oxide and nitride films, but elements have also been grown. Nitride and oxide films grown by ALD are becoming more and more popular for microelectronic applications, such as diffusion barriers, and the new generation of gate oxides also offers an ideal application for ALD oxides. The very thin -nano-scale- oxides with high dielectric constants, an extreme smoothness and an engineered band-gap deposited by this method can be reliable gate layers. For this purpose avoiding the oxidation of the silicon surface during deposition is an important issue that can easily be solved in an ALD reactor by avoiding the use of highly oxidizing precursors. Multi-layer structures might also be used as high-k dielectrics [2.1.12].

Nitride films can be used as diffusion barriers in IC fabrication. Most common are perhaps TiN and TaN. The majority of the nitride layers are deposited from metal chlorides and ammonia, in which case the extremely low growth rate is an issue. Elemental films, e.g. tungsten and copper can also be reliably grown with the ALD method. In this case reducing elements must be used as the other precursor. The material of choice for this role is generally hydrogen. For example Cu has been grown by a reaction of CuCl and H₂. As H₂ gas is sometimes not reactive enough at the substrate temperatures applied in ALD, atomic hydrogen must be produced by plasma or by thermal cracking. Plasma assisted ALD is highly reactive, and the deposition of numerous metals has been made possible by this approach. Even

metallic titanium and tantalum has been grown with this method at deposition temperatures of 25-400°C. The other possibility to enhance the growth of materials with a lower reactivity is by photo assistance, in which case the surface is enlightened with a UV source, and this gives the extra energy required for the chemisorption [2.1.12].

One great advantage of the ALD method is the deposition of high quality films at low growth temperatures. Due to the chemisorption the impurity concentration is expected to be quite low even at temperatures lower than 100°C. The heating of the substrate is important for all the surface reactions to take place, and the only disadvantage of the low temperatures is a slightly higher impurity level, but this is still low compared to CVD. Deposition of TiO₂, SiO₂ and Al₂O₃ films below 50°C has been reported in Refs. 2.1.14. and 2.1.15. The low temperature deposition is also advantageous as it makes the layer deposition on polymers and organic materials possible which could be a breakthrough for flexible electronics. The nucleation process on polymers is somewhat different from the conventional though, as there are no hydroxyl species on some polymer surfaces, therefore they do not have nucleation sites. The precursors in this case penetrate within the holes in the polymer and the nucleation then occurs on these absorbed molecules.

Another important characteristic of the ALD method is the ability to form nanolaminates easily. While depositing a composite material (e.g. an oxide) some precursor pulses have to be replaced by the dopant material. If the original was an ABAB pulse sequence, then the multi-layer can be fabricated following an (AB)_x(CD)_y sequence. The ratio of the x and y thickness of the two layers defines the composition of the multi-layer. If x and y are both large, we get an even multi-layer. If they are both small, the result will be a homogeneous alloy. However, if one is much larger than the other the film will be a slightly doped layer. On the other hand the deposition of compositionally modulated thin films can also be easily achieved with the ALD method. For example it is an ideal tool for the deposition of multi-layers for optics, where thin films with precisely controlled thickness and composition are required. Among the ALD grown materials dielectrics with a refractive index varying between 1.43 and 2.6 can be deposited, and even the growing films with graded refractive indices is fairly straightforward. Optical and X-ray mirrors have been made by ALD: In the soft X-ray wavelength range the layers have to be only a few nanometres thick, which is typically the challenge designed for the ALD method [2.1.16].

Due to the self-assembly characteristics of the process, ALD is an ideal tool for fabricating nano-structures. In this case the traditional approaches for lateral patterning need to be revised, but the ALD based nano-fabrication can easily be carried out with the use of nano-templates [2.1.17].

Due to the uniformity and the precise thickness control nano-coating is an excellent application for ALD [2.1.18]. Protective coating of nano-sized objects can be easily, reliably and reproducibly solved with the method. Min et. al. coated ZnO nano-rods with Al₂O₃ to protect them from contamination and corrosion. The nano-rods were 10-30µm long and 50-200 nm in diameter and they were covered with 45 nm Al₂O₃ uniformly [2.1.19].

The coating of nano-particles or nano-sized balls can be achieved with ALD, after which the particles themselves may be removed by an etching step, thus even hollow nano-sized balls can be made [2.1.20]. This method has an especially interesting application in the fabrication of three dimensional photonic crystals. These structures have a periodically varying dielectric constant, which results in the photons behaving somewhat like electrons in a crystal: a band structure is formed, in cases even with band-gaps, where photons cannot exist. 3D photonic crystals can be made by the self assembly of nano-spheres in an fcc order, and another material with a markedly different dielectric constant filling in the voids. The other approach is to make inverse photonic crystals, where the voids are filled with a high dielectric constant, and then remove the template nano-balls. Povey et.al. [2.1.21] fabricated photonic crystals with Al_2O_3 and VO_2 void filling between silica spheres. Covering nano-particles is even simpler in fluidised bed reactors.

ALD reactors

ALD reactors of a number of designs exist, but they all consist of a reaction chamber with a substrate holder in it, and precursor gas inlets. The pressure within the reactor may range between ultrahigh vacuum to atmospheric pressure depending on the reactor type and design.

In the case of an ultrahigh-vacuum reactor with molecular flow the reactants can be introduced into the chamber, and then removed with a pump that evacuates the reactor. This makes an economical utilization of the precursors possible, but the deposition is relatively slow. The other construction carries the precursors with a neutral gas, and between the pulses the reactor is also purged with this inert gas. These are the flow type reactors, which are usually preferred in industrial use as the deposition is incomparably faster with them. They usually operate under viscous flow conditions. In both reactor types it is crucially important for the walls of the reactor to be uniformly heated, as the precursors may adsorb on cold spots, which makes the purging or the evacuation a great deal harder. The carrier gas used in the reactors is an inert gas, usually nitrogen that has to be at least of 5.0 (99.999%) purity, as this is the main impurity source in the deposition.

Most reactors, especially for research purposes, are open tubular chambers, in which any type of substrates may be placed and arranged arbitrarily. The batch reactors on the other hand are usually designed in travelling wave arrangement. In this design the substrates are placed parallel with each other, with just a narrow space between them. The pulsing is then synchronised with the evacuation of the reactor so that the precursor pulse travels over the substrates like a wave front, and before it is pumped out of the reactor, the next pulse follows behind it with a purging wave between them. In this design the precursor molecules collide with the surfaces multiple times, and the substrates become saturated very quickly. This allows a very fast and cost efficient use. There is also another reactor design: that of the flow type reactors with moving substrates, where the movement of the substrates is synchronised with the precursor pulses.

The deposition of the precursors on the surface is usually helped with a heating of the substrate. This method is called thermal ALD. In cold wall reactors only the

substrate is heated, in hot wall reactors the whole chamber is heated to the deposition temperature. In the cases when the thermal energy is not enough to ensure the reaction of the precursors on the surface, the reaction may be assisted by a plasma source.

The scale up of the ALD process is very easy as only the saturation of the precursor gases need to be ensured, the laminar flow needs not be considered in the design. Therefore batch reactors are already available in the market [2.1.3, 2.1.5].

2.2 Properties and preparation of ZnO layers

Wide band-gap semiconductors (e.g. GaN) are very suitable for the purposes of high power, high temperature electronic devices and short wavelength opto-electronics. In fact, they may even be more suitable for these purposes than GaAs due to their superior qualities: they tend to have larger electron mobility, and higher breakdown field strength. ZnO is a material with a direct band-gap of 3.37 eV, which means it is still transparent in UV light. On the other hand its exciton binding energy is 60 meV, which increases the luminescence efficiency. (In comparison, the exciton binding energy of GaN is 25 meV.) The room temperature Hall mobility can be as high as 200 cm²/Vs in mono-crystalline samples whereas the carrier concentration in the intrinsic case is typically in the order of magnitude of 10¹⁵-10¹⁸ /cm³. ZnO also has a very high radiation and thermal stability. It is piezoelectric, and can even be ferromagnetic if doped with transition metals. For opto-electronics applications good quality single crystalline ZnO would be crucial, therefore the epitaxial growth on GaN has recently renewed interest in this material [2.2.1].

ZnO grows in a hexagonal wurtzite, rocksalt and zincblende phases, but only the first is stable, the second only under high pressure, while the third only grows on cubic surfaces. The lattice parameters of the wurtzite ZnO crystal structure are $a=3.25$ Å and $c=5.12$ Å. The bond between the Zn and O atoms is an sp³ covalent bond, but it is also highly ionic, and is in fact on the boundary between the two bonding types. Each Zn²⁺ ion is surrounded by four O²⁻ ions, which is the typical tetragonal arrangement of an sp³ coordination. The structure of the hexagonal ZnO is polar, which is also the reason for a number of properties of the material, such as its piezoelectricity. The anisotropy of the hexagonal crystal yields a number of interesting physical properties in ZnO as well. The anisotropic optical properties result in a uniaxial birefringence with two refractive indices parallel and perpendicular to the c axis [2.2.2].

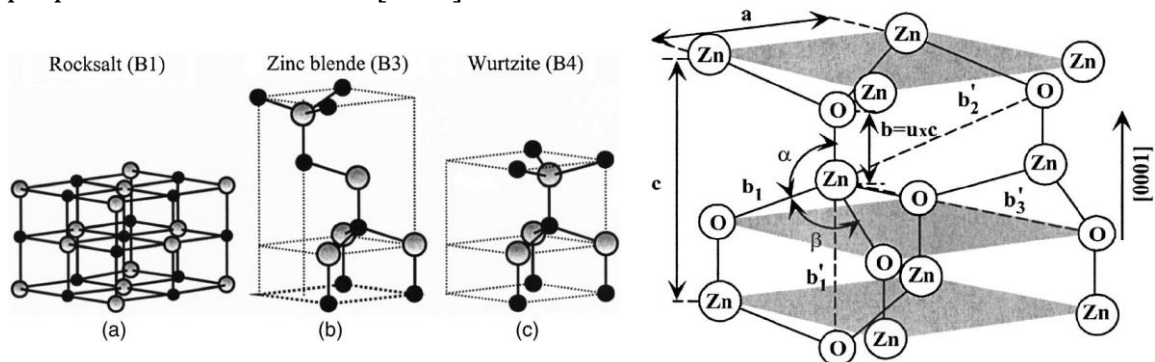


Fig. 2.2.1 The possible crystalline structures of ZnO (a,b,c) and the details of the wurtzite structure [2.2.2]

It can have three very different types of surfaces: it can either be terminated by O ions or Zn ions, or by a non-polar surface with the same amount of O as Zn. The

different surfaces have different chemical properties that also determine the growth along these directions. The Zn atoms on the Zn-terminated surface start to sublime at a temperature as low as 380°C, whereas the O terminated surface remains stable up to 600°C. This latter surface also has a different electronic structure from the other two.

ZnO has been grown by a number of methods on various substrates, e.g. Si [2.2.3], glass [2.2.4], diamond [2.2.5], sapphire [2.2.6] and GaN [2.2.7]. Epitaxial growth has also been found possible by some methods, including RF magnetron sputtering [2.2.8, 2.2.9], pulsed laser deposition [2.2.10], molecular beam epitaxy [2.2.11]. Epitaxial ZnO films are extremely important for a number of applications, such as ultraviolet light emitters [2.2.12], and even room temperature pumped lasing has been shown [2.2.13]. In most cases the epitaxy is attempted on sapphire substrates, mostly in the (0001) direction, despite its poor structural and thermal match to ZnO (18.4% in plane lattice mismatch). Therefore, the layers grown on sapphire always have a high degree of mosaicity and high carrier concentrations combined with a low mobility. GaN promises to be a more suitable substrate for ZnO heteroepitaxy with a hexagonal crystalline structure and a lattice mismatch of only 1.8% (lattice parameters of GaN are: $a=3.189$ and $b=5.185$). The ScAlMgO₄ substrates also have a very small mismatch to ZnO (only 0.09% in the ZnO(0001)||ScAlMgO₄(0001) direction) [2.2.2]. As the growth of high quality ZnO single crystals is possible with hydrothermal-, vapour phase- and melt growth, the homoepitaxy on ZnO is also a possibility, but the single crystalline substrates are extremely expensive. Homoepitaxial growth has been proved to be possible on both polar surfaces of the material. In this case one has to pay attention to the polarity of the surface, as the O-terminated surface is more stable, therefore it is a more suitable substrate for layer growth [2.2.14]. Polycrystalline layers have often been grown on Si (cubic structure with $a=5.43$)

ZnO has a direct band-gap. The p-like valence band is split in three sub-bands due to crystal field- and spin-orbit interactions, the top band comes from the O 2p band; the lower ones come from the Zn 3d states. The conduction band of ZnO is s-like: the lower conduction band states originate in Zn 3s levels, and are strongly localised, the higher ones are free electron like [2.2.1].

Band-gap engineering is of crucial importance in the development of semiconductor devices. The electrical properties of ZnO can vary within a very wide range from conductor through semiconductor to insulator depending on the deposition method and parameters. The carrier concentration can be anything between 10^{15} and $10^{20}/\text{cm}^3$. The latter is the highest reported n-type doping. On the other hand no reliable p-type doping has so far been reported [2.2.15].

There are two intrinsic dopants in ZnO: oxygen vacancies and Zn interstitials. Oxygen vacancies have lower formation energy than Zn interstitials, therefore they are more common [2.2.16]. In the case of a Zn rich growth environment, oxygen vacancies are predominant, while under O rich conditions Zn vacancies dominate. Hydrogen always acts as a donor in ZnO. It binds to an O and forms an OH. These three are the most common defects and the sources of unintentional doping in ZnO, and they result in the n-type intrinsic conductivity of the material. Which of the

three dominate the conduction is still a question for debate. Theoretical calculations suggest that the O vacancies and Zn interstitials would give deep levels, and only the H doping can produce the shallow donor levels associated with n-type conductivity [2.2.17-2.2.19].

The most widespread approach to increase the n-type conductivity of ZnO is by doping with trivalent atoms -e.g. Al, Ga or In- that substitute a Zn atom in the lattice, or by group VII elements in the place of O atoms. The record conductivities are in the range of $10^{-4} \Omega\text{cm}$ [2.2.20].

P-type doping in ZnO –just like in GaN- is extremely hard to achieve. The reasons are the same as in the case of most wide-band-gap semiconductors. The p-dopants are compensated by the above mentioned n-type native defects, or the unintentional hydrogen dopants. Another problem is the low solubility of most p dopants in the material. The candidates for p-type doping are group I elements in the place of the Zn atoms and group V elements in O sites. The latter seem more promising, as they cause shallower levels, but due to their size they tend to be placed in interstitial sites rather than substitutional ones [2.2.15].

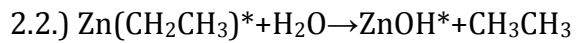
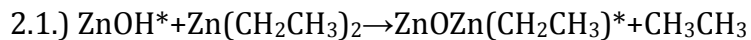
Another limiting factor for the manufacture of ZnO devices is that although Ohmic contacts are easily obtained, the fabrication of Schottky-type contacts on n-type ZnO is still an issue. For this purpose the most probable candidate is Pd, as predicted by the theory and as shown by the experiments of Grossner et al. [2.2.21].

A number of different nano-structures have already been grown on ZnO, e.g. Nano-wires and nano-rods, but it is evident that the ALD method still offers still a wide range of possibilities to grow any number of structures.

The atomic layer deposition of ZnO

The method for the atomic layer deposition of ZnO films has long been known. The metal-organic precursors can be dimethyl-zinc or diethyl-zinc, the oxidant is usually water vapour, O₂, or ozone. All the combinations of these reactants have excellent self-limiting ALD mechanisms. ZnO layers have been found to grow well with ALD between 100-400°C, but a growth already at 80°C has also been performed. The growth rate appears to depend on the used precursors and the deposition temperatures as well, but it has never exceeded the value of 0.2 nm/cycle [2.2.22].

The atomic layer deposition of ZnO occurs along the following reactions:



where the * means surface species [2.2.23].

According to the literature, the crystalline structure and orientation of intrinsic ALD ZnO depends on the deposition temperature and the substrate. Epitaxial layer growth of ZnO was reported on GaN and sapphire [2.2.24, 2.2.28], but most ALD deposited ZnO layers are oriented polycrystalline layers, as is the case of Si and glass substrates. Some authors have also noted that the polycrystalline films have a preferential crystallographic orientation, which may even depend on the deposition temperature, but there have been some controversial results on the exact nature of this dependence. The crystalline structure can most easily be described with X-ray

diffraction (XRD) measurements [2.2.22, 2.2.28-2.2.32]. In theory a perfectly non-oriented ZnO powder sample has the highest intensity XRD peak in the (101) crystalline orientation. The (100) and the (001) directions also appear in the diffraction patterns of ZnO samples. The (100) direction corresponds to the arrangement with the c axis parallel to the surface; while the (001) means that it is normal to it.

There is a slight discrepancy in the literature about the dependence of the orientation on the deposition temperature. According to references [2.2.28, 2.2.31, 2.2.32], the preferential orientation of the c axis changes from parallel to perpendicular to the substrate with increasing deposition temperature, while according to refs. [2.2.22, 2.2.29] it changes from perpendicular to parallel. The other big gap in the literature is the lack of data on how the doping affects the crystallographic structure and orientation, as no detailed XRD experiments have been conducted on the subject so far.

The films grown with H₂O as oxidants generally contain more oxygen than those deposited with ozone. If the deposition temperature is increased in cases with H₂O as oxidant, this effect decreases rapidly. According to ref. [2.2.33] this is due to the fact that at higher temperatures less surface OH groups persist, as above 200°C their thermal energy exceeds the energy needed to desorb from the surface. At higher temperatures the purging of residual H₂O is also more effective. The films grown with the use of ozone have an increasing O ratio built in with the increasing temperature due to the stronger oxidation of the diethyl-zinc molecules. Since the higher oxygen concentration means a lower carrier concentration, the resistivity of the layers grown with O₃ is 10-10³ times higher than that grown with water vapour. According to the available literature the resistivity of intrinsic ZnO decreases monotonically between 100°C and 200°C growth temperatures. Surprisingly, in this range both the electron mobility and the carrier concentration appear to decrease at the same time, although generally increasing concentration is associated with decreasing mobility. The reason for this opposite effect in ALD ZnO may be the consequence of the improved crystal structure of the layers obtained at elevated deposition temperature [2.2.22, 2.2.29-2.2.32].

Schuisky et. al. [2.2.34] examined the film growth during ZnO deposition with in situ resistivity measurements with contacts fabricated on the substrate in Van der Pauw geometry, and measured the resistivity changes during layer deposition. They found that it monotonously decreased with the increasing thickness up to about 50 nanometre film thicknesses. Also, the resistivity varied cyclically between the deposition cycles. It increased at every diethyl-zinc exposure and decreased after every water pulse. This may be due to the difference of the surface conductance with different adsorbates chemisorbed on the surface. As a DEZ molecule is chemisorbed at the surface, due to Eq. 2.1. the surface OH groups are transformed into Zn-alkyl groups, then after the water exposure the original OH coverage returns. That is, the OH-terminated surface has a much lower resistivity than the ethyl-terminated one.

ALD grown ZnO films have a very low intrinsic resistivity of ~10⁻² Ωcm, also depending on a number of deposition parameters. This low value is believed to be the result of the presence of Zn interstitials, oxygen vacancies and hydrogen

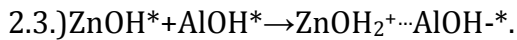
contamination [2.2.16-2.2.19]. This resistivity can be further reduced by two orders of magnitude at the most by Al doping [2.2.20, 2.2.23, 2.2.35-2.2.39].

Al doped ALD ZnO

The ALD grown ZnO can easily be doped with a number of materials, e.g. Al₂O₃, and multilayer structures can also easily be grown from these compounds. Composite thin films have long been the focus of research, as the refractive index, dielectric constant, lattice parameter and a number of other physical properties may be controlled by alloying two different materials. The composite material can also be fabricated as multilayers of the two constituents, which is quite straightforward with the ALD method. The doping and alloying of ZnO layers with Al with the ALD method has been examined by quite a few groups [2.2.20, 2.2.23, 2.2.35-2.2.39]. The doping of ZnO with Al by ALD occurs with inserting Al precursor pulses among the DEZ and the water pulses. The Al pulses are of course followed by water pulses, which raises the question if the Al is then built in as Al₂O₃, or the Al alone is placed as a substitutional dopant into the Zn location of the crystal. That is, is the resulting layer an alloy of the two oxides or an Al doped ZnO layer?

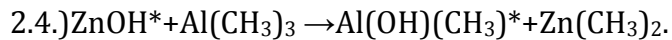
The growth of ZnO and Al₂O₃ layers is an interesting issue. The growth rate of ZnO is around 0.2 nm per cycle according to literature values, while that of Al₂O₃ is around 0.1 nm. Still, a multi-layer or an alloy of these two has much lower growth rates, as both materials have nucleation issues, and when the pulse sequences are changed, one has to nucleate on the other. Experiments have shown that after an Al₂O₃ pulse the growth rate of ZnO is much lower, and the same applies to the Al₂O₃ growth. The Al₂O₃ growth has a short nucleation period. It changes from 0.1 to 0.13 nm growth rate in 25 growth cycles. The ZnO on the other hand increases from 1.5 to 2 nm growth /cycle in 700 growth cycles. The surface chemistry of both materials is ruled by the hydroxyl coverage of the substrate. The hydroxyl coverage of amorphous Al₂O₃ is 0.94*10¹⁵/cm², that of (100) ZnO is 1.06*10¹⁵/cm², both defined at 177°C. The DEZ molecule reacts in average with 1.37 and the TMA with 1.47 hydroxyl groups at the surface [2.2.37].

George et. al. [2.2.37] measured the Zn content of the deposited alloy layers, and found that it was way below the expected value. They found that for example in the case of 50% ZnO and Al₂O₃ ratio the growth rates of the two materials were way below the intrinsic values: 27% and 67% of the corresponding ZnO and Al₂O₃ values. When the two materials have to nucleate on each other, the nucleation of ZnO lasts for about 6 cycles after each TMA pulse, and 2-3 TMA pulses are required after each DEZ pulse for the Al₂O₃ to nucleate. These could be the results of a smaller amount of surface reactive sites. But, as shown above, both the hydroxyl coverage and the reaction type of the two surfaces is similar, therefore the reduced growth cannot be a result of the lack of OH species. One explanation might be that the relative acidity of the two surfaces is different, and the following reaction may occur:



In which case the ZnOH₂⁺...AlOH⁻ complex formation results in less reactive OH species left on the surface.

Besides the nucleation problems another effect decreases the growth of the ZnO-Al₂O₃ alloys and multilayers. In the ZnO concentration range of 75-85% even negative growth rates can be experienced, that is an etching for ZnO. During in-situ quartz crystal microbalance measurements it was found that the etching always occurred during the TMA exposure of the layer, when the thickness decreased as much as one deposition/cycle. The explanation for the phenomenon is the following surface reaction:



The loss of mass predicted by this agrees reasonably well with the experimental results.

The literature has reported an etching of metals in atomic layer deposition before as well, for example in the case of TaCl₅ and Ta₂O₅ films, or Sr(thd)₂ with the SrO surface, etc. ZnO is also etched by a CH₄ plasma. In the case of the Al₂O₃ doping the CH₄ from the TMA and the hydroxylated ZnO surface reaction abstracts a Zn and forms Zn(CH₃)₂. On the other hand the donating of CH₃ groups from the Al to the Zn can also occur directly. The third etching effect can be the formation of ZnAl₂O₄ spinels.

Many authors have examined the effect of the Al doping and the temperature on the resistivity of ZnO layers, but only one or the other, or just in a limited temperature or doping range. No comprehensive study has been conducted yet about the effectiveness of the doping at different temperatures.

It was reported that the lowest resistivity could be achieved with Al content between 1 and 5 at%. At higher concentrations the mobility decreases, but the layers maintain their conductivity up to Al concentration as high as 10 at%. Between 10 and 16 at% the resistivity increases again, and small Al₂O₃ grains are formed in the layers. The crystallinity of the doped ZnO deteriorates, they may even become amorphous. Although it has been suggested that the doping efficiency may correlate with the ALD growth temperature [2.2.35, 2.2.38, 2.2.39], no detailed investigation was conducted on the subject so far.

Many groups have examined the effect of post annealing on the conductivity and the structural and morphological properties of the ALD deposited ZnO layers. It has been established that the post annealing results in a more uniform distribution of the Al doped sub-layers along the depth profile of the layers. However, the thermal treatment tends to increase the resistivity of the films. The most probable explanation is that the residual oxygen always present in every vacuum system diffuses into the layers and neutralises the intrinsic dopants. The oxygen vacancies quite obviously, but the hydrogen donors may also be engaged by the oxygen. If on the other hand the annealing was performed under some kind of capping layer an enhanced conductivity could be achieved [2.2.40-2.2.43].

The effect of the Al doping on the crystallinity and the orientation of the layers has not been examined yet. The effect of grain boundaries in the conduction process, or whether the conductivity may be in connection with the orientation of the layers has not been examined either, despite the fact that it is known to have an effect on the resistivity of sputtered layers [2.2.25]. It has been reported in a number of works [2.2.22, 2.2.28, 2.2.29, 2.2.31, 2.2.32] that the orientation of the ZnO layers depends

on the deposition temperature. This implies that the columnar crystallites of the layers either stand normal to the surface, or lie parallel to it. This means completely different grain boundary conditions, and if the conduction is in connection with the grain boundaries, this must also have an effect on the resistivity as well.

2.3 CIGS solar cells

$\text{Cu}(\text{In},\text{Ga})\text{Se}_2$ materials are one of the most promising members of the chalcopyrite family, due to their high absorption coefficients (10^5 cm^{-1}), long term electrical and thermal stability and outstanding stability against photo-degradation. They have the highest efficiency among the thin film technologies [2.3.1]. The most important chalcopyrite compounds for photovoltaic applications are $\text{Cu}(\text{In},\text{Ga})(\text{S},\text{Se})_2$, which is an immensely complex system, of which we have a surprisingly low level of understanding compared to the achieved technological level. Most qualities (e.g. morphology, electronic structure and band diagram) of this material have been experimentally set to achieve the best efficiency, while a complete understanding of them is still missing.

CIGS based thin film solar cells can be deposited on a number of substrates. Most commonly used is a glass sheet but recent attempts have been made to deposit chalcopyrite solar cells on flexible substrates. These efforts resulted in cells with efficiencies as high as 17.6% [2.3.2].

The components of CIGS solar cells

Thin film solar cells can be built up in superstrate or substrate configurations. In the case of a superstrate layout the deposition starts with a substrate, on which the transparent contact layer is deposited, followed by the buffer layer, the absorber, and finally the back contact. This method is the less common one, as it yields solar cells with lower efficiencies. The reason for this is the inter-diffusion of CdS and CIGS during absorber deposition [2.3.4].

The most widespread configuration is the substrate configuration shown in fig. 2.3.1.

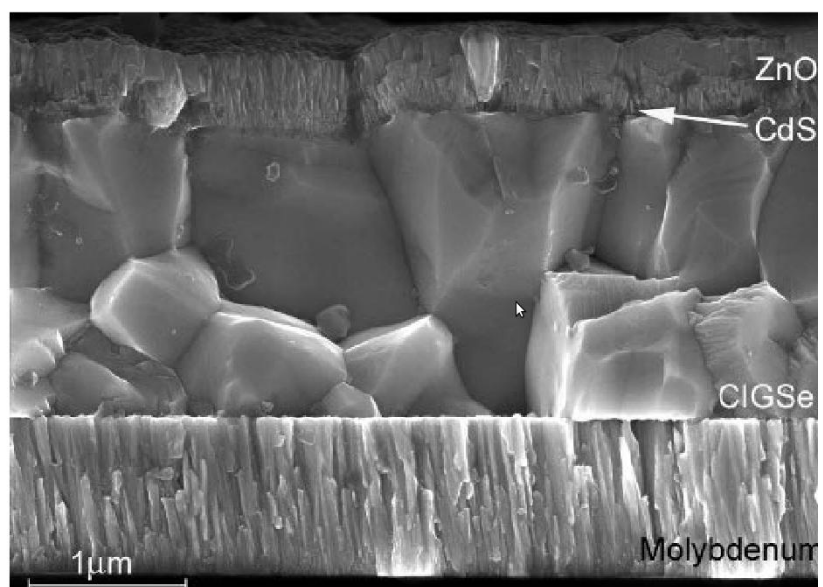


Fig. 2.3.1 The cross section of the CIGS film deposited in substrate configuration [2.3.]

In the substrate based structure the back contact electrode of the cell is first deposited on the substrate. This is usually a Mo layer, a highly conductive material that can conveniently and highly reproducibly be deposited by sputtering. On the back electrode, the active layer, the p-type CIGS film is deposited. On top of this layer an n-type buffer layer is deposited, followed by the transparent conductive front contact, which is most generally Al doped ZnO prepared by sputtering [2.3.5].

The most commonly used substrate is soda lime glass, with a thickness usually between 1 mm and 3 mm. The choice of material is crucial: experiments have shown that the sodium content of the substrate material is indispensable. The Na diffusion from the substrate into the absorber layer increases the carrier concentration and also alters the structure of the layer: it yields a larger grain size and an overall better layer morphology. It increases the composition range tolerated by the structure, assists the selenization and changes the defect distribution by neutralizing deep level donors, thus increasing the p-type conductivity [2.3.6]. The Na diffusion into the absorber is independent of the qualities of the Mo layer.

The back contact is most commonly molybdenum, on which the active CIGS material grows uniformly, forming an ohmic contact. The qualities of the Mo layer can also greatly depend on the deposition parameters, and thus a number of the properties of the resulting cells can be tuned. Mo films deposited at a low Ar background pressure have low resistivities but possess compressive stress and a weak adhesion to the substrate. With the increasing pressure, the resistivity increases and a tensile stress appears. The layers deposited at high pressure have an excellent adhesion and at the same time smaller grains, but are also more porous than low pressure ones. Due to their morphology they offer more nucleation sites for the absorber layer, which ultimately results in a better absorber adhesion and smaller, less faceted absorber grains. To combine the good qualities of the different deposition methods Scofield et. al. [2.3.7] developed a bilayer process with the deposition of a thin Mo layer at high Ar pressure immediately followed by a thicker one at low background pressure. This way it was possible to achieve low resistivity films with a good adhesion, which were then used in the best efficiency solar cells.

Between the active layer and the front electrode the buffer layer has a number of different roles. It is supposed to fit the lattices to each other and set the proper band offsets. It is also widely believed to prevent recombination at the interfaces. The buffer layer is usually CdS which offers a perfect n-type match to the p-type CIGS. There are attempts to replace this material with others, because of the high toxicity of cadmium. Furthermore, as this film is deposited by chemical bath deposition it requires the interruption of the vacuum process. Intrinsic ZnO is one of the leading candidates for this purpose, but it has to cover the CIGS layer very uniformly, therefore special deposition methods are required. Atomic layer deposition promises to fulfil all these requirements [2.3.8].

The CIGS absorber layer

The most important chalcopyrite compounds as absorber layers for photovoltaic applications are Cu(In,Ga)(S,Se)₂. By combining these components, a wide range of lattice constants and band-gaps may be achieved. The lattice constant of CIS

(CuInSe₂) is 0.58 nm, its band gap is 1 eV, those of CGS (CuGaSe₂) are 0.56 nm, and 1.7 eV. Thus the material qualities and the band gap of the absorber material may be tailored between these values even along the depth profile of the layer. The band gap corresponding to highest efficiencies achievable with a given method is 1.2 eV, which can be realized with a Ga/(Ga+In)=0.3 ratio. Above this ratio the quality of the films starts to decrease [2.3.9].

Although CIGS technology is not as sensitive to stoichiometry as Si based technology, still, the quality of the CIGS film depends largely on the exact composition of the layers. The CIGS material is doped p-type by native defects. The most important defect is the (2V_{Cu},In_{Cu}) complex, which is a stable defect providing a shallow acceptor level. This means that a slightly Cu poor composition is actually advantageous, and the CIGS material needs to be deposited copper deficient. Therefore the atomic ratio of the metals has to be between 0.88<Cu /(In+Ga)<0.95 and Ga/ (In+Ga)=0.3. Although a few percents of difference from this exact molecularity may still result in functioning layers, the films with various compositions differ in many qualities, most importantly in their performance. As mentioned before, the Na incorporation also increases the range in which the molecularity may change and still yield fairly high efficiency solar cells: The ratio of (In+Ga)/(In+Ga+Cu) may vary between 0.52 and 0.64 in the presence of Na [2.3.10].

Copper rich films have a larger grain size, caused by a segregation of CuSe at the grain boundaries, which has a low melting point and thus serves as a fluxing agent promoting the growth of large, closely packed crystallites. On the other hand, In rich layers have better electrical qualities. The bilayer process combines these advantages by depositing a Cu rich layer under a Cu poor one [2.3.11].

Manipulating the Ga content of the layer gives another possibility to engineer the qualities of the layer through its depth. Increasing the Ga/In ratio towards the depth of the layer results in a wider band gap near the back contact, which ultimately gives a higher open circuit voltage (Voc) and fill factor. At the same time it is crucial that the band gap is wide near the active region of the p-n junction, so that high-energy photons can still generate electron-hole pairs. The optimal band gap grading is defined by the optimum of these effects [2.3.12- 2.3.13].

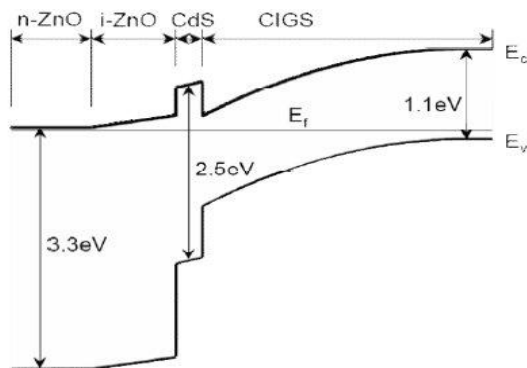


Fig. 2.3.2. The band diagram of a CIGS solar cell [2.3.]

An interesting aspect of the details of the deposition is the sensitivity of the films to

their orientation. Not only the morphology but even defect formation depends largely on the crystallinity of the absorber layers. The most common orientations found in CIGS films are the (112) and (220/204). The (220/204) orientation has been observed as more prominent in the record efficiency absorber materials as it has a lower ratio of non-radiative recombination centres. This crystallinity can be achieved with a Se overpressure, or a higher Se flux, with the substrate type Na and Cu content also playing a part in the resulting orientation [2.3.14, 2.3.15].

The highest reported conversion efficiency for CIGS solar cells is beyond 20% for laboratory scale cells [2.3.16]. This result has been produced by an inline co-deposition method, where all the compounds are co-evaporated from individual sources. This is the technique promising the best quality cells, but also the most complex one possible, in which the precise control of all the parameters e.g. substrate velocity, temperature and composition profiles is necessary.

Deposition methods

The co-deposition method is often performed as a sequence of deposition processes, where the concentration of the components varies with time. During evaporation the Se is always in excess, but the Ga/In ratio can be changed during the process thus tailoring the band-gap throughout the depth of the layer. Changing the copper content also changes the growth kinetics of the film. The bilayer process unites the advantages of the Cu poor layers on the electronic structure and the Cu rich layers on the morphology. The deposition starts with a relatively Cu rich layer, which gives larger grain size and an overall better film morphology, and ends with a Cu poor layer, which ensures the optimal electrical qualities. The inverted process is the same reversed. The three-stage method begins with the co-evaporation of In, Ga and Se, which results in a very smooth base layer. This is followed by an exposure to Cu and Se in the second stage, until a Cu-rich composition is achieved, and then additional In, Ga and Se are supplied to adjust the precise film composition and give a smooth layer surface [2.3.17].

Besides co-evaporation there is a number of other processes to fabricate CIGS films such as selenization of the precursors with Se vapour [2.3.18-2.3.34], H₂Se or diethylselenide [2.3.33,2.3.35], the rapid thermal processing of co-deposited or stacked multi-layer precursors [2.3.36], spray pyrolysis [2.3.37], flash evaporation [2.3.38], RF sputtering [2.3.39], electrodeposition [2.3.40], chemical bath deposition [2.3.41], etc.

The two step method for CIGS preparation

The two-step method means the deposition and post-selenization of the metallic components, and is a promising method for low cost, large scale manufacturing of solar cells. It is fairly simple, and does not require expensive apparatus or a very precise control of the parameters, as the thus created layers are not as sensitive to the growth parameters as the ones grown with one-step methods. Still fairly high efficiencies can be achieved with this approach. Films prepared with this method have efficiencies smaller with a few percents than the record ones on the laboratory scale, but once the one major difficulty of scaling up has been avoided, these

differences are significantly smaller. Siemens solar uses this preparation method, and they have achieved modules with 15% efficiency [2.3.18].

Selenization can be carried out on the copper-indium-gallium layer thus creating CIGS material, or on the other hand the quality of the already deposited CIGS material can be largely improved by a selenization with simultaneous annealing. A post-deposition thermal treatment in Se atmosphere improves the film stoichiometry and the structure [2.3.26].

Selenization is usually achieved by the use of Se vapour, or H₂Se. The latter is highly toxic, therefore its application raises environmental and health concerns. It is usually stored in high pressure cylinders, so its handling is somewhat complicated. There have also been successful recent attempts of selenization with diethylselenide [2.3.26, 2.3.27].

Paradoxically, the Se content of the layers is not always increased by selenization. The reported decrease of the Se content during selenization due to the outdiffusion of Se can be avoided by a very rapid ramp up [2.3.19].

The metals can also be deposited on the substrates by a number of methods, evaporation and sputtering being perhaps the most common. A paste coating of the metallic components [2.3.20] or a metallic ink coating with a post selenization [2.3.21] are two of the unconventional methods that provide a simple non-vacuum process for absorber preparation, although the device efficiencies do not exceed 10 % at the moment. The problem most often associated with these methods is that the paste quality seems to be poor. The homogeneous mixing of the different metals within the powder and the milling of sufficiently small particles without contaminating the materials has yet to be solved. Current efforts are aimed at dissolving nano-sized particles in the fluxing agents [2.3.22] or the milling of alloys of Cu, Ga and In, which are more brittle, therefore a more homogeneous powder with smaller particle size can be made from them [2.3.21].

There have been a number of studies on the processes that take place during the selenization of Cu, In and Ga, but no full description has been given yet. Most studies examine the process by ex-situ methods [2.3.22], but there have been certain attempts for the in situ characterization of the CIGS formation. Liu et al [2.3.34] used in-situ electrical resistance measurement, while Kim et al. used time-resolved high temperature XRD [2.3.35]. There is no detailed analysis of the diffusion of Se in the metallic components, and the influence of a number of parameters such as time, pressure and heating method on the diffusion is not yet understood. However, from the work of Kim et. al., it appears that the formation of both CIS and CIGS materials is a one dimensional diffusion controlled process with a nucleation and a subsequent growth step. The growth kinetics consists of the growth of a CIS or CIGS layer on the surface of the material, which then limits the diffusion speed. The process was estimated both with the Avrami and the parabolic rate growth model and an activation energy of 100-130 kJ/mol was found for the CuInSe₂ formation.

Several studies address the chemical reactions that take place in the process. It has been established that if the temperature during selenization is reached through ramp annealing, the formation of the binary and ternary composites follow a certain

order. First the metal alloy phases form (e.g. CuGa₂, Cu₉Ga₄, Cu₁₁In₉, Cu₇In₃, and Cu₄In). Then as the second step, after the temperature has exceeded the melting point of Se, the different selenization processes start. In different selenization conditions and deposition methods the formed metal selenides can be very different. Generally speaking, CuSe forms first, which then transforms into CuSe₂ between 190°C and 230°C, which then turns into CuInSe₂ between 250°C and 300°C. The In-Se reactions occur between 225°C and 265 °C, and mean the formation of InSe and In₄Se₃. The formation of α-In₂Se₃ starts above 225°C, while the γ-In₂Se₃ only forms above 450°C. The formation of Cu_xSe and In_xSe₃ is disadvantageous, as they are non-volatile. On the other hand the formation of highly volatile In₂Se also makes it harder to control the processes as it results in a loss of indium [2.3.31, 2.3.34]. The GaSe reactions start at around 315°C. Then the CuInSe₂ (230°C-300°C) and CuGaSe₂ phases appear, which finally react and form Cu(InGa)Se₂. Single phase quaternary CIGS material is only formed at temperatures above 470°C. In phase separated layers the CIS and the CuIn_{0.7}Ga_{0.2}Se₂ phases co-exist. MoSe₂ starts growing after all the other metals have been reacted, as it is formed by the CuInSe₂ donating its two Se atoms to the Mo. It is a way, therefore, to determine when the reaction has terminated. The other conclusion drawn from these experiments is that post-selenized layers require Cu poor layers, as the high copper content decreases the diffusion of the other components.

It has been proposed [2.3.23] that the morphology of the as deposited CIG layer may have a crucial role in the resulting morphology, thus the overall quality of the CIGS film after the selenization. Both evaporated and sputtered CIG layers are inhomogeneous with a rough surface, which is considered to make the preparation of good quality CIGS layer by selenization harder, if not impossible. The reason for the phenomenon has not yet been explained, but it is widely believed that a good alloying with a dominantly Cu₁₁In₉ composition of the metals is required to achieve a stoichiometric material. [2.3.24]

The background pressure during selenization is also crucial. Kim et al. [2.3.25] examined the effect of a 1 atm Ar background pressure during selenization, and found that in this case higher temperatures are required to achieve a single phase chalcopyrite structured material. The reason for this phenomenon is that in a background pressure the Se atoms suffer multiple scattering and loose a considerable fraction of their energy before they reach the surface of the metallic layer. They do not have sufficient energy to migrate on the surface and they can only induce localized reactions. They also found that the surface of the layers selenized in vacuum have a smoother surface morphology.

The selenization method simultaneously applied with a sulphurization has been attempted by a number of groups. The addition of sulphur also helps increasing the band-gap of the absorber, although in a slightly different way than the gallium does: while the Ga content increases the energy level of the conduction band of the CIGS material, the incorporation of S further increases the conduction band and at the same time decreases the valence band [2.3.26].

Advantages and disadvantages of the selenization method

An advantage of the selenization method is that during this process Se diffuses into the Mo back contact of the solar cell, and MoSe_2 is formed on the boundary of the two materials. This results in an improved contact between the active layer and the back contact of the solar cell. An additional formation of Cu_xSe induces crystallization mechanisms that also improve the film quality [2.3.27]. Voljubeva et al. suggested that the formation of the CuSe at the bottom of the film may be a result of Na diffusing through the Mo back contact layer and interfering with the Se flux [2.3.28].

There have been reports on the disadvantages of the selenization method. One is that the selenized layers have a threefold volume expansion compared to the metals. Due to this expansion and the rather different thermal expansion coefficients of the Mo and CIGS films a considerable amount of residual stress is built into the final film. This results in a weaker mechanical adhesion to the substrate and in cases even a peeling off of the absorber film. One approach to overcome this problem by Gupta et al [2.3.29] was to deposit a thin layer of amorphous Se under the metallic components. This layer tends to form very small, sub-micron sized grains, which decreases the mismatch between the two films, and as the nucleation of the metals is different on this Se layer, the morphological and crystalline properties of the CIGS film will also be different - in cases even superior.

The other often mentioned issue is that Ga tends to accumulate near the back contact [2.3.29]. This unintentional grading of the layer is caused by a number of factors. One is the above mentioned residual stress resulted by the volume expansion, which helps the diffusion of the relatively small Ga atoms. The other reason is that in stacked layers copper and gallium may form a Cu_9Ga_4 alloy at the bottom of the film, which reacts very slowly with the Se. On the other hand CuGaSe_2 has a lower reaction rate than that of CuInSe_2 which results in the In being pulled towards the reaction interface, leaving a segregated CuGaSe_2 phase behind. The unintentional grading of the layers can also be seen in the morphology of the layers: The Ga rich layers at the bottom have smaller grain size [2.3.30]. There have been attempts to solve this issue by a post-deposition annealing step, or by a two-step deposition method [2.3.31]. R. Kamada et al [2.3.32] tried to overcome this difficulty by depositing stacks of metal and metal-selenides. They found that if a selenide layer is at the bottom of the stack, then this may serve as a second Se source for the selenization. As the reaction then starts from two interfaces at the same time, a somewhat smoother Se distribution could be achieved, with a slightly elevated Ga concentration in the middle of the film.

A similar approach was adopted by F.B. Dejene et. al. [2.3.31], who used the thermal evaporation of cycles of InSe, GaSe and Cu with a selenization in Se vapour. With inserting several layers of selenides, thus a number of excess Se sources they achieved a uniform depth distribution, and the Ga atoms built into the lattice directly caused an increase in the band gap and an increase of the open-circuit voltages of the devices.

Besides the changes in the Ga concentration an In loss is also often experienced in selenization procedures during the annealing steps due to the low melting point of

the In. This phenomenon is reported by Sugiyama et. al. to be less pronounced if the selenization is performed with diethyl-selenide [2.3.33].

To avoid all the above mentioned problems connected to selenization, Dhere et. al. invented a two-selenization process using Se vapour [2.3.29]. They deposited a stack of Cu rich layers followed by a selenization, then a stack of Cu-poor films followed by another selenization. The procedure is ended with a Cu-Ga over-layer that is meant to avoid globule formation of In. This method improved the adhesion of their layers to the molybdenum under-layer. They controlled the segregation of the Ga and the loss of In by a rapid ramp-up of the temperature and a slow cooling down with Se fluxes maintained.

3. Experimental methods

3.1 The atomic layer deposition system

The reactor used in the experiments was a Picosun SUNALE™ R-100 type ALD reactor. A schematic of the equipment is shown in Fig. 3.1.1. It is a viscous flow reactor equipped with three inlets for precursors and oxidants, and a heatable booster source. All components are made from stainless steel. The sample holder is a 4" size platelet. The reactor is a hot wall reactor, the whole chamber is resistivity heated to the deposition temperature, and the samples are heated by convection and radiation from the reactor chamber walls. The temperature is measured using thermocouples both in the reactor wall and near the heaters, and is regulated by a PID program. The evacuation of the chamber is achieved with a rotary pump to 10 hPa (mbar). The whole equipment is kept in a clean room environment to avoid contamination.

The precursors presently attached to the system are electronic grade purity Diethyl-zinc (DEZ) for the deposition of ZnO, and trimethyl-aluminium (TMA) as a source of aluminium oxide, or Al doping. The source of oxygen is H₂O vapour. The booster source contains Ti isopropoxide, the other precursors are kept at room temperature. The diethyl-zinc and trimethyl-aluminium chemicals are manufactured by Sigma-Aldrich. The carrier gas and purging medium is 99.999% pure nitrogen, in which the precursors are injected by fast valves. Flow rates of the precursor gases and water are 150 sccm. The intermediate space is at all times purged by a nitrogen flow of 300 sccm. During deposition the pressure in the chamber is around 15 mbar. In the case of flat substrate surfaces the pulse time of the precursors is 0.1 s, the purging times are 3 s after each metalorganic precursor pulse, and 4s after the water pulses.

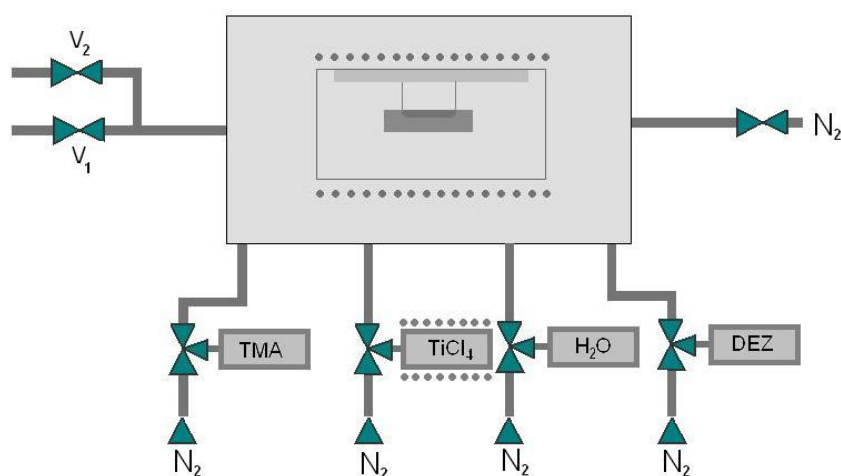


Fig.3.1.1. A schematic of the reactor

3.2 Thermal evaporation and sputtering

Copper, Indium and Gallium films were deposited by thermal evaporation and sputtering for the purpose of the absorber layer.

Two different systems were used to deposit copper, indium and gallium. One of them is a VEB Hochvakuum Dresden BL 25 type instrument operated at $\sim 1 \times 10^{-6}$ mbar background pressure. The evaporation took place from a resistivity heated Ta boat covered with W. The estimated temperature of the source was between 1500-2000°C. The thickness was measured with an oscillating quartz thickness monitor, setting the average density of the components 7.39 g/cm^3 .

The second system used was a vacuum system manufactured by Energosolar, Hungary designed to manufacture Cu(InGa)Se₂ based solar cell modules. The system contains both evaporation and sputtering chambers. However, as the equipment is not finished yet, only Ga and In evaporation sources are installed in the evaporation chamber, therefore the selenization had to be conducted after the deposition of the metallic components.

Mo layers were deposited and target characteristics were monitored by pulsed (10 μs period length with 10% duty factor) DC magnetron sputtering from a 114-440 mm² metallic Mo target. Bi-directional substrate movement under the target took place at 50 mm/s speed at a 60 mm working distance. The vacuum before the opening of the Ar valves was typically 8×10^{-7} mbar. Depositions were typically performed at a 6×10^{-3} mbar working pressure (measured by Edwards WRG – S type Gauge) at 50 sccm total gas inlet. The target power was 750W (in power controlled mode) and the target voltage was 300-315 V. Neither substrate bias nor pre-heating was applied. Cu layers were deposited from a Cu target in the same magnetron sputtering tool the same conditions at a 250 W target power and a 290 V target voltage.

The temperature during In evaporation was 1040°C-1060°C and the pressure 2×10^{-5} mbar, while in case of the Ga evaporation these values were 1115°C-1141°C and 1.7×10^{-5} mbar, respectively.

3.3 Hall measurement

Hall measurement was used to determine the specific resistivity, the carrier concentration and the mobility of the deposited layers. The samples were measured in the Van der Pauw configuration.

In the case of samples fabricated by the ALD method it is important to know, that due to the chemisorption the layer does not only grow on the surface of the substrates, but also on the sides, and even grows under the substrates. Therefore before the fabrication of the contacts the layer on the reverse side of the sample had to be etched off. Then the contacts were fabricated using silver paste and were reinforced with glue.

3.4 Spectroscopic ellipsometry

The ellipsometer used in this work was a Woollam M-2000DI rotating compensator ellipsometer in the wavelength range of 193-1690 nm in 706 points at angles of incidence ranging from 55° to 75°.

The spectra provided by the measurements were fitted with different optical models so that the layer thicknesses, refractive indices and surface roughnesses could be obtained. When the layers comprised different materials, an effective medium approximation was used. This approach supposes heterogeneous mixtures of the components, and derives the complex refractive index from those of the components, under certain restraining assumptions. Most of these methods consider one component as minority and the other as a host, e.g as minor inclusions in a matrix. The Bruggeman effective medium approach used in this work considers a mixture of the two components with arbitrary ratios.

3.5 Microscopy

Different microscopic methods were used for the characterisation of the samples in this work.

The scanning electron microscopy was performed in a LEO 1540 XB system that has a Gemini electron optical column, in which the electron beam is created by a W/ZrO Schottky field-emission cathode. The electrons emitted by the cathode are accelerated to 20 keV. The beam passes through the column with this energy, then is decelerated near the substrate surface to 0.1-20 keV. The system contains an Everhart-Thornley secondary electron detector and an in-lens secondary electron detector at the objective lens of the electron column. The latter makes a magnification of 60-1000 000 x possible (even with 0.5-5keV electrons, in which case the lateral resolution is in the nanometre range) The morphology of the samples was examined with a secondary electron image. These give the images with the best resolution, as –due to their relatively low energy (under 50 eV) they are from the smallest volume near the primary beam.

The elemental composition of the surface of the samples was determined by a Bruker Quantax energy dispersive spectrometer.

The crystalline structure of the surfaces was measured with electron backscatter diffraction. The method gives information of the grain size, shape, orientation and the type of the boundaries. EBSD-measurements were performed by a Philips XL-30 type scanning electron microscope supplied with an EDAX-TSL EBSD-system.

Transmission electron microscopic imaging was performed using a Phillips CM 20 TEM which is an analytical TEM, with a tungsten electron gun that can be operated between 20 and 200 kV. The eucentric sample holder can tilt between -45° and +45° along the A axis and -30° to +30° along the B axis A resolution of 2.4 Å and an electron probe size down to 1 nm (with the objective twin lens pole-piece) is achievable.

High-resolution images were made in a JEOL 4000EX microscope operating with a LaB₆ electron source with an accelerating voltage between 80 and 400 kV. This equipment has an objective lens polepiece designed for HREM utilisation. A point-to-point resolution of 1.65 Å is achievable with it. The images were recorded with a Gatan CCD camera Gatan 622 MKII TV-rate image pick-up system with an image intensifier.

The transparent samples for the TEM investigations were prepared by mechanical cutting and polishing followed by Ar⁺ ion milling at 10 keV ion energy. Cross sectional specimens were inserted into special Ti discs of Ø 3 mm and thinned from both sides. The preparation process was finished at 2.5 -3 keV ion energy in order to remove the small surface layer damaged during high energy ion milling. In some cases additional ion milling were applied at Ar⁺ energies below 1 keV to minimize surface roughness of the specimens for high resolution microscopy.

Atomic force microscopy was used to image the morphology of the samples. The instrument in use for the present work was an AIST-NT, SmartSPM 1010 instrument. The tip was a Budgetsensors Tap300-G type, and was used in tapping mode.

3.6 SNMS and XPS

An INA-X type SNMS equipment by Specs GmbH, Berlin recorded the depth profile analyses in this work. An inductively coupled low-pressure radio frequency Ar plasma was used to provide both sample bombardment and post ionization. The samples were bombarded with Ar⁺ ions extracted from the plasma with the use of high-frequency negative bias on the sample. The bombarding energy could be changed between 100 eV and 2 kV. The remaining gas ions are suppressed by energy dispersive ion optics. The sputtered particles were identified with a quadruple mass spectrometer with a secondary electron multiplier. The concentrations were determined using the relative sensitivity factors of the constituents. The sputtering time was converted to depth scale from sputtering rates determined by a high-sensitivity surface profiler. The largest surface still analysable with this equipment is 14 mm in diameter, the lowest detectable concentrations are in the ppm range, the best achievable depth resolution in the order of magnitude of nanometres.

The XPS measurements were performed with an XPS machine (product of SPECS, Germany) connected to the SNMS measurement chamber, so the specimens could be moved from the SNMS to the XPS measurement chamber in vacuum. Conventional excitation of non-monocromated Al X-rays was used. The XP spectrometer energy scale was calibrated with the relative calibration method measuring Cu, Au and Ag XPS lines and using standard binding energy values determined at the National Physical Laboratory (UK).

3.7 XRD

X-ray diffraction measurements were performed with a multipurpose Bruker AXS D8 Discover horizontal X-ray diffractometer equipped with Göbel mirror and a two dimensional GADDS detector system. The samples are mounted on a motorized X, Y, Z stage; their precise alignment is made possible with a positioning system with laser and camera. Two different detectors may be used with this instrument: a scintillation point detector and a 2D position sensitive (GADDS) detector. The X-ray source is a Copper anode X-ray tube, Cu K α radiation is used in most experiments, with a monochromatic and parallel beam of 500 μ m in diameter.

For the evaluation of the XRD peaks the following data International Centre for Diffraction Data Powder Diffraction Files (ICDD PDF) were used:

CuGa_{0.3}In_{0.7}Se₂: 00-35-1102

CuInSe₂: 00-40-1487

CuSe₂: 00-26-1115

Cu₂Se: 01-079-1841

ZnO: 00-036-1451

For reciprocal space mapping measurements, a 1 dimensional position sensitive detector (Bruker Vantec-1) and monocromated Cu K α radiation with a Ge 002 monochromator crystal were employed.

3.8 UV-VIS transmittance spectroscopy

The transmission UV-VIS spectra were determined at room temperature using 265 mm focal length ORIEL grating monochromator equipped with lock-in amplifier, Si avalanche photodiode detector and a 75 W xenon lamp. The scanned spectral resolution was 1 nm.

II. Results and discussion

4. Atomic layer deposition of Al doped ZnO layers

The literature of the atomic layer deposition of Al doped ZnO films lacks a systematic examination of the structure and conductivity of these layers with different doping and deposition temperatures. This was the aim of this work.

Doped and undoped ZnO layers were deposited in the ALD reactor described in chapter 3.1. Diethyl-zinc (DEZ) precursor was used for the deposition of ZnO, and trimethyl-aluminium (TMA) as a source of the Al dopant. The source of oxygen was H₂O vapour in both cases. All precursors were electronic grade purity and kept at room temperature. The carrier gas and purging medium was 99.999% purity nitrogen. During deposition the pressure in the chamber was 15 mbar. The pulse time of all precursors was 0.1 s, the purging times were 3 s after each metalorganic precursor pulse, and 4 s after the water pulses.

The layers were deposited on (100) Si wafers with 10-15 Ωcm resistivity and 3 mm thick soda lime glass cleaned in cc.HNO₃ and high purity 5 MΩ resistivity water. In all the deposition processes Si and glass substrates were placed into the reactor at the same time, so that the same layers were deposited on them. The glass samples were later used for the resistivity measurements, and the Si samples for the microscopic, ellipsometric and XRD measurements.

Growth conditions	ALD parameters
Precursors	Diethyl zinc and Trimethyl aluminium
Oxidant	H ₂ O
Process pressure	10-15 mbar
Substrates	Si/ Glass
Deposition temperature	120°C, 150°C, 180°C, 210°C, 240°C, 270°C, 300°C
Cycle sequence	(i(DEZn+H ₂ O)+TMA+H ₂ O) _j +i(DEZn+H ₂ O), with(i between 9 and 60)
Reservoir temperature	24°C
Injection time	0.1 s
Purge time	3 s
Flow rates	Precursors:150sccm, H ₂ O: 300 sccm

Table 4.1. Growth parameters of the layers

The layers were deposited at seven different substrate temperatures: 120°C, 150°C, 180°C, 210°C, 240°C, 270°C and 300°C on both types of substrates. One deposition cycle consisted of a DEZ or TMA pulse, then a purge, followed by a water pulse, then a purge again. Both the first and the last deposition cycle was always ZnO. Using sequences of these cycles, the following Al-ZnO layers with different doping levels were prepared (Table 4.2):

Deposition cycles	Al atom%	T
500 layers ZnO	0	all
240 layers of ZnO+1 layer Al ₂ O ₃ + 240 layer ZnO	0.1	150°C
7 cycles of (60 layers ZnO+1 layer Al ₂ O ₃) +60 layers ZnO	0.7	150°C
9 cycles of (50 layers ZnO+1 layer Al ₂ O ₃) + 25 layers ZnO	0.9	150°C
11 cycles of (40 layers ZnO+1 layer Al ₂ O ₃) + 40 layers ZnO	1.1	150°C
15 cycles of (30 layers ZnO+1 layer Al ₂ O ₃) + 30 layers ZnO	1.5	all
18 cycles of (25 layers ZnO+1 layer Al ₂ O ₃) +25 layers ZnO	1.9	150°C
21 cycles of (21 layers ZnO+1 layer Al ₂ O ₃) + 21 layers ZnO	2.1	all
23 cycles of (19 layers ZnO+1 layer Al ₂ O ₃) + 19 layers ZnO	2.4	150°C
26 cycles of (17 layers ZnO+1 layer Al ₂ O ₃) + 17 layers ZnO	2.6	150°C
30 cycles of (15 layers ZnO+1 layer Al ₂ O ₃) + 15 layers ZnO	3	all
40 cycles of (11 layers ZnO+1 layer Al ₂ O ₃) + 9 layers ZnO	4.1	all
48 cycles of (9 layers ZnO+1 layer Al ₂ O ₃) + 9 layers ZnO	4.9	all

Table 4.2. Deposition recipes for doped Al-ZnO layers with calculated concentration values

The 150°C series was the most detailed: it consisted of samples with 13 different doping levels, while at the other temperatures 6 doping levels were tried.

Although all deposition processes consisted of approximately 500 cycles, depending on the deposition temperature and the doping, the thickness of the resulting layers varied between 40 and 90 nm. In some cases the thicknesses were also determined with stylus step height measurement, but as the two measurements gave the same results within a few nm deviation, the ellipsometry results were considered sufficient in the following experiments.

After the deposition, electrical contacts were fabricated on the samples with glass substrates using silver paste. The sheet resistivities and carrier concentrations were then measured in the Van der Pauw configuration. The specific resistivities and the mobility values were calculated considering the thickness values received from the ellipsometry results.

4.1 The structure and morphology of Al doped ZnO layers

Fig. 4.1.1. shows the growth rates at different temperatures and different doping levels.

The growth rate-T curves have a maximum at around 150°C, which corresponds to the location of the ZnO ALD window described in the literature [2.3.29]. The Al doped samples on the other hand have a somewhat wider window, with the growth rates still high at 180°C.

The growth rate also correlates with the amount of the introduced Al, i.e. it decreases with the increasing Al content. These general characteristics are similar at each growth temperature. The growth is slowing down with the increasing number of the Al pulses, since the Al₂O₃ has to nucleate on ZnO surface and vice versa [2.3.37].

The roughness of the layers on silicon was determined by AFM and found to be around 5 nm. The surface roughness of the silicon substrates is well under 0.5 nm.

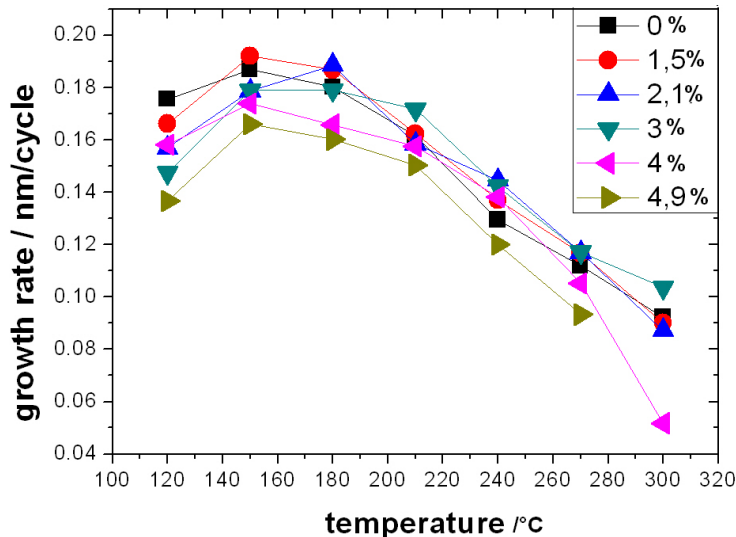


Fig. 4.1.1. Temperature dependence of the growth rate of the Al-ZnO layers with different Al contents

The XRD measurements of the samples showed that the crystallinity of the layers depends both on the deposition temperature and the Al doping. The analysis shows that both the intrinsic and the aluminium doped layers contain polycrystalline ZnO with wurtzite type structure (ICDD JCPDS 36-1451), and no crystalline Al₂O₃ phase was recognizable. The intensities were always normalized with the thickness of the layers. The intensity ratios of the ZnO peaks differ from the ones characteristic for random oriented powder samples, showing a textured character of the layers.

As examples, Fig. 4.1.2. shows XRD $\Theta/2\Theta$ spectra of three intrinsic ZnO samples deposited at three different substrate temperatures with the positions and Miller indices of ZnO peaks indicated. Typically the (101) peak, which is theoretically the

strongest in powdered ZnO samples, is present in most samples, but its relative intensity is low. The samples deposited at higher temperatures have a more pronounced crystallinity. In the case of the 120°C sample, the (100) peak is the most prominent; while the change of the peak intensity ratios with increasing deposition temperature, i.e. the growth of (002) peak after 210°C and the vanishing of (100) peak at 210°C shows the change of preferred orientation depending on the deposition temperature. The change of the orientation means that while at lower temperatures the c axis of the ZnO unit cell is parallel to the substrate surface; in the layers deposited at higher temperatures the c axis is perpendicular to it. This phenomenon is in agreement with the results of Ref. [2.3.30, 2.3.32]. The spectrum of an Al doped sample is also shown in the picture. It is evident that the Al doping decreases the orientation of the layers.

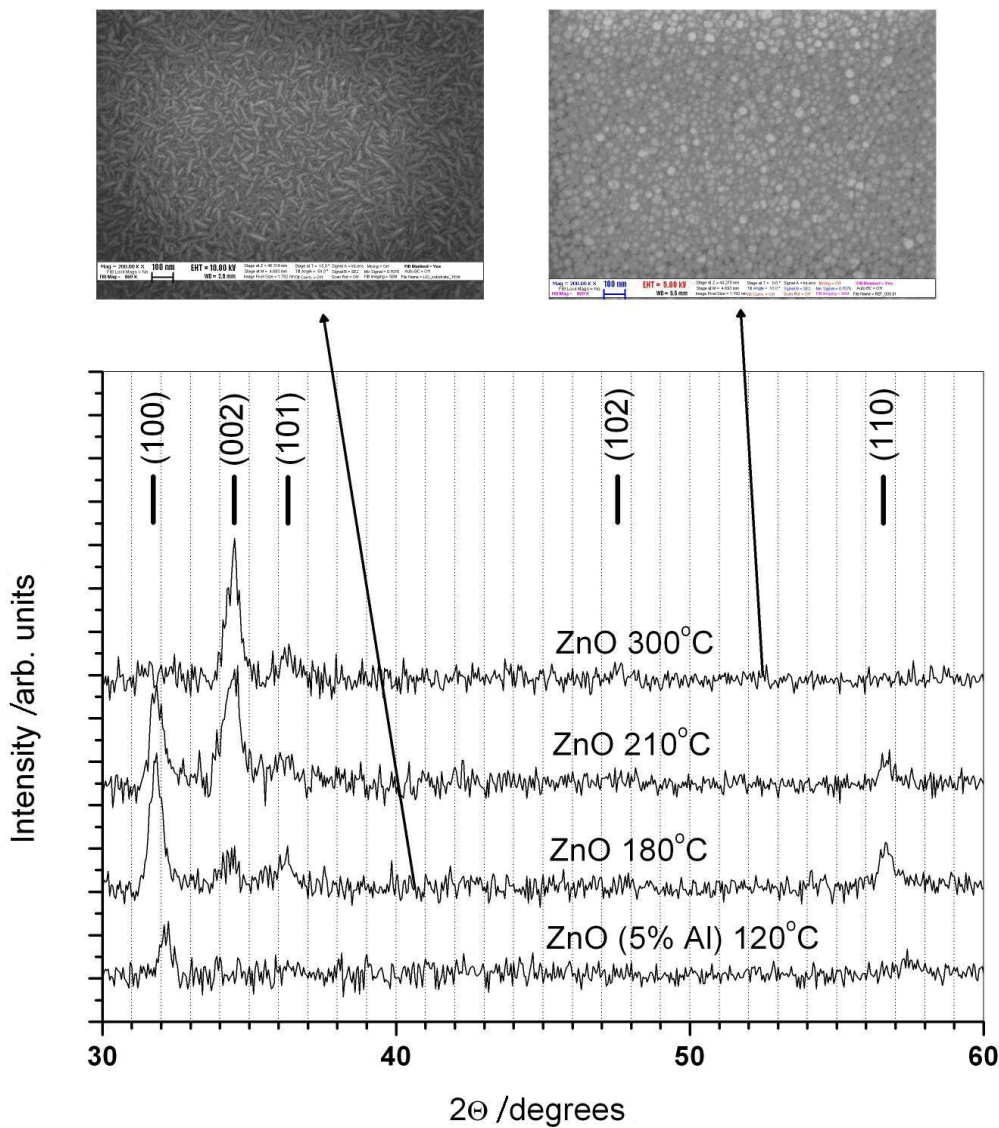


Fig. 4.1.2. XRD spectra of ALD ZnO layers deposited at different temperatures
The Al doping decreases the lattice constant at all temperatures (compressive

strain), at higher temperatures this effect is more pronounced. The aluminium incorporation decreases the grain size and changes the preferred orientation. In the doped samples deposited at lower temperatures a (100) orientation is dominant, but not as much as in the non-doped case. With the increasing deposition temperature, in the intrinsic samples the (002) orientation appears while in the doped ones the (101) orientation becomes apparent. Finally, at the highest deposition temperature, the (002) orientation becomes dominant in the intrinsic c samples, while there is no preferred orientation in the aluminium doped ones, and the grain size becomes very small (which was also confirmed by the TEM analysis). The samples with the highest aluminium content of 5 at% and the intrinsic ones were characterized at every deposition temperature and these results are summarised in table 4.1.1.

	intrinsic	4.9 at%
120°C	Small grain size; typical orientation: (100)	No pronounced orientation, (100) apparent
150°C	(100) dominant	No pronounced orientation, (100) apparent
180°C	(100) orientation even more dominant	Beside the (100) orientation (101) appears
210°C	Besides (100) (002) becomes more apparent	(100) and (101)
240°C	Better crystalline structure. (100) and (002)	No orientation, very small grains.
270°C	(002) more dominant than (100) and (101), but all of them are present.	No orientation, very small grains.
300°C	(002) orientation	No orientation, very small grains.

Table 4.1.1. Summary of the XRD findings

Fig. 4.1.3. shows the intensities of the characteristic (100) and (002) peaks vs. the deposition temperature in the case of the Al doped samples. These figures clearly reflect that the typical orientation of doped ZnO layers depends on the deposition temperature and develops a tendency similar to the one found on intrinsic samples. In the case of the 120°C and 150°C samples the (100) orientation was present, i.e. the c-axis of the crystallites was parallel to the surface. As the deposition temperature increases, the (002) peak becomes more and more pronounced while the (100) gradually disappears. In the case of the 270°C and 300°C samples the (002) is the dominant orientation, i.e. the c-axis of the crystallites is standing perpendicular to the surface.

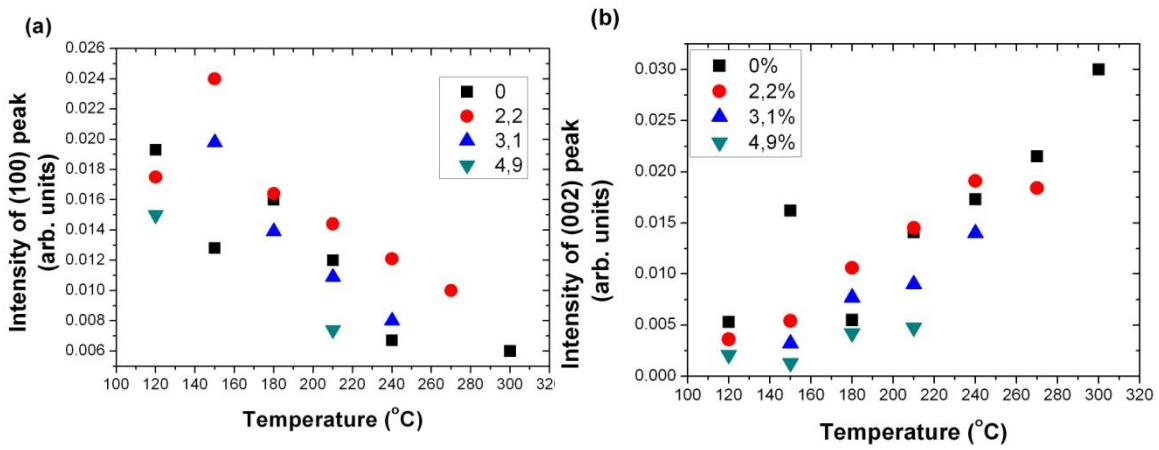


Fig 4.1.3. a and b respectively: intensities of (100) and (002) peaks as a function of the deposition temperature

Fig. 4.1.4. displays the intensities of the (100) and the (002) peaks as a function of the aluminium content. The aluminium doping improves the crystallinity of the layers up to a certain point (approx. 2 at%). This is the same region where (as shown in the next chapter) the resistivity also has its minimum. Excessive aluminium incorporation on the other hand destroys the crystallinity of the ZnO, which leads to an increased resistivity.

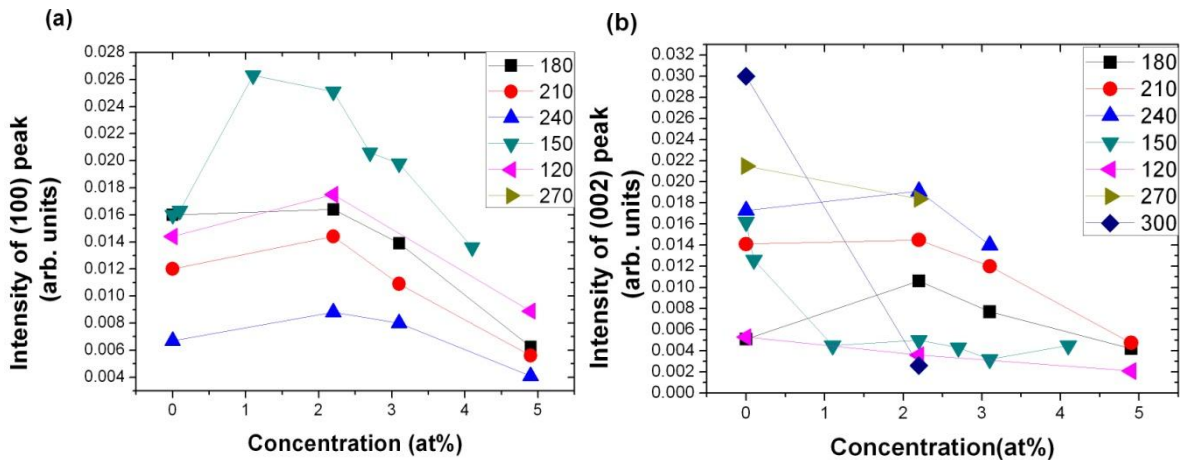


Fig. 4.1.4. a and b respectively: intensities of (100) and (002) peaks as a function of the Al content

The crystallite size of the layers is inversely proportional to the FWHM of the diffraction peaks. The exact value of the grain size cannot be evaluated from this measurement, as the very small layer thickness also causes a widening of the diffraction peaks. The size of the crystallites has a maximum at around 2% Al content (Fig. 4.1.9.) At 5 at% the crystallite size is very small, and the overall crystallinity of the samples deteriorates as well.

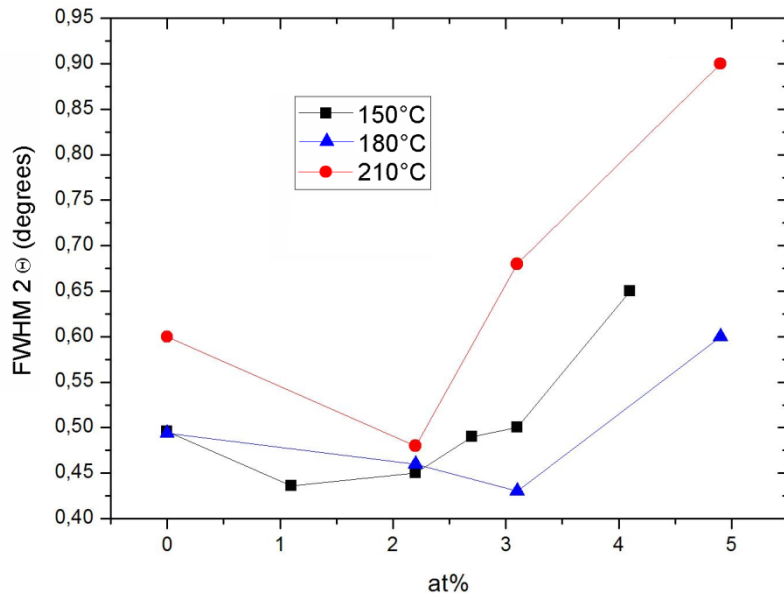


Fig. 4.1.5. FWHM of the (100) peak vs. Al content

Fig. 4.1.6. depicts the 2θ position of the (100) and (002) peaks vs. Al amount. A shift towards larger 2θ values can be observed, which indicates an accumulation of compressive strain in both crystallographic directions with the aluminium doping. Although the signal to noise ratio of the XRD data was relatively low, the tendency of the results can clearly be seen

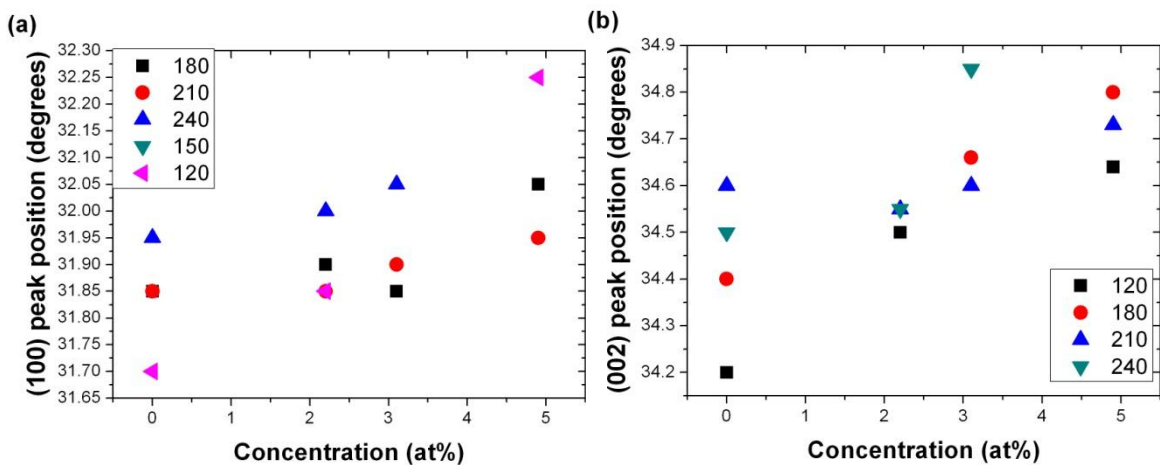


Fig. 4.1.6. 2θ shift of the characteristic peaks as a function of the aluminium doping

The above measurements were performed on ALD ZnO layers deposited on Si, but it is important to emphasize that the same analysis carried out on samples grown on glass substrates resulted in the same behaviour. Therefore, it can be concluded that the obtained results are independent of the substrate in the case of polycrystalline

layers.

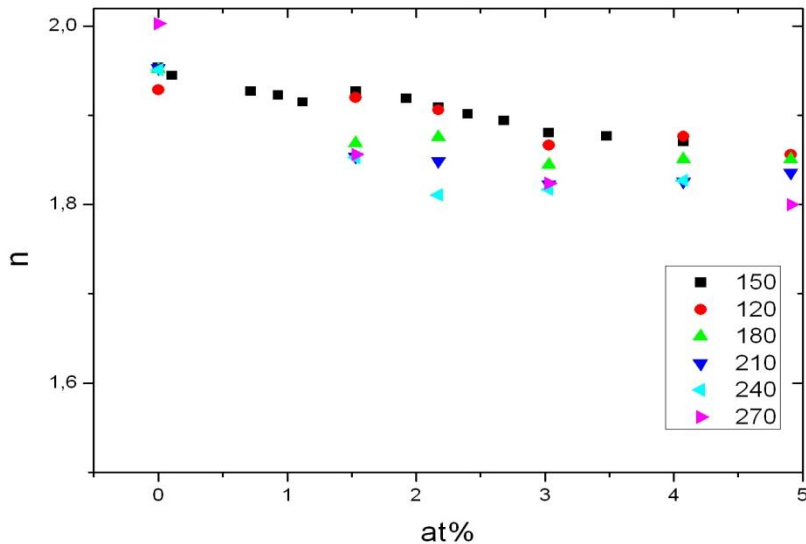


Fig.4.1.7. The real part of the complex refractive index as a function of the Al doping

Fig. 4.1.7. shows the real part of the refractive index plotted against the Al atomic percent. All of the measured results from the samples deposited at different temperatures follow a linear tendency within a narrow range. The refractive index decreases with the aluminium incorporation, but does not depend on the deposition temperature. The refractive index of the intrinsic ZnO is around 1.95, in agreement with the literature data, while that of Al_2O_3 is 1.7. Therefore, we may say that with the incorporation of the aluminium the refractive index of the layer is shifted towards that of Al_2O_3 . In this respect the layers behave like an alloy of ZnO and Al_2O_3 . As the XRD results reflect no phase separation, there are no crystalline Al_2O_3 grains present in the sample.

XPS measurements were also conducted by sputtering the layer off to the Al containing sublayer, and the Al layer is definitely not continuous. The actual Al content is only 0.2% in the Al containing region, whereas a complete mono-layer coverage would require at least 1% of Al concentration. This is in agreement with ref. [2.3.32] and [2.3.30]. The Al_2O_3 ALD process is always somewhat slow: the mono-layer/cycle growth rate cannot be achieved, in fact a growth rate of 0.1 nm / cycle which corresponds to a growth of about 0.25 mono-layers / cycle is generally considered the achievable maximum. On the other hand Al_2O_3 growth on ZnO also has nucleation issues with an initial ZnO growth of only 27% and Al_2O_3 growth 67% of the steady growth rates. This would mean a 0.17 mono-layer, and is in a fairly good agreement with the result of the experiment.

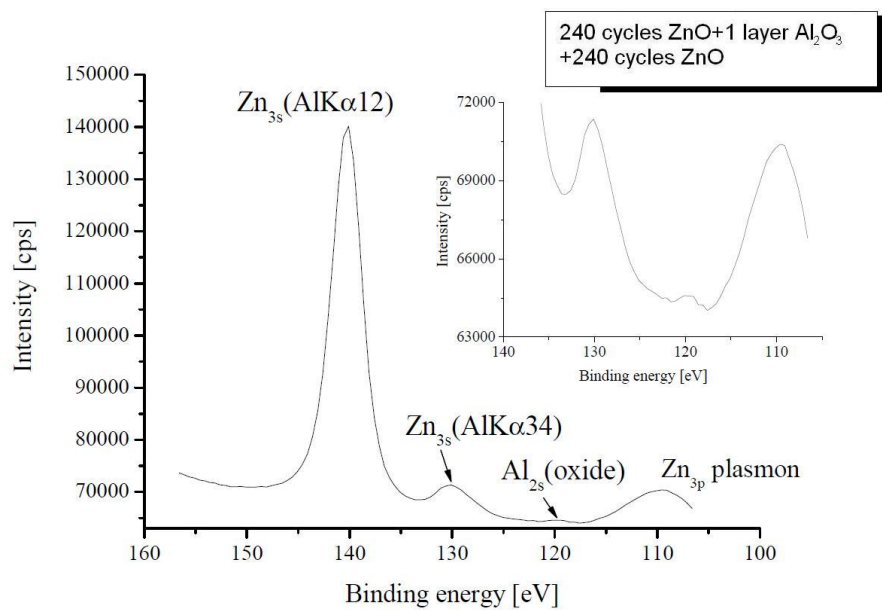


Fig 4.1.8. XPS spectra of the sample of Fig. 4.1.2 and 4.1.3 taken at the Al sublayer

In Fig. 4.1.8. the XPS spectra of the same layer taken at the Al sublayer show that the Al is present in the layer mostly in the form of Al_2O_3 . Auger analysis of the data established that about 10-20% of the whole Al quantity introduced is not in Al_2O_3 bond. This is the fraction of the Al content that is incorporated into the ZnO lattice in the Zn sites, and this fraction can increase the n-type conductivity of the layer by donating electrons to the material. The rest of the Al doping is present in the form of Al_2O_3 and the two oxides are alloyed with each other.

4.1.2 The resistivity of the ALD deposited AZO layers

Fig. 4.2.1. summarizes the specific resistivity of the layers as a function of the Al content and substrate temperature. The measurements were done on layers deposited on glass.

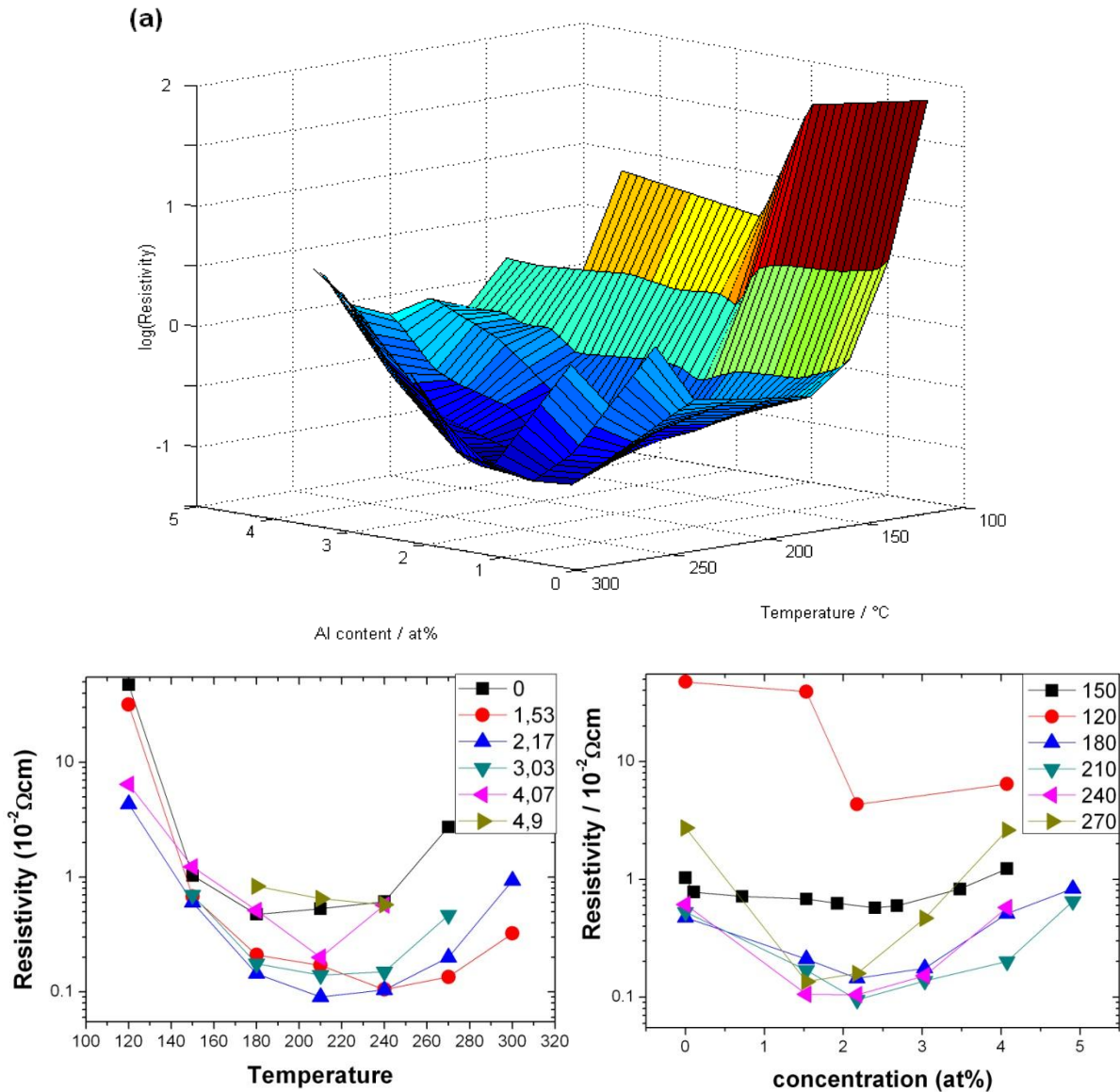


Fig.4.2.1. Specific resistivity as a function of the doping level and the substrate temperature. a: 3D view, b: temperature dependence, c: dependence on doping

The two dimensional surface in Fig. 4.2.1.a shows the specific resistivity vs. the doping level and the temperature, while Fig 4.2.1. b and c are projections of this surface.

The conductivity of the intrinsic ALD ZnO decreases between 120°C and 210°C in agreement with the literature data [2.3.4]. The minimum of the intrinsic resistivity, as can be seen in Fig. 4.2.1.b, is at 180°C and its value is $4.7 \times 10^{-3} \Omega\text{cm}$. The minimum resistivity achieved with doping was $9 \times 10^{-4} \Omega\text{cm}$. Above 210°C the resistivity starts to increase again. As it can be seen in Fig. 4.2.1.b, at a given level of doping the temperature dependence of the resistivity follows a convex curve. All of these curves have their minimum around 210°C. The doping effect increases with the temperature (as proposed in [2.2.20 and 2.2.39]) up to this region, beyond this, the resistivity increases again. It can also be seen from Fig 4.2.1., that the doping efficiency (i.e. the ratio of electrically active Al vs. Al_2O_3) is also affected by the temperature. The doping has a maximum efficiency at around 210°C. Plotting the resistivity against the aluminium concentration at a given temperature results in a similar picture. Compared to the intrinsic values, the resistivity first drops then reaches its minimum at 1.5-2.5 at%, then at higher Al levels it increases rapidly again.

To investigate the physical background of these changes in the resistivity we also performed Hall measurements. In Fig. 4.2.2.a we can see the mobility and the carrier concentration as a function of the deposition temperature in the case of the intrinsic samples. The carrier concentration grows with the increasing deposition temperatures, then passing a maximum, in the same region where the resistivity has its minimum, then it falls again. At the same time mobility decreases throughout the whole temperature range. In the intrinsic case the carrier concentration originates merely in the intrinsic dopants, that is oxygen vacancies, Zn interstitials and built in hydrogen, the number of which depends on the deposition temperature.

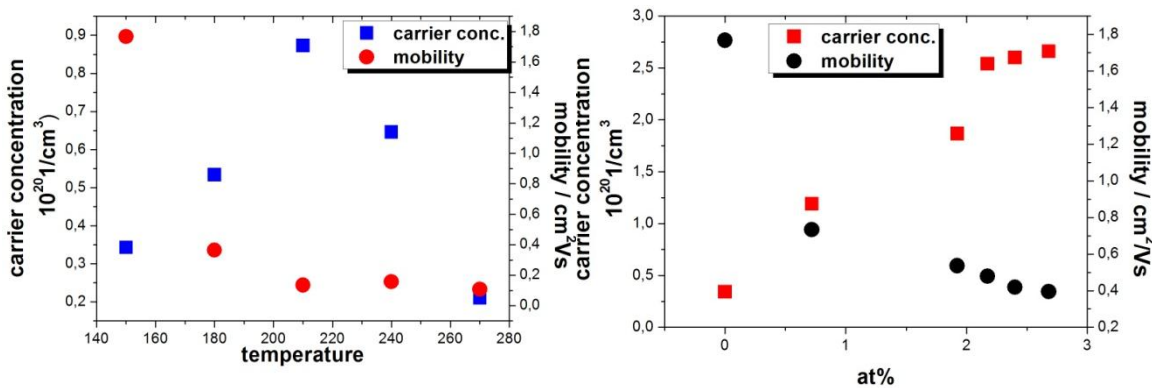


Fig. 4.2.2. The dependence of the carrier concentration and the mobility on the temperature (a) in the case of the intrinsic samples, and on the doping (b) shown on the 150°C series

In Fig. 4.2.2.b the typical dependence of the mobility and the carrier concentration on the aluminium content is shown for the 150°C series. The carrier concentration

increases monotonically and the mobility decreases as a function of the aluminium content. Although the aluminium incorporation occurs in a form of Al_2O_3 doping, a fraction of the Al proportional to the $\text{Al}_2\text{O}_3/\text{ZnO}$ ratio is still incorporated as electrically active dopant.

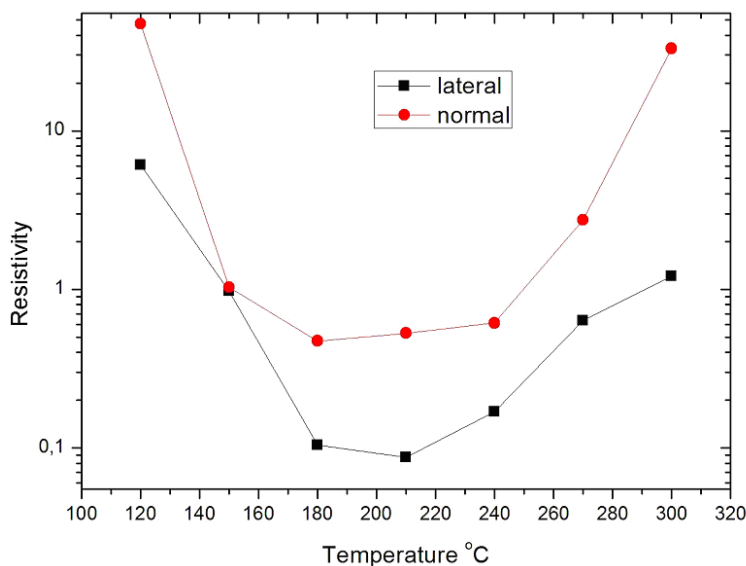


Fig. 4.2.3. Specific resistance parallel and perpendicular to the layer surface vs. deposition temperature on ZnO on Si samples

Fig. 4.2.3. presents the resistivity of the samples both in parallel and normal directions to the surface. In latter case the Si , on which the ZnO layer was grown, served as a back contact, while the top electrode was evaporated Ag . In this case the quantitative values of the resistivities were substantially higher than the lateral ones, as a result of the addition of the series resistance of the silicon wafer and a depleted layer between the films. Therefore, the measured values have been rescaled and displayed together in a graph with the lateral measurements (arbitrary units on the y axis). The curves in Fig. 4.2.3. display the qualitative behaviour of the resistivity vs. temperature curves, and it is evident, that the two curves exhibit similar qualitative tendencies (i.e. they are both convex, with a minimum at 210°C). The conductivity shows no anisotropy as a function of the deposition temperature, whereas the XRD curves revealed a monotonous change of dominant crystallite orientation from parallel to perpendicular. Therefore grain boundary conduction cannot dominate the electrical conduction behaviour.

Fig. 4.2.4. shows the temperature dependence of the ellipsometric band-gap on the deposition temperature (Fig. 4.2.4.b), and on the aluminium doping (Fig 4.2.4.c). As it can be seen from Fig. 4.2.4.b, the doped samples develop a band-gap minimum at around 180°C substrate temperature while the doping level dependence shows an increasing tendency towards higher Al atomic fractions.

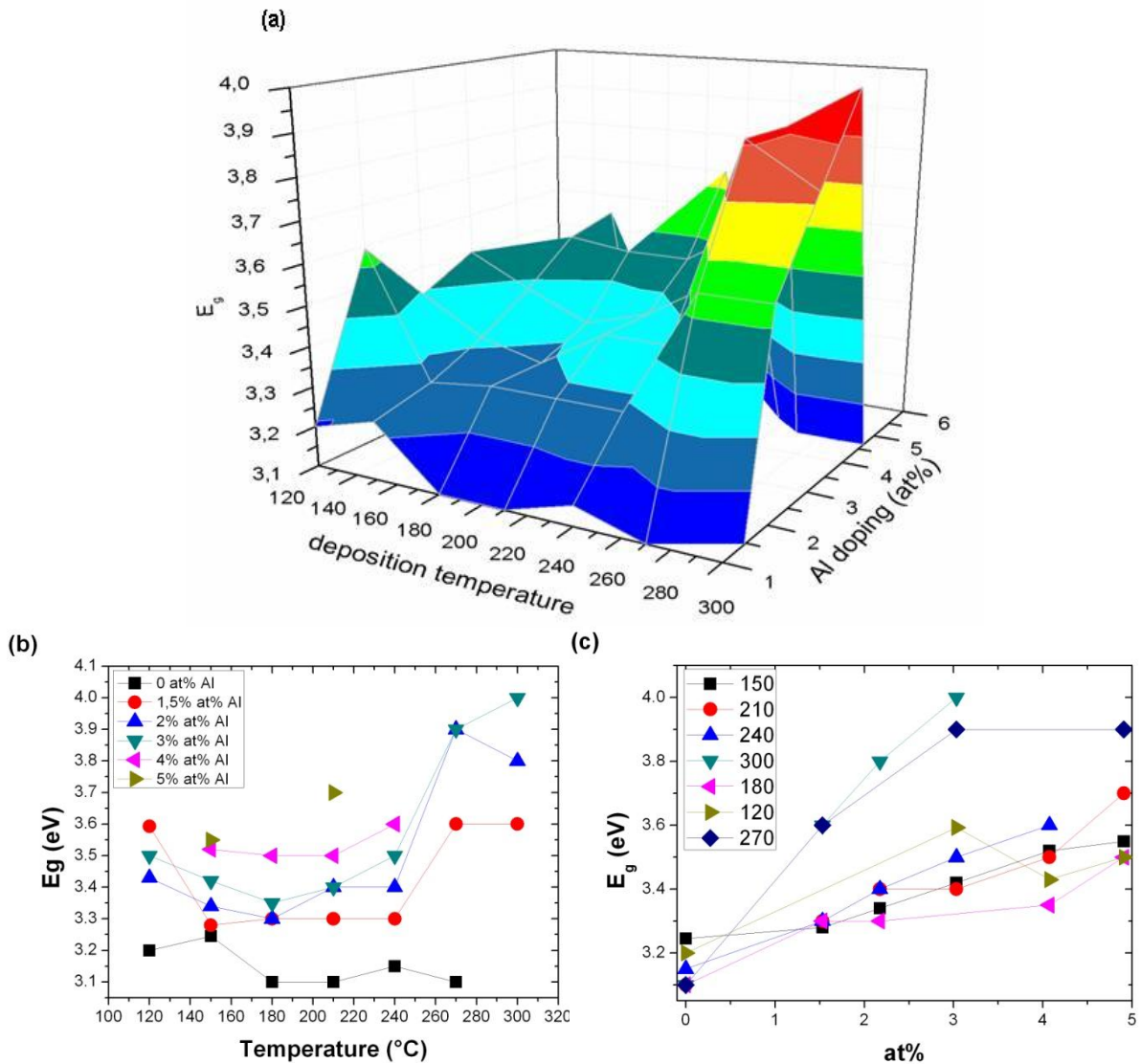


Fig. 4.2.4. The band gap of the Al doped ZnO layers as a function of the substrate temperature (b) and Al atomic fraction (c) deduced from ellipsometric measurements.

The band-gap can be tailored by alloying the two oxides. The band-gap of Al_2O_3 is wider than that of ZnO , therefore the increasing band-gap shows the aluminium oxide built into the ZnO layer. This correlates with the resistivity and the carrier concentration data. Outside the optimal doping range the majority of the added Al pulses is incorporated in the film as Al_2O_3 . In the optimal range of the parameters on the other hand a greater ratio of the added aluminium is built in as substitutional dopants into the ZnO lattice.

Fig. 4.2.5 shows UV-VIS transmission spectra of the intrinsic, the 2 at% and the 4.9% doped samples deposited at 120°C, 210°C, and 300°C.

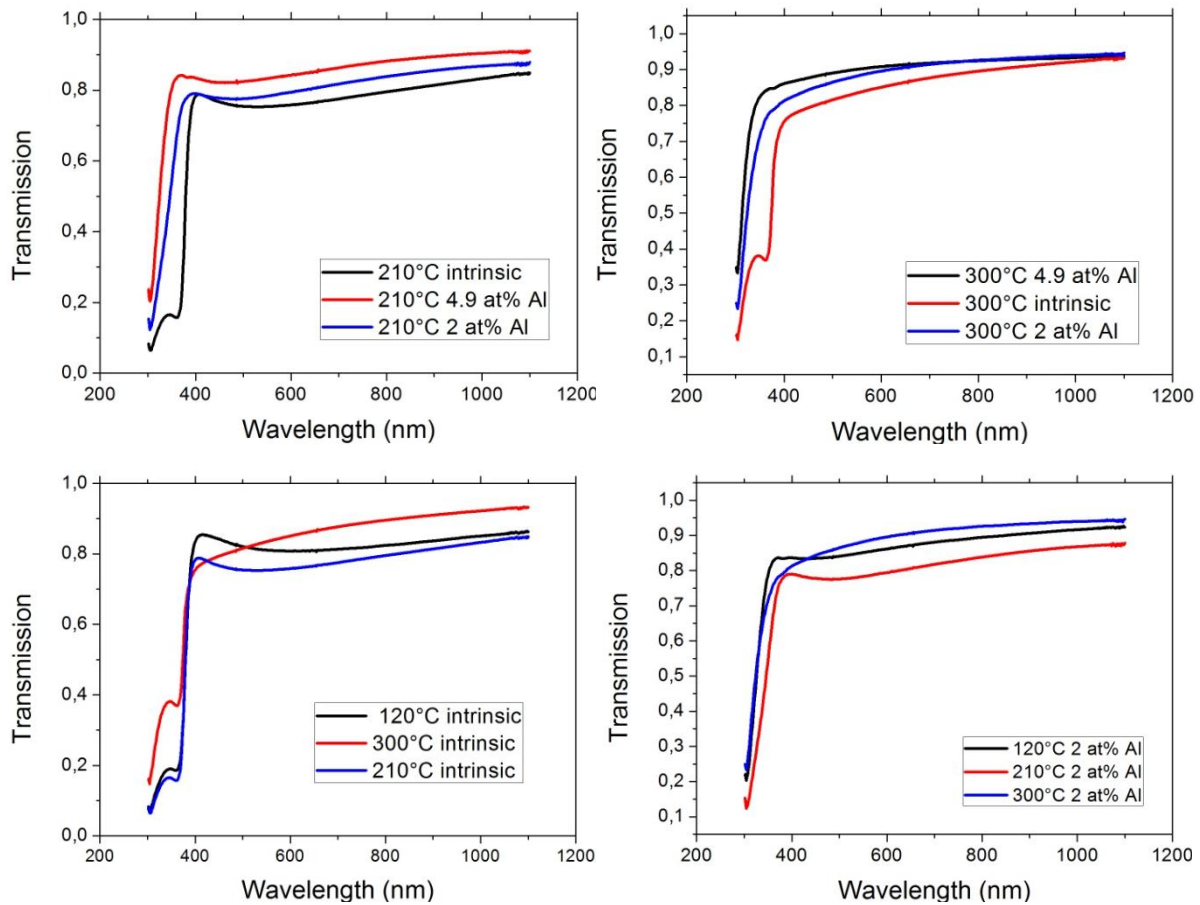


Fig. 4.2.5 Transmission spectra of the intrinsic and 5% doped samples deposited at 120°C, 210°C and 300°C

In the case of window electrodes the composition is usually defined by a compromise between the conductivity and the transparency. In the case of these samples it can be seen, that the Al doping actually improves the transparency of the layers, and widens the transmission window. The deposition temperature increases the transmission in the 400-600 nm range.

The transmission spectra were converted to absorption coefficient α using the Beer-Lambert equation. Plot of α^2 vs. $h\nu$ gives a straight line in a given $h\nu$ range, which extrapolates at $\alpha^2=0$ to the bandgap value E_g . Fig. 4.2.6 shows the α^2 vs. $h\nu$ curves of the intrinsic and 2% doped samples deposited at 210°C, as it can be seen, the doped samples develop a characteristic blue shift of approx. 0.3 eV compared to the intrinsic ones. This is again in correlation with the ellipsometric band-gap data.

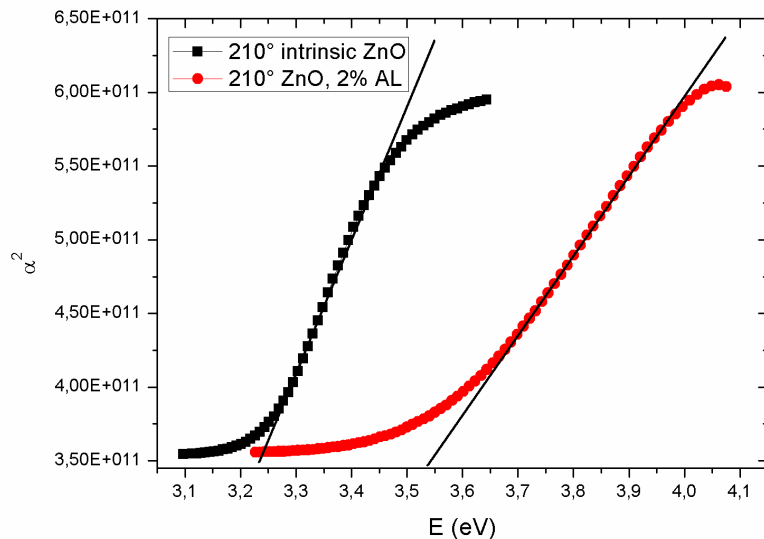


Fig. 4.2.6 The α^2 vs. $h\nu$ curves of the intrinsic and 5% doped samples deposited at 210°C

The atomic layer deposition of the ZnO layers has also been attempted on CIGS layers. A 40 nm thick 2 at% doped layer was deposited at 150°C on a commercially available CIGS film. The layer covered the absorber film uniformly and conformally, as it can be seen in Fig.4.2.7. The consecutive ZnO sputtering then covered the layers evenly and pinhole-free, which would have been impossible without the ALD grown buffer layer.

As shown above in this chapter, the conductivity and the band-gap of the ALD deposited ZnO films can be varied in a wide range, therefore a band-gap engineering of the solar cell materials is possible with the ALD ZnO buffer layer.

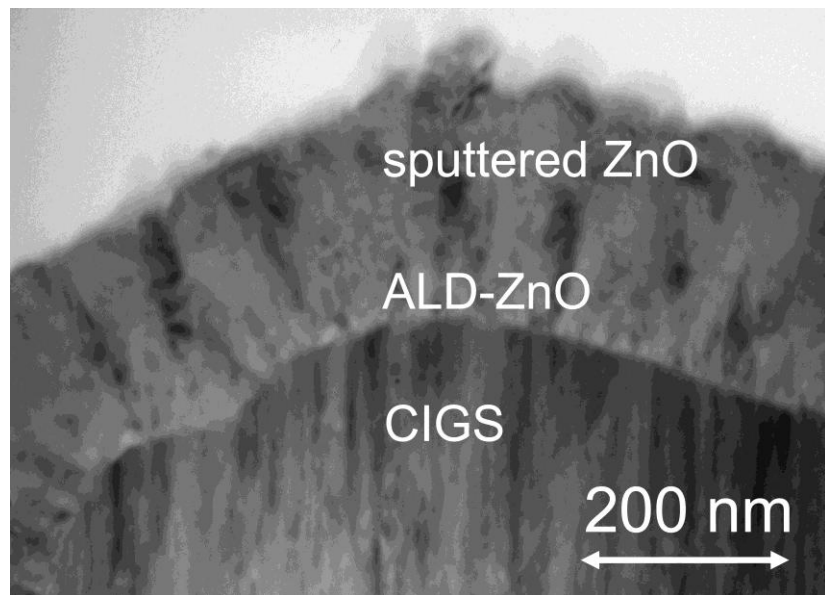


Fig 4. 2.7. Periodic alternate injection of Zn and Al precursor pulses by ALD results in a ZnO layer with good conformal coverage on polycrystalline CIGS offering the possibility of the deposition of vacuum compatible buffer layers with various qualities.

5. Nucleation and growth of atomic layer deposited ZnO layers

5.1. The nucleation of ALD deposited ZnO

To study the initial phases of film growth on different substrates, ZnO layers have been deposited on GaN, graphene, sapphire and p-type (100) Si wafers with 10-15 Ωcm resistivity. The substrates were cleaned by acetone, ethylene and high purity (5M Ω) water, except for the Si substrates which were cleaned with cc.HNO₃ and high purity water. ZnO layers with 5, 10, 15 and 30 ALD cycles were grown on all substrates at 150, 220 and 300°C deposition temperatures.

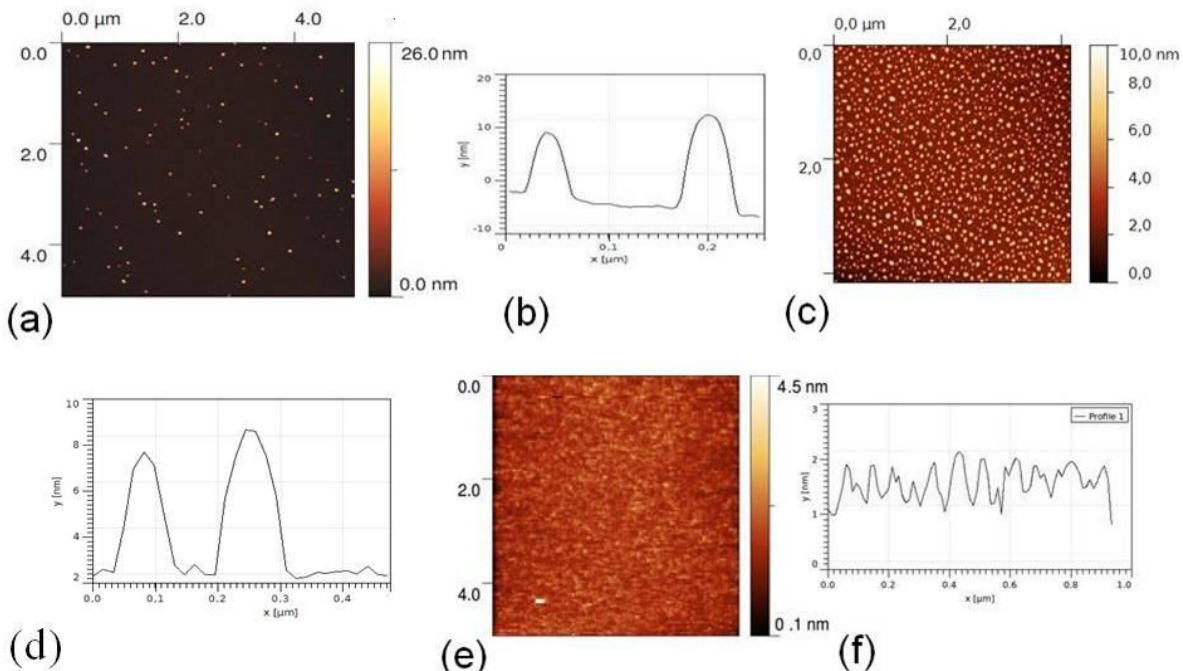


Fig. 5.1. AFM micrographs of the growth of ZnO on Si at 150°C. a: after 5 cycles, b: the profile of this surface, c: after 10 cycles, d: the profile of this surface, e: The layer after 30 cycles, f: the profile of this surface. All the pulses are 0.1 s long.

Fig. 5.1. shows the morphologies of the ZnO layers on Si surfaces grown at 150°C. It is evident from all the images that the ZnO exhibits an island-like growth on Si. The sample with 5 cycles of ALD deposited ZnO can be seen in Fig. 5.1.a. There are ZnO islands scattered over the surface. Their height is around 10 nm, and they are around 60 nm in diameter. With a quick estimation we can calculate the amount of ZnO this means on the surface. Taking a 10 $\mu\text{m} \times 10 \mu\text{m}$ area on the surface, this means about 100 sphere sections. Adding up their volumes we get a volume in the range of 10^6 nm^3 ZnO. On the other hand if we assume layer by layer growth with a growth rate of 0.19 nm/cycle (which is the typical growth rate at this temperature), a ZnO layer with a thickness of 0.95 nm would cover the surface. This would mean a volume in the order of magnitude of 10^8 nm^3 ZnO.

This quick estimation is in agreement with the spectroscopic ellipsometry results. For the evaluation of the measurements a Bruggeman effective medium approximation was used, supposing a 10 nm thick film which is a mixture of ZnO and air. The model fitting gave the result that 1.57% of the film volume is ZnO in the case of the samples with 5 cycles of ZnO deposited at 150°C. In the case of the sample with 30 cycles of ZnO at the same deposition temperature, the fitting gave a 6.7 nm layer with 90% ZnO with a surface roughness, which is in agreement with the continuous layer also shown in Fig. 5.1. At 300°C deposition temperature, according to the ellipsometric results 1.06% of the 10nm thick film is ZnO, which is also in agreement with the AFM results.

This leads to the conclusion that the process behind this island-like growth is not the particles adsorbing on the surface followed by island formation due to surface diffusion. Instead, as there is much less material on the surface, it seems that the nucleation itself also occurs slower than expected, and a nucleation issue must be in the background of the phenomenon, probably due the lack of bonding sites on the surface, as the SiO_x surface does not have as many OH groups as presumed. Haukka and Roots in Ref. [5.1] found that depending on the temperature, between 200°C and 400°C there are about 1-2 OH groups on every nm² of the SiO_x surface.

After 10 cycles there is a lot more islands on the surface, but their size is approximately the same as in the 5 cycle case. After 15 cycles the islands have started to grow together, and a full coverage is achieved. After 30 cycles a full and uniform coverage of the surface can be seen. The roughness of the layer is around 1 nm. The other deposition temperatures resulted in very similar morphologies. At 220°C the nucleation is even slower: The coverage is still not complete after 30 cycles. At 300°C the layer only becomes uniform after 60 deposition cycles.

The above mentioned results were also verified with scanning electron microscopy.

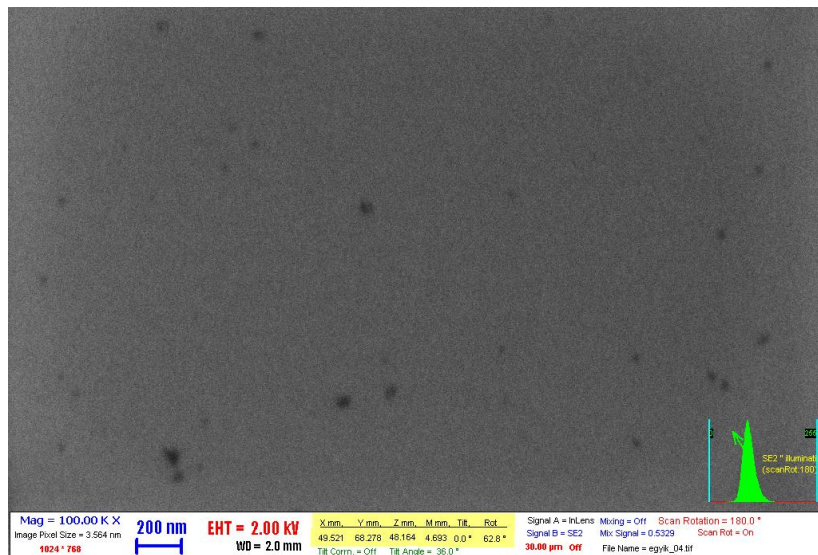


Fig. 5.2. SEM micrograph of the sample with 5 cycles of ZnO

The islands could be seen on the secondary electron micrographs as well, and the EDS elemental analysis confirmed a higher ZnO concentration in the islands than on the surface between them.

From the changing of the surface morphology with the increasing number of deposition cycles it can be seen, that after the first cycle not all bonding sites have been occupied as the precursors in the later cycles fill in further nucleation sites at the surface. This can be seen from how further islands with the same size are formed instead of the growth of the already existing ones in height and diameter. To verify this model the following deposition methods were tested: a 1 s long first pulse, then four 0,1s long pulses, that is, the regular pulse lengths; and a 10 s long first pulse, then four 0,1 s long pulses. It was expected that this extra long exposure in the first step might fill in all the nucleation sites, then the islands would start to grow. The resulting morphologies are shown in Fig. 5.3.

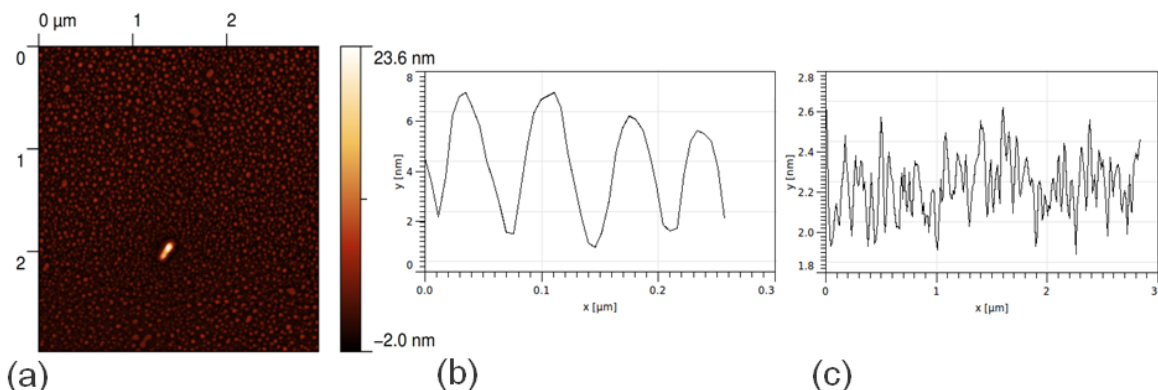


Fig. 5.3. AFM micrographs of ZnO on Si 150°C with extra long initial exposures. a: 1s first cycle, then 4 regular ones. b: the profile of the morphology shown in a, c: the profile of the morphology of the sample with 10s long first cycle, then 4 regular ones.

It can be seen from Fig. 5.3. that the 1 s long exposure in the first deposition cycle increased the number of islands considerably. After this nucleation period in the further cycles the islands grew. The resulting islands are smaller both in diameter and in height than those deposited with the traditional (uniform 0.1 s long) pulse lengths. In the case of the 10 s long first pulse the result of the 5 cycles is a continuous layer with a much smaller surface roughness than usually experienced on ALD deposited polycrystalline layers. This is the method to deposit ultra thin and smooth polycrystalline ZnO films. This phenomenon is unknown in the literature of atomic layer deposition. The 0.1 s exposures are sufficient at all temperatures for a saturation of the surface. According to the literature of the ALD method, if saturation has been achieved, all bonding sites available on the surface become occupied, and there is no need for further exposure. The 0.1 s pulse lengths results in the required saturation and partial pressure of the precursors therefore it is a completely unexpected result, that only in the case of the first deposition cycle a longer

exposure results in higher coverage of the surface. Although there are still available bonding sites on the surface, it takes several cycles for the nucleation to complete. Longer exposures have previously only been used in the case of high aspect ratio structures, not on smooth surfaces.

The layers deposited on GaN can be seen in Fig. 5.4. On this substrate the layers grow layer-by-layer at all deposition temperatures. Fig. 5.4.a shows the surface of the reference GaN layer. The morphology of the ZnO layer follows the substrate morphology exactly (see Fig. 5.4.b). The coverage was full and complete already after 5 cycles at every substrate temperature. It can be seen in Fig. 5.4.c that the profile of the surface follows the atomic terraces of the layer. By choosing the right temperature even an epitaxial growth is possible on GaN substrates.

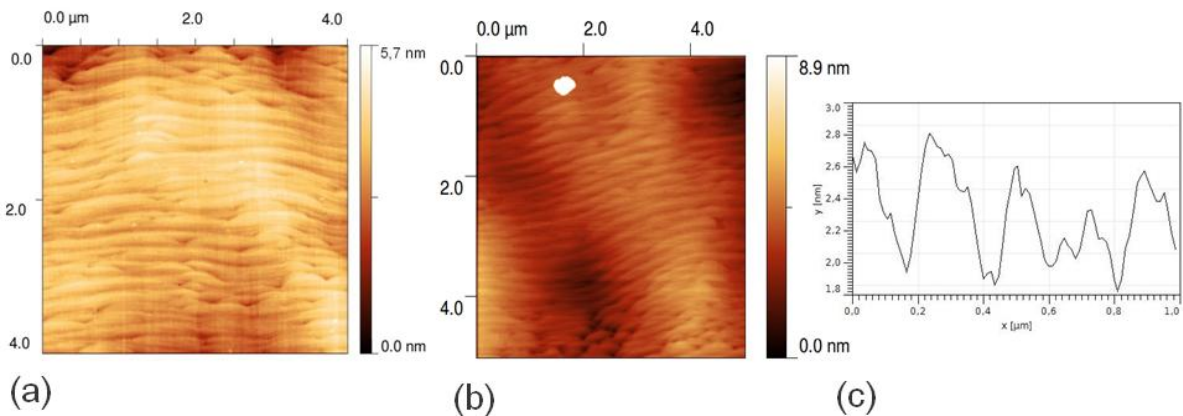


Fig. 5.4. The growth of ZnO on GaN according to the AFM measurements: a: GaN reference surface, b: ZnO layer after 5 (0.1s long) pulses, c the profile of the layer shown in Fig. 5.4.b

The comparison of the results with SEM and EDS measurements showed a uniform ZnO elemental distribution on the surfaces of all the GaN substrates, and the ZnO concentration increased with the increasing pulse numbers.

The ZnO layers grown on sapphire substrates showed a very interesting feature: the growth mode could be controlled by the temperature. At 150°C the growth is very similar to that on Si. The extremely smooth surface of the sapphire substrate (Fig. 5.5.a) is scattered with islands after 5 deposition cycles (see Fig.5.5.b). After 15 cycles the layer was already continuous. At temperatures at and above 220°C on the other hand the growth was completely different. A layer by layer growth occurred: continuous layers can be seen already after 5 deposition cycles. The XRD results revealed highly oriented, almost epitaxial layers. The orientation was mainly (002), with only a small (101) peak visible, whereas in a powdered ZnO sample the (101) is the highest intensity peak.

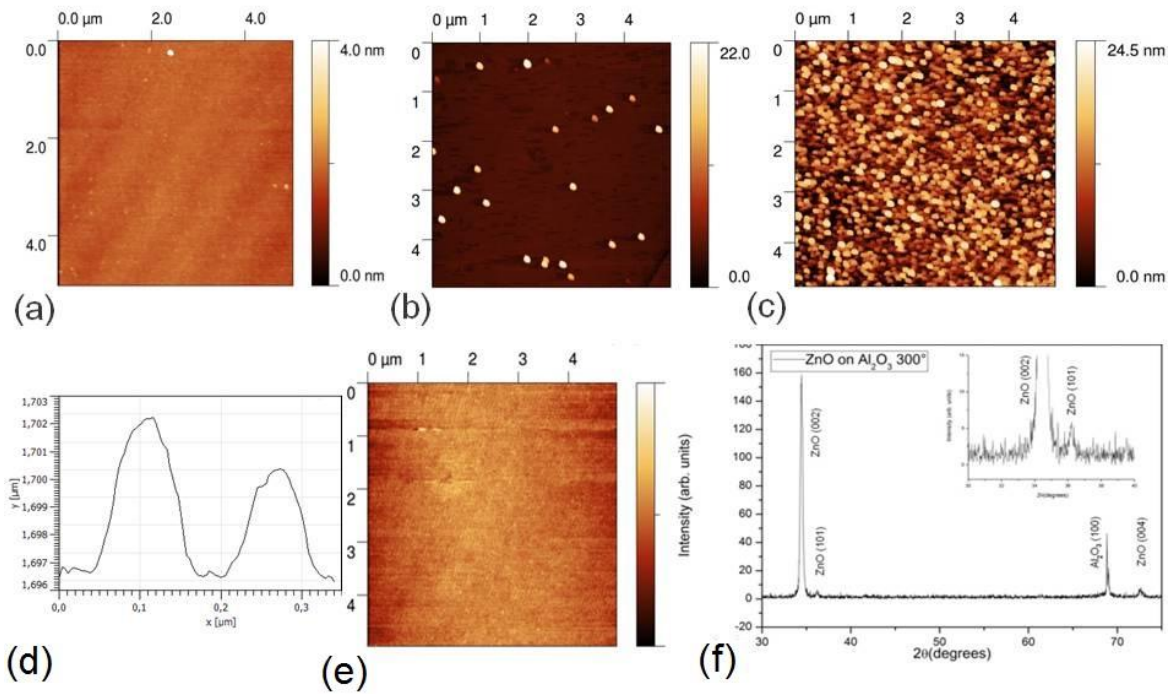


Fig. 5.5. The growth of ZnO on sapphire according to the AFM measurements: a: sapphire substrate surface, b: the layer after 5 cycles of growth at 150°C, c: after 15 cycles at 150°C, d: the profile of the surface shown in b, e: 5 cycles at 300°C, f: the XRD results of the layer

On graphene there was no ZnO growth at all, even after 500 cycles the graphene substrate was completely inert. Further experiments were not tried, as this result was by no means unexpected, as on such inert substrates there are no connection sites for the ALD growth. To succeed in ZnO growth on graphene, further experiments are required, including some functionalization of the graphene surface [5.2,5.3].

5.2 The growth of ALD ZnO

The average growth rates of ~70 nm thick ZnO layers deposited on Si were determined. It was found to be a function of the deposition temperature: it is 1.07 Å at 120°C, then increases. The maximal growth rate is at 150°C: 1.9 Å, then it decreases at higher deposition temperatures. At 300°C the growth rate was only 0.9 Å. The number of mono-layers grown in one deposition cycle may be calculated from this, but one must also consider that the orientations are different at the different deposition temperatures. As ZnO grows in a hexagonal wurtzite structure, with the lattice constants $a=3.5$ Å, and $c=5.25$ Å, therefore the distances of the atomic mono-layers are $d=2.81$ Å if the layer grows perpendicular to the c axis, and $d=2.5$ Å if it grows parallel to the c axis. At lower temperatures the layers grow in the (100) crystallographic direction, that is perpendicular to the c axis, at higher temperatures it grows in the (002) direction, parallel to the c axis. Therefore the number of mono-layers deposited in one deposition cycle can be calculated considering the atomic spacings. These results are shown in Fig. 5.6.

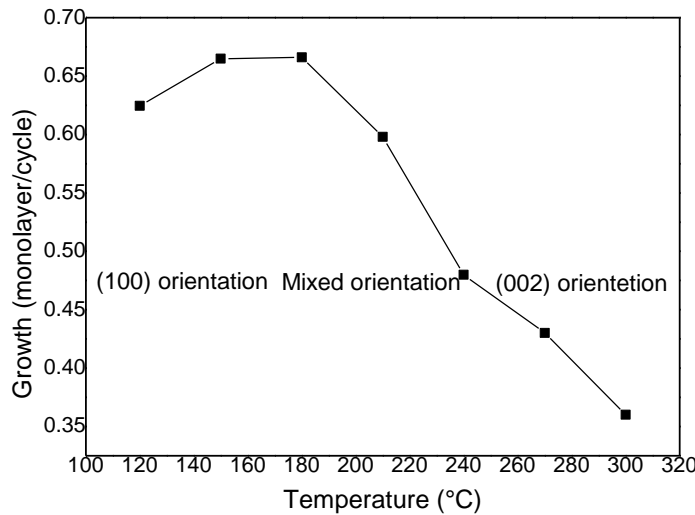


Fig. 5.6. The mono-layer/ cycle rate of ZnO growth at different temperatures

If we consider that during chemisorption the bonding sites are the OH groups on the surface, in the (100) case the sites are at 5.2 Å distance from each other, while in the (002) case this spacing is 3.25 Å. In the diethyl-zinc precursor molecules the Zn-C bond length is 1.95 Å. After the DEZ molecule connects to the surface it releases one ethyl group, therefore the radius of the remaining specimen is around 2 Å. This means that in the (100) case the molecules definitely have ample space to connect to each site, and no steric hindrance has to be taken into account. The packing density calculated merely from the molecular structure should be one, and so the growth rate should be a mono-layer/cycle. In the (002) case, the atomic spacing is close to the size of the adsorbates. Depending on the repulsion of the neighbouring molecules it is also likely that they reconfigure in the next closest packing structure. This may be one of the hindering processes that decrease the growth rate at the higher temperatures. The other one is that with increasing the temperatures the number of OH groups decreases, and that at higher deposition temperatures the adsorbed specimen may desorb once again.

The growth rates on Si were 1.2 times that on GaN at all deposition temperatures. Obviously, the mechanism of the adsorption, and the chemical processes must be the same at a given temperature independently of the surface. (In case full coverage has already been achieved.) The morphologies of the layers grown on Si and GaN are very different. As seen in Fig. 5.1. the layers grown on Si have a surface roughness of a few nanometres, while the surface of the ZnO layers grown on GaN is extremely smooth, except for the small roughness that already the substrate possessed as well. It is fair to suppose that the larger growth rate on the nominal surface of Si samples is then the result of the larger surface area resulted by the larger roughness of the grown layers.

The very small roughness of the GaN surface, and thus the ZnO films grown on it can be approximated with a surface covered by cylinder sections with 10 nm height and 1000 nm width lying parallel to the surface. The actual surface area this morphology yields an only 1.0004 times larger surface than an ideally flat one.

On the other hand the morphology of the ZnO surface can be approximated with a surface covered with domes, or sphere sections that can be seen in Fig. 1.a. The domes are 10 nm in height and 60 nm in diameter. It is reasonable to assume that the full coverage means that these same domes cover the whole surface. A close packed ordering can be achieved assuming a tetragonal ordering of the domes, and adding an extra one in every gap between four others, so that the top of each sphere section is 10 nm high from the substrate surface. The surface area of this morphology can be calculated, and it increases the surface by a factor of 1.08. The increase of the surface area accounts for a part of the increasing growth rate. The other effect enhancing the growth rate is probably the increased number of defect sites and kinks. It can also be seen in the figure, that as the spheres cover each other partly, this assumption results in the typical ALD deposited ZnO film seen in the AFM micrographs with a surface roughness of a few nanometres. Therefore the coalescence of the 10 nm high islands also accounts for the roughness and morphology of the ALD grown polycrystalline layers on Si.

As a conclusion the growth always occurs layer by layer on GaN and an epitaxial growth is also possible with proper deposition parameters. The growth type on sapphire can be tuned by the deposition temperature. The island-like growth of ZnO on Si is a result of nucleation issues, which can be solved by an extended first pulse time. As the thus achieved films have a smaller surface roughness, the growth of thinner continuous layers is also possible with this method.

The higher growth rates on Si than on GaN under the same deposition conditions can be explained by the different surface morphologies and the different growth modes on these two substrates.

6. The growth of epitaxial ZnO layers

The motivation for this research was the need for conductive epitaxial layers for the purpose of seed layers for hybrid solar cells and optoelectronic devices. The fabrication of these structures requires a conductive seed layer of ZnO. From this seed layer a hydrothermal growth of nanorods is possible, which grow epitaxially, therefore they follow the crystalline structure of the seed layer. If an ordered structure of the nanorods is required, then the seed layer needs to be epitaxial. This way they will not only be normal to the surface, but they will even have the same orientation.

The experiments on the nucleation of ZnO showed that an epitaxial growth is possible at 300°C deposition temperature, but not at 240°C. On the other hand the ZnO layers with the best conductivity were deposited at and under this temperature. It was also interesting to examine the effect of doping on the epitaxial growth, as this has not been previously examined. In theory ZnO can grow epitaxially on sapphire substrates as well, therefore it would be possible that the Al₂O₃ and ZnO multi-layers might also grow epitaxially. On the other hand the ALD grown Al₂O₃ tends to form amorphous layers. In this case –depending on the concentration- it would gradually deteriorate the crystalline structure. The aim of this work was to see how well conductive epitaxial layers can be formed.

The layers were deposited in the previously described ALD system. The substrates were 6 µm thick GaN layers epitaxially grown on sapphire substrates. The substrates were cleaned in acetone and ethylene and 5 MΩ de-ionized water.

The ZnO layers were deposited at 300°C and 270°C, as epitaxy was expected to be possible at these temperatures. Double layers were also grown with a thin (200 cycle) buffer layer grown at 300°C and a thicker (400 cycles) one at 210°C. It was expected that the epitaxial buffer layer grown at 300°C would force the top layer to also grow epitaxially, and the layers grown at 210°C have previously proved to be conductive. Therefore these layers were expected to be epitaxial with a fairly low resistivity. The Al doping was kept fairly low in all cases. Even just one cycle of Al doping in the middle of the layer was tried. The samples prepared are summarised in table 7.1.

After the layer deposition the resistivity of a number of layers was measured. On these samples contacts were fabricated with silver paste, then reinforced with epoxy glue. The ZnO layers were removed from the back side of the samples with HCl, so that the layer would only be on the top side of the GaN, and the contacts could be placed on the actual side of the layer. The resistivities were measured in the Van der Pauw configuration.

The thickness of the samples was measured with a profilometer. The thicknesses were found to be 75% of those grown on silicon substrates under the same growth conditions. The specific resistivities and the mobilities were calculated using these measured thickness values. The samples are listed in Table 7.1.

	Deposition cycles
1	300°C 21* (21 cycles ZnO+ 1 cycle Al ₂ O ₃)+21 cycles ZnO
2	300°C 200 cycles ZnO+210°C 12*(50 cycles ZnO+ 1 Al ₂ O ₃)+ 50 cycles ZnO
3	300°C 200 cycles ZnO+210°C 17*(21 cycles ZnO+ 1 Al ₂ O ₃)+43 cycles ZnO
4	270°C 16*(30 cycles ZnO+ 1 Al ₂ O ₃)+ 20 cycles ZnO
5	300°C 12* (50 cyclesZnO + 1 Al ₂ O ₃)+ 50 cycles ZnO
6	270°C intrinsic 550 cycles ZnO
7	300°C 200 cycles ZnO+210°C 400 cycles ZnO
8	300°C 600 cycles intrinsic ZnO

Table 6.1 The deposition cycles of the different samples

6.1 The deposition of epitaxial layers

The deposition of epitaxial layers was attempted at temperatures varying between 150°C and 300°C. The crystallinity of the layers was determined with XRD. The measured $\Theta/2\Theta$ curves of three representative samples deposited at 150°C, 220°C and 300°C are presented in Fig. 6.1.

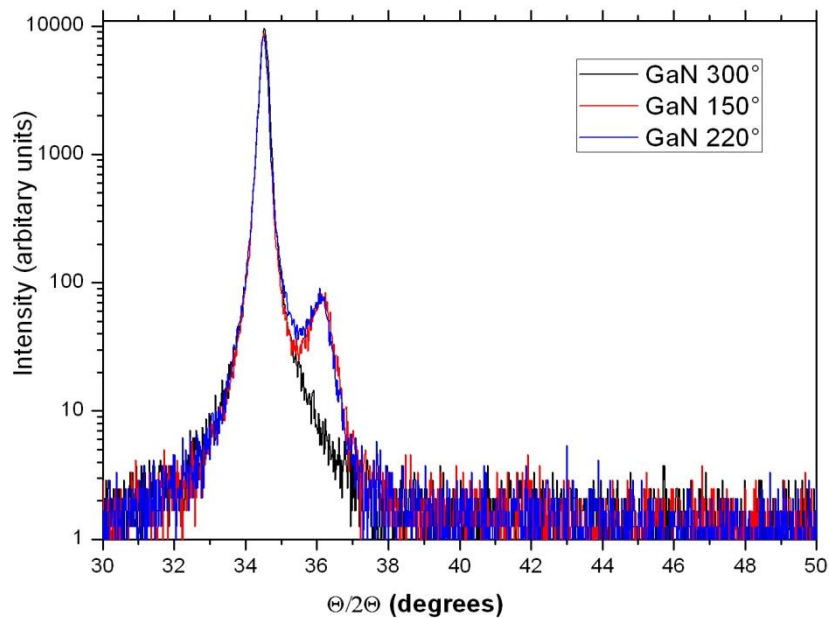


Fig. 6.1. XRD $\Theta/2\Theta$ spectra of the samples deposited at 150, 220 and 300°C

The XRD spectra of the samples are dominated with the strong GaN (001) substrate peak at $2\Theta = 34.56^\circ$ which almost perfectly overlaps with the ZnO (002) peak at $2\Theta = 34.421^\circ$. The results show that the intrinsic ZnO layers grown at 150 and 210°C have both (002) and (101) peaks. The $\Theta/2\Theta$ curves of the samples deposited above 270°C show no additional peaks to that of the GaN substrate. This leads to the conclusion that if they are crystalline, they have an epitaxial structure following the (001)

orientation of the GaN substrate. All the layers possessed the typical peaks as presented in Fig. 6.1. In the case of the films deposited under 270°C the (101) peak of ZnO at $2\theta = 36.252^{\circ}$ is also apparent while neither the (100) at $2\theta = 31.769^{\circ}$ nor the (102) at $2\theta = 47.568^{\circ}$ was observed showing that these layers are not epitaxial, but only some specific orientations are present.

To make sure that the layers deposited at higher temperatures are indeed epitaxial, and to further examine their crystalline quality, regular and high resolution TEM images were taken on the intrinsic ZnO layer grown at 300°C . These images can be seen in Fig. 6.2.a and 6.2.b. The TEM micrographs clearly reflect that the ZnO film followed the structure of the GaN substrate precisely. The films are high quality and epitaxial.

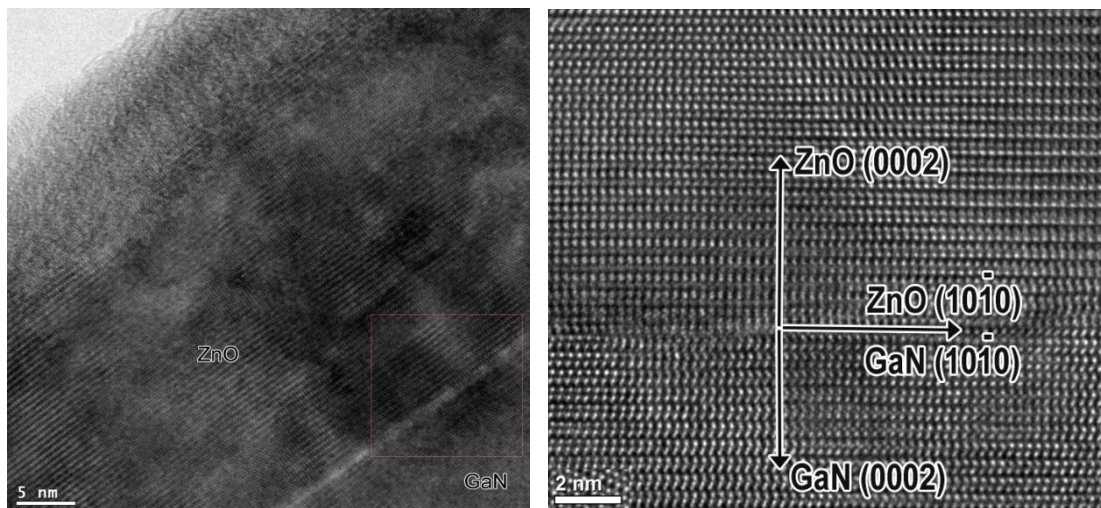


Fig. 6.2. a and b: The TEM micrograph and the high resolution TEM image taken on the sample deposited at 300°C

Reciprocal space mapping of the (104) lattice point was also conducted on the samples deposited at 270°C , and the intrinsic double layer. These maps are presented in fig. 6.3. a and b. It is obvious from these images that the layers are perfectly epitaxial without any strain.

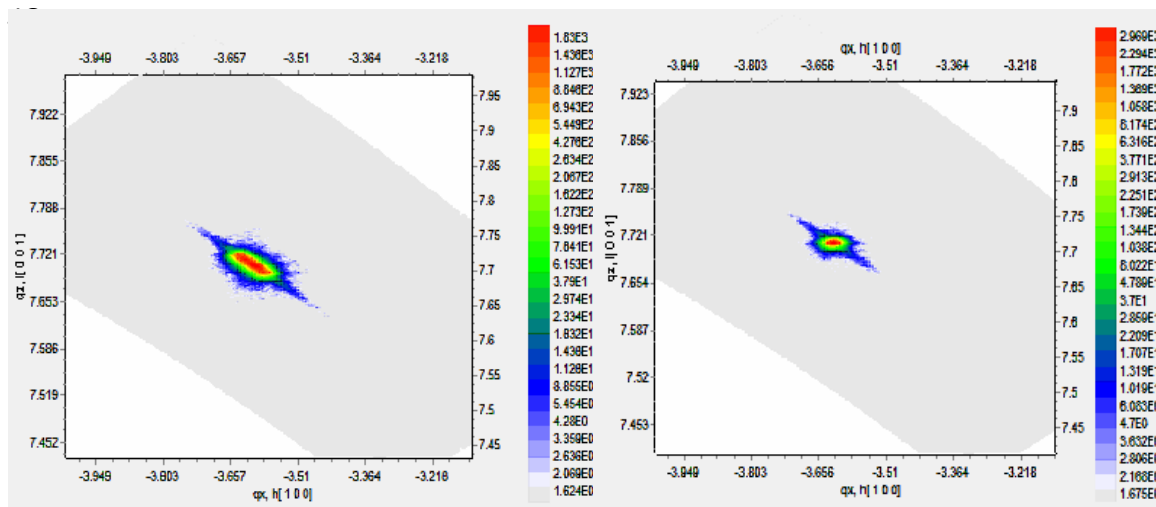


Fig.6.3. The reciprocal space maps of the epitaxial ZnO layer grown at 270°C (a), and the intrinsic double layer.

6.2 The effect of the Al doping on the crystallinity

1. 300°C 21 AlOx layers	(001) oriented, but a small (101) peak also apparent
2. double layer 12 AlOx	(001) oriented, but a small (101) peak also apparent
3. double layer 17 AlOx	(001) oriented, but a small (100) peak also apparent
4. 270°C 16 AlOx layers	(001) oriented with both (100) and (101) peaks
5. 300°C 12 AlOx layers	(001) oriented with both (100) and (101) peaks
6. 270°C intrinsic	Epitaxial in the (001) orientation
7. intrinsic double layer	Epitaxial in the (001) orientation
8. 300°C intrinsic	Epitaxial in the (001) orientation

Table 6.2 The crystallinity of the layers

The crystalline quality of the doped layers was also very good. These layers are still highly oriented, continuous and uniform but they are not perfectly epitaxial any more. They appear to be oriented in the (001) direction, but they also have peaks at $2\theta = 31.77^\circ$ and 36.25° displaying the (100) and the (101) reflections of ZnO, respectively. This shows that even though these layers are not polycrystalline, they must contain crystallites with orientations other than that of the GaN substrate. The XRD results from the layers are presented in Table 6.2. and Fig. 6.4.

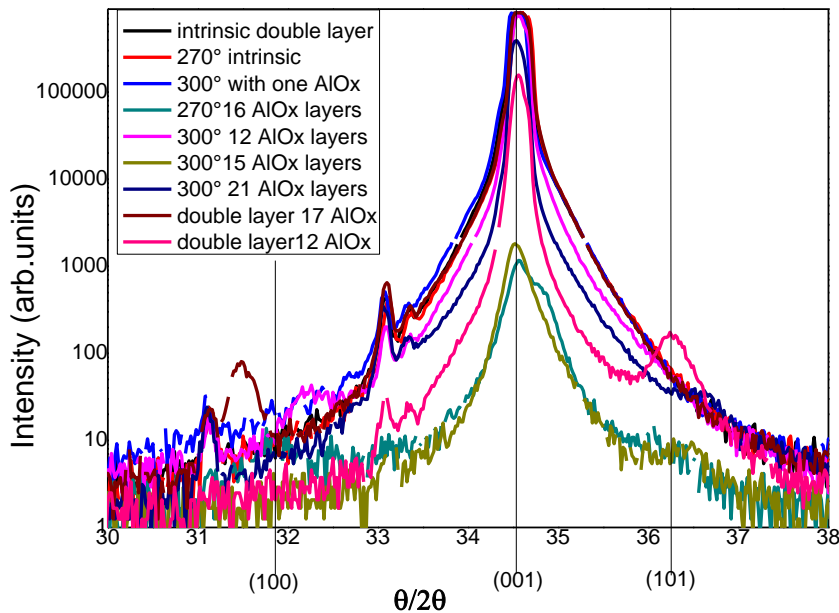


Fig. 6.4. The XRD results of the Al doped samples

Somewhat contradictory to the XRD findings, the reciprocal space map taken from the (004) peak of the doped double layer (presented in Fig. 6.5.a) still showed a perfect epitaxy. Therefore to determine if the doped samples are still mainly highly oriented with some crystallites in other orientations, or they are completely polycrystalline, in other words, to see, how much of the surface of the layers was oriented differently, EBSD experiments were conducted. The result of the ZnO film deposited at 300°C and doped with 12 AlO_x sublayers is presented in Fig. 6.5.b.

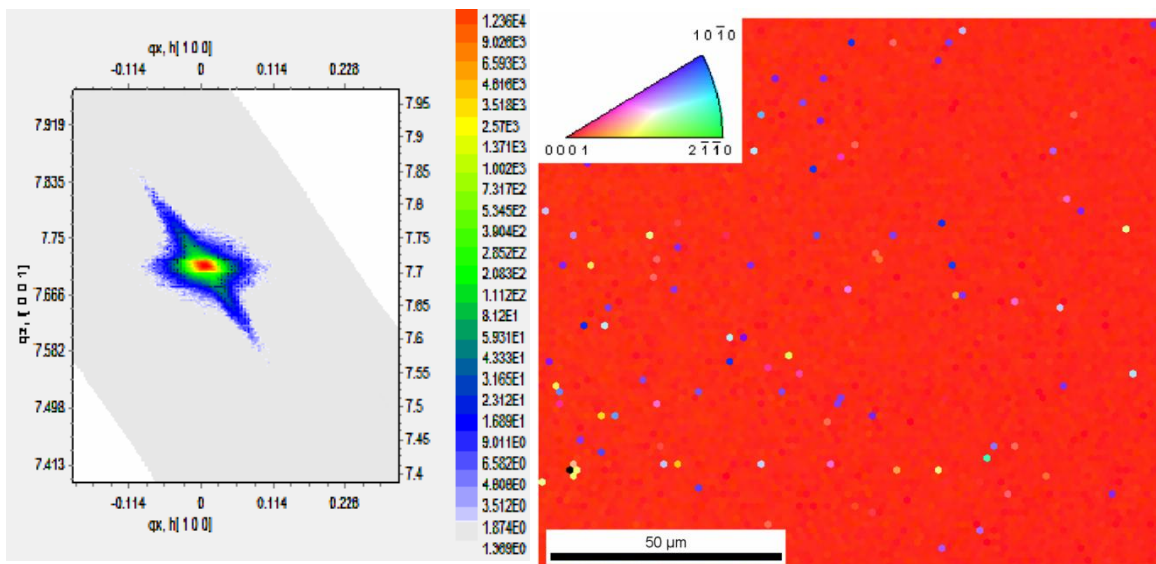


Fig. 6.5.a and b. the reciprocal space map and the EBSD map of the double layer doped with 12 AlO_x sublayers, respectively

It can be seen that most of the sample surface shows a (001) orientation following the crystalline orientation of the GaN substrate. Only small domains have the c axis parallel to the surface.

6.3 The conductivity of the films

The list of the deposited layers and their measured resistivities, carrier concentrations and the calculated mobility values are listed in Table 6.3. The resistivities of all the samples are very low. The mobility values are very high, compared to the literature values listed above, these are around the maximum achievable mobility values for epitaxial ZnO films. The surprising quality of these layers is the very high carrier concentrations. These values are already very high in the undoped layers and could not be considerably increased with the Al doping.

One possibility to explain this high value of carrier concentration was to suppose that the intrinsic doping –that is, the oxygen vacancies, zinc interstitials and hydrogen doping- was so high in these layers. This is somewhat in contrast with the high crystalline quality of the layers, as these unintentional dopants in ZnO are contaminations and defects that would deteriorate the crystallinity of the layers. The other possible explanation would be that some Ga diffused into the ZnO layers. Ga is an even more effective dopant in ZnO than Al. Both Al and Ga diffuse in ZnO with a substitutional mechanism. In the temperature range of 750-1000°C the solubility of aluminium in zinc oxide is $n = 1.0 \times 10^{23} \exp(-1.08 k^{-1} T^{-1})$ ions/cm³ and the solubility of gallium is $n = 2.7 \times 10^{21} \exp(-0.59 k^{-1} T^{-1})$ ions/cm³, where the activation energies are in eV. The diffusion is dependent on their surface concentration, and their diffusion coefficients are $D = 5.3 \times 10^{-2} \exp(-2.74 k^{-1} T^{-1})$ cm²/sec for Al, and $D = 3.6 \times 10^4 \exp(-2.74 k^{-1} T^{-1})$ cm²/sec for Ga. [6.1]

Prepared layers	ρ (10 ⁻⁴ Ωcm)	μ (cm ² /Vs)	n (10 ²⁰ /cm ³)
300°C 21 AlOx layers	0.768	140.3107	5.8
double layer 12 AlOx	1.766765	93.09313	3.8
double layer 17 AlOx	1.67328	109.8582	3.4
270°C 16 AlOx layers	1.15065	104.45601	5.2
300°C 12 AlOx layers	1.215	88.690223	5.8
270°C intrinsic	1.4536	122.49771	3.5
intrinsic double layer	1.8228	118.23417	2.9
300°C intrinsic	1.4883	131.23194	3.2

Table 6.3. The layers with their resistivities, carrier concentrations and mobilities

The depth profile of the layers was measured by SNMS and the proof of Ga in-

diffusion was indeed found. The measurements are presented in Fig. 6.5. The straight line shows simulation results of the elemental distribution in case of no interdiffusion. It can be seen, that the zinc, oxygen and nitrogen concentrations are in fact on this line, whereas the Ga diffused into the ZnO layer. The Ga concentrations are between 1% (near the interface) and 0.01% (on the front side, near the middle).

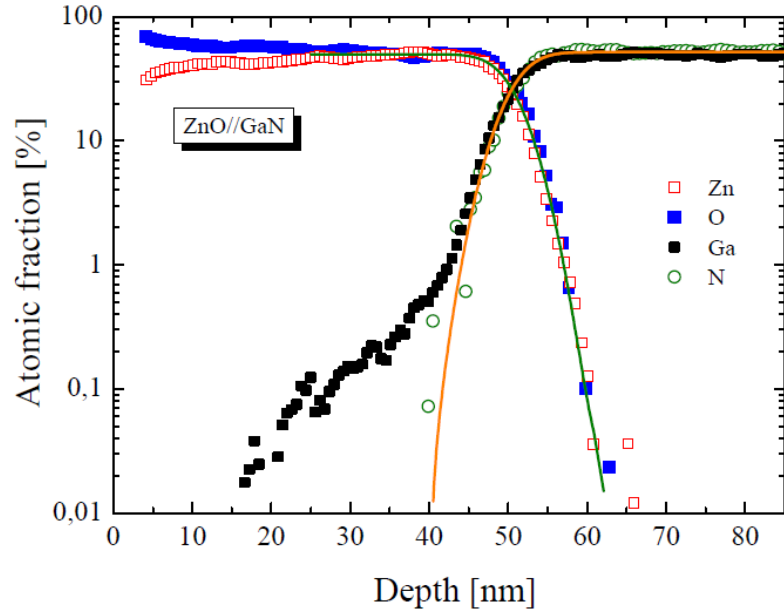


Fig. 6.6. The depth profile of the layers as measured by SNMS.

As a conclusion the layers deposited above 270°C tend to be epitaxial, but an epitaxial seed layer deposited at high temperatures ensures that the top layer grown at lower temperatures also grows epitaxially. In the case of the Al doped layers small domains with a different orientation also appeared. All the layers had high conductivities resulted by the high mobility due to the excellent crystalline structure and the high carrier concentrations. The latter is caused by the diffusion of Ga atoms into the layer, therefore a further Al doping cannot further reduce the resistivity.

7. Deposition of CIGS layers with post selenization of the metallic components

The aim of this work was to find new, simple and cheap ways of fabricating CIGS material by co-evaporating Cu, In and Ga from a single source followed by post-selenization; and to study the effects of the morphology and the selenization parameters on the CIGS material.

CIGS layers were deposited by the selenization of metallic components. To study the effect of the morphology and structure on the resulting CIGS structure a number of deposition methods have been examined. First a sequential deposition of metallic components was attempted with a number of different deposition sequences. This made it possible to examine how the order in which the metals are deposited affects the resulting film qualities. The sputtering and evaporation of the sequentially evaporated metallic layers took place in the complex vacuum system described in chapter 3.2.

As a second deposition method the evaporation of the three metallic components from a single evaporation source was developed. The method is similar to using an alloy-like source, except that the alloy only forms whilst heating the source. The evaporation of the metals is defined by their vapour pressure at a given temperature. According to the Raoult law the evaporation rate of the different components varies during the process, therefore the composition of the layer may also vary with time. The quantity of the material to be evaporated has to be chosen, considering, that in order to produce the required stoichiometric ratio, the whole content of the source needs to be evaporated, or the component that evaporates later remains in the source. This flash-like evaporation took place in the VEB Hochvakuum Dresden BL 25 instrument described in chapter 3. To avoid the alloying of Ga with the Ta boat, the Ga and In pieces were placed onto a thin Cu foil. This method was also advantageous since the evaporation of copper requires the highest temperature.

For the selenization of the consecutively deposited metals two different approaches have been tried. The evaporation of selenium on top of the layers and a consecutive annealing to enable the Se to diffuse into the layers, so the transformation of the components to CIGS layers could take place. This process took place in a vacuum evaporation chamber dedicated for this purpose. The background pressure was $\sim 10^{-6}$ mbar. The source was a resistivity heated W boat. The estimated temperature of the source was 800°C. The substrate temperature was 430°C during evaporation. The selenium source was Se pellets.

With this method, as it will be shown in the next chapter, the Se could not diffuse into the whole depth of the layers, therefore homogeneous CIGS layers could not form throughout the entire depth of the layer. The other method therefore was to anneal the metals in Se atmosphere. To do this, some of the CIG samples with Se pellets were sealed into glass capsules evacuated to 10^{-2} mbar, and heated for 5, 10, 15 or 20 minutes to 500°C and in order to achieve the $\text{Cu}(\text{In},\text{Ga})\text{Se}_2$ phase.

The substrates in use were 2 cm x 2 cm soda lime glass pieces and 1 cm x 1 cm Si squares. They were all cleaned in cc. HNO_3 and $5\text{M}\Omega$ de-ionised water before the

layer deposition. The substrate temperature did not exceed 50°C during evaporation. Table 7.1. shows the prepared samples.

1	In	Ga	Cu	Selenization with Se evaporation and annealing
2	Ga	In	Cu	Selenization with Se evaporation and annealing
3	Cu	In	Ga	Selenization with Se evaporation and annealing
4	Cu	Ga	In	Selenization with Se evaporation and annealing
5	In	Ga	Cu	Selenization with Se vapour
6	Ga	In	Cu	Selenization with Se vapour
7	Cu	In	Ga	Selenization with Se vapour
8	Cu	Ga	In	Selenization with Se vapour
9	Cu+Ga+In evaporated together		Selenization with Se vapour for 5 minutes	
10	Cu+Ga+In evaporated together		Selenization with Se vapour for 10 minutes	
11	Cu+Ga+In evaporated together		Selenization with Se vapour for 15 minutes	
12	Cu+Ga+In evaporated together		Selenization with Se vapour for 20 minutes	

Table 7.1 The deposition sequences of the CIGS samples prepared by post selenization of metallic components

7.1 The morphology of the evaporated metals

The morphology of the sequentially evaporated metallic layers varied significantly depending on the order of the evaporated metals. Fig. 7.1. shows the SEM micrographs (column 1.) and the EDS maps (column 2.) of the sequentially evaporated components. It can be seen on almost all samples that the metals covered the substrates completely. The average grain size of the layers is 100-200 nm, but micron sized and tens of microns sized droplets could also be seen on some samples. In order to present all these morphologies, the SEM micrographs are presented with different magnifications. The comparison of the micrographs reveals the importance of the deposition order of the metals:

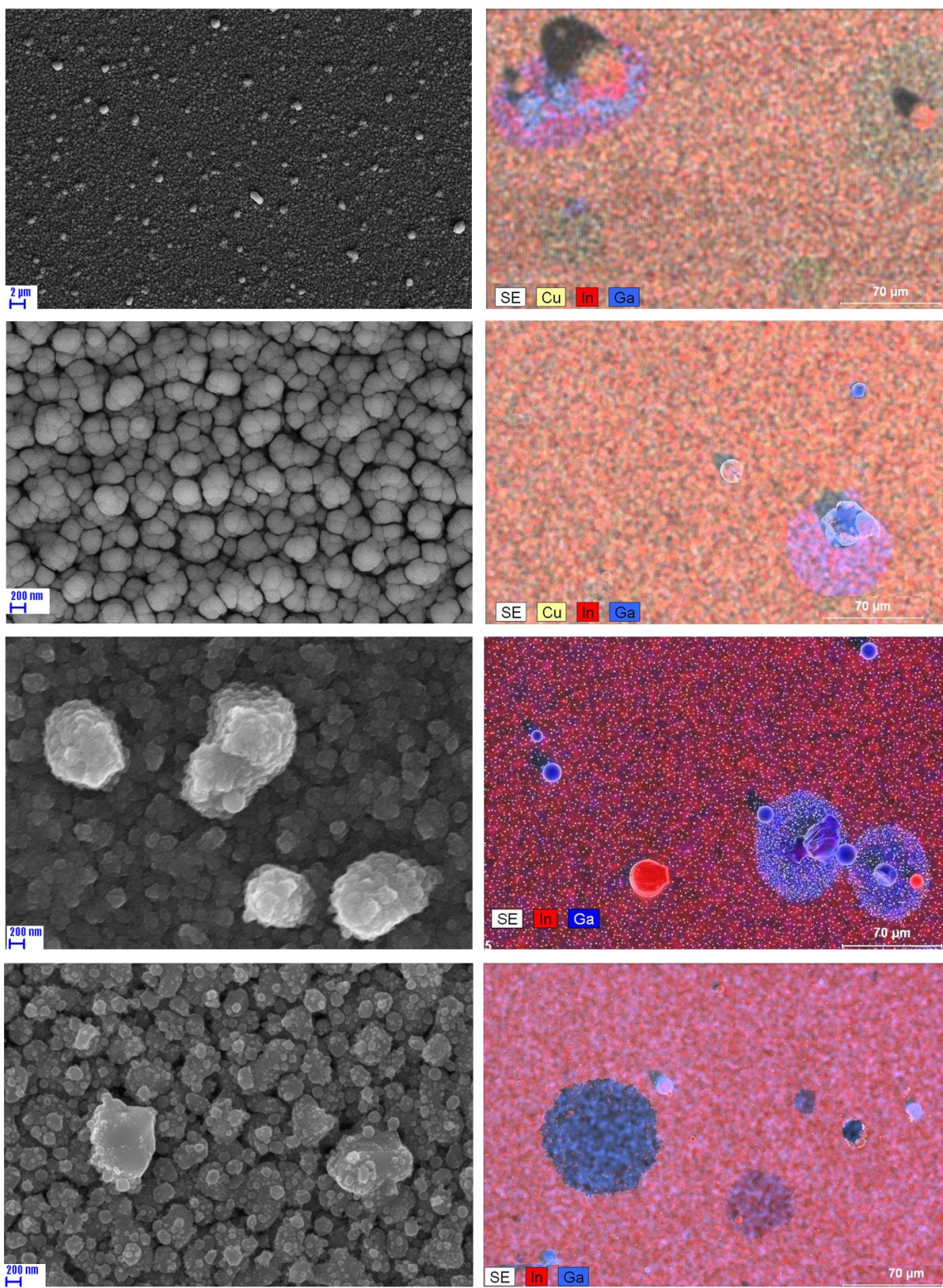


Fig. 7.1. The SEM micrographs (1. column) and element maps (2. column) of the evaporated metallic layers: sample 1, 2, 3 and 4 in the 1., 2., 3. and 4. rows respectively.

The first row of Fig. 7.1. shows the morphology of sample 1. The surface is scattered with 0.5-1 μm sized islands. On a larger scale (see the element map beside), 10 μm sized islands can be found on the surface. From the elemental analysis it turns out that the smaller objects are In grains, whereas the larger ones are Ga droplets. The origin of this morphology is that the In, when evaporated, forms droplets on the substrate surface. Then, in the case of this sample the Ga was evaporated, then the Cu sputtered on the surface. During sputtering the substrate temperature exceeded the melting point of Ga, which then diffused on the top of the layers. Thus, although the Cu sputtering took place after the Ga evaporation, some gallium droplets can be found on top of the evenly sputtered copper layer. This applies to all the cases where the evaporation were followed by the sputtering, and may be an advantage, as a higher Ga content in the top layer of the film results in an ideal band-gap profile, where the Ga rich sub-layers are near the surface resulting in a wider band-gap at the active region.

The SEM results of sample 2 can be seen in the 2nd row of Fig. 7.1. The Ga droplets are once again apparent, but as the larger scale image shows no In islands could be found.

The surface of sample 3. is presented in the 3rd row. In this case the In layer was evaporated on top of the sputtered copper layer, then the gallium was evaporated on top of that. This time the Ga was evaporated last, therefore the morphology is slightly different and the Ga islands are smaller.

The only sample where no Ga droplets could be found is sample 4. (see row 4.) The only inhomogeneities of this layer are the μm sized In grains. The element distribution of the layer reveals large In deficient regions.

Fig. 7.2. shows SEM images and EDS maps of flash evaporated CIG film. The elemental distribution of the metals was laterally inhomogeneous, and the morphology was very rough.

The secondary electron image (Fig. 7.2.a) displays a coarse surface morphology with micron sized hills. The EDS spectra of the distribution of In, Cu and Ga (Figs. b, c and d respectively) show that the indium formed micron size droplets on the sample, and these were then uniformly covered with granular layers of gallium and copper with an average granule size of 0.1 μm . The background of this morphology is that the indium evaporates first, as it does not wet the surface, it forms droplets. The other metals evaporate at higher temperatures, and cover this surface evenly.

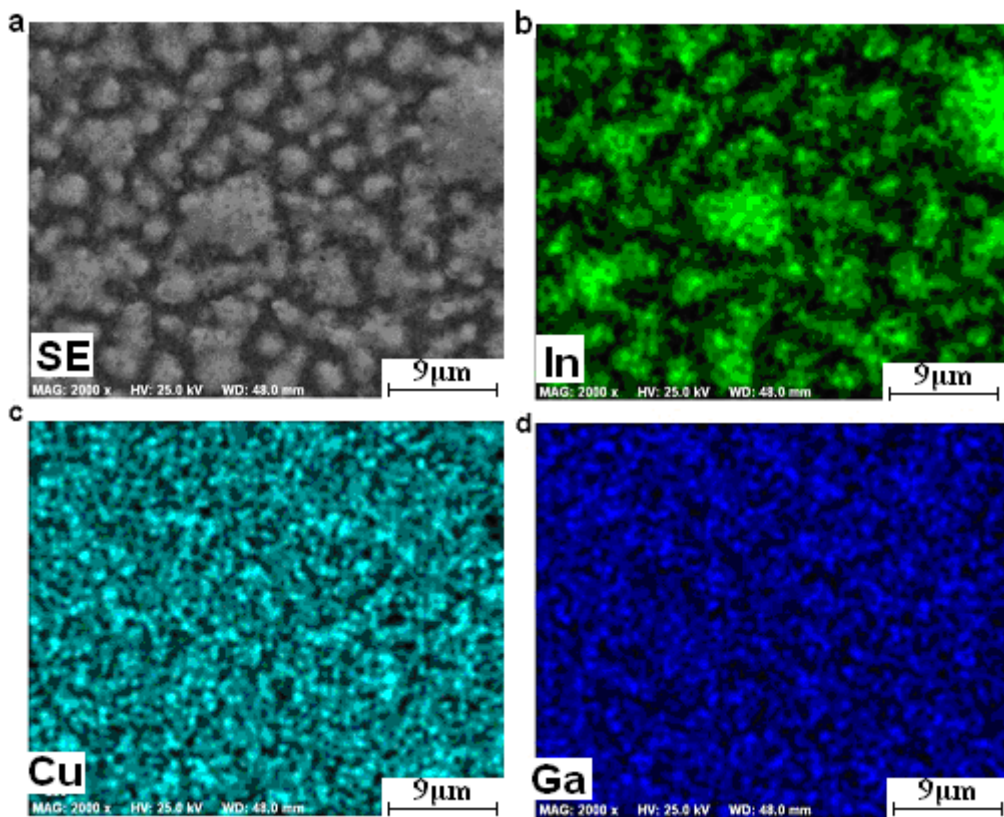


Fig. 7.2. SEM morphology and EDS maps of flash evaporated CIG film – a: secondary electron image, b: In, c: Cu, d: Ga distribution respectively

As a conclusion the morphology is very rough with every deposition method. The evaporated In always forms droplets on the surface. In the case of the flash evaporated samples the other metals were homogeneously distributed, while in the case of the sequentially evaporated samples the exact order of the evaporation had a crucial impact on the resulting morphology.

7.2 Post annealing of stacked metallic layers

Fig. 7.3. shows the SNMS Depth profiles (1. column) and the cross sectional SEM images (2. column) of the samples selenized with Se evaporation: samples 1, 2, 3 and 4 can be seen in the 1., 2., 3. and 4. rows respectively.

The SNMS results of the layers can be seen in the first column of Fig. 7.3. The results must be interpreted with some caution though, as due to the rough surface morphology of the layers the intensities from the surface layers may be somewhat misleading. This is also the reason why no depth scale can be calculated from these results.

In all cases the increase of the Mo yield indicates the bottom of the film. From the depth profiles the following observations can be made: The layers of the different

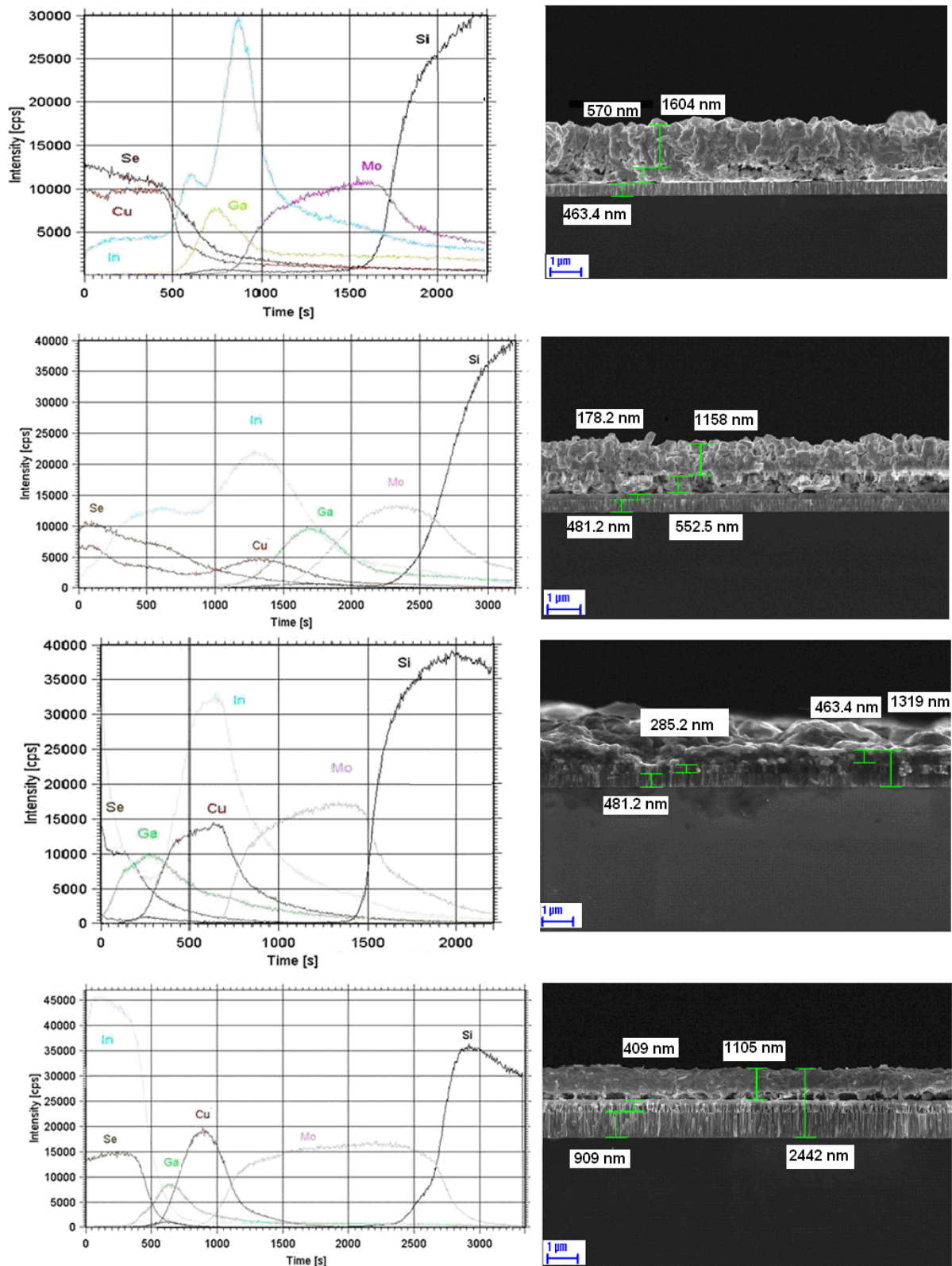


Fig. 7.3. The SNMS results (1st column) and cross sectional images (2nd column) of the consecutively evaporated layers with Se evaporation and post-annealing. Samples 1, 2, 3 and 4 in the 1., 2., 3., and 4. row respectively.

metals are still visible, in the original order of the deposition. Therefore the metals did not mix and alloy with each other sufficiently and the alloy formation is negligible at the temperature of the selenization. On the other hand, as the Se diffuses into the layer, a mixing and a reaction of the components starts, which can be seen from the way the In layers are always pulled towards the surface. In the Se containing top layer the In concentration rapidly increases in all cases.

Comparing these results with the cross sectional SEM images shown in the second column of Fig. 4.3, the thickness of the selenized CIGS layers and the unreacted metallic film that remained underneath may be determined. In sample 1 this means 1.4-1.7 μm CIGS on 500-550 nm thick metal under. In sample 2: 1-1.3 μm CIGS on 550-600 nm metallic layer. Sample 3 is the most uneven layer, with 1 μm high CIGS islands on an approximately 500 nm thick CIGS layer. There is also an about 300 nm thick metallic layer underneath. Sample 4: ~1 μm thick CIGS on ~400 nm metallic layer.

It is evident that the selenization was more effective in the samples where the Cu was at the top. Samples 3 and 4 have a much rougher morphology, with more unreacted metallic components remaining at the bottom.

The XRD measurements of the layers were evaluated using the following ICDD PDF records:

$\text{CuGa}_{0.3}\text{In}_{0.7}\text{Se}_2$: 00- 35-1102, CuInSe_2 : 00-40-1487, CuSe_2 : 00-26-1115, Cu_2Se :01-079-1841. The results are shown in Fig. 7.4, and the main observations are summarized in table 7.2.

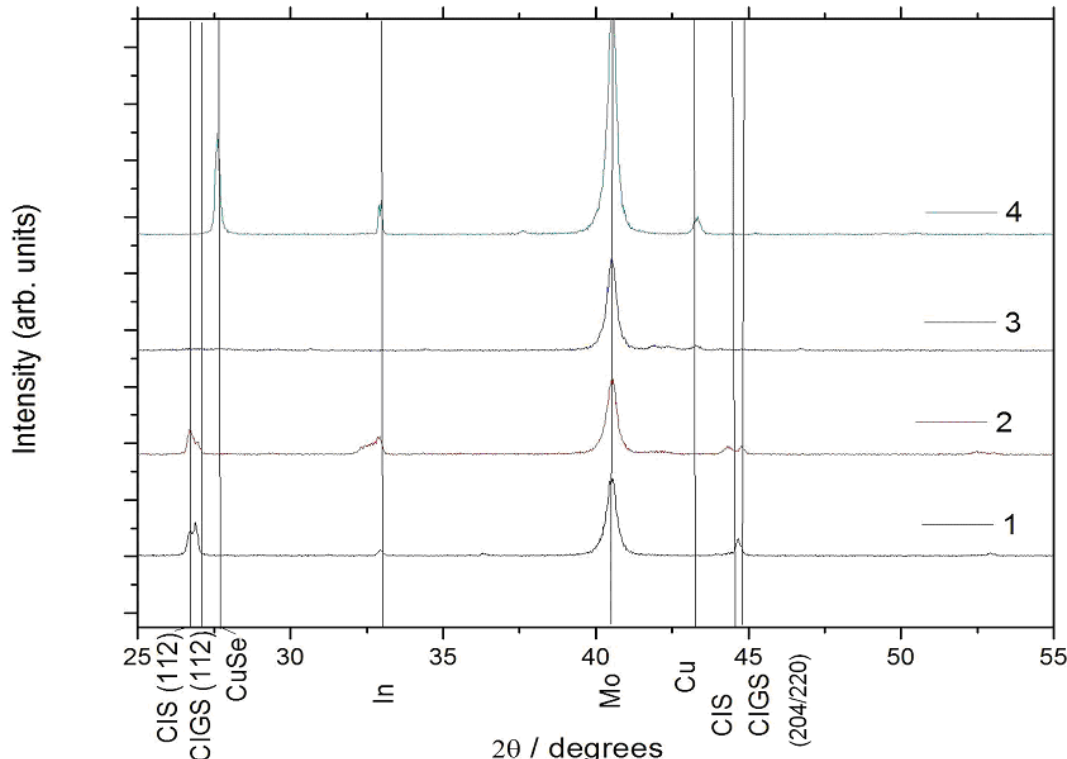


Fig. 7.4. The XRD results of the consecutively evaporated layers with Se evaporation and post-annealing

1	$\text{CuIn}_{0.7}\text{Ga}_{0.3}\text{Se}_2$ and CuInSe_2 phases with metallic In
2	CuInSe_2 phase dominates, with some $\text{CuIn}_{0.7}\text{Ga}_{0.3}\text{Se}_2$, and some metallic In
3	CuInSe_2 phase with (213) orientation apparent, but with small grains, and some Cu and In.
4	CuInSe_2 with In and Cu

Table 7.2 the XRD results of the post annealed samples

As conclusion, besides the CIGS and CIS phases selenides were formed and a portion of the metals remained unreacted at the bottom of the layers as can be seen in the SEM micrographs shown in fig 7.3. The reason for this effect is probably that not enough Se is evaporated on the layers, and at the annealing temperature a portion of the Se may even evaporate from the layer instead of diffusing into it.

7.3 Selenization of metallic components with Se vapour

As the Se evaporation and annealing did not result in a uniform depth profile of the Se content of the layers, a selenization in selenium vapour was attempted. For this purpose the 0.5 cm^2 sized samples were sealed in evacuated glass ampoules with Se pellets and annealed at 500°C for 15 minutes. The number of Se pellets was chosen so that during annealing the Se would be in excess.

Fig. 7.5. shows SEM micrographs of the samples after the selenization.

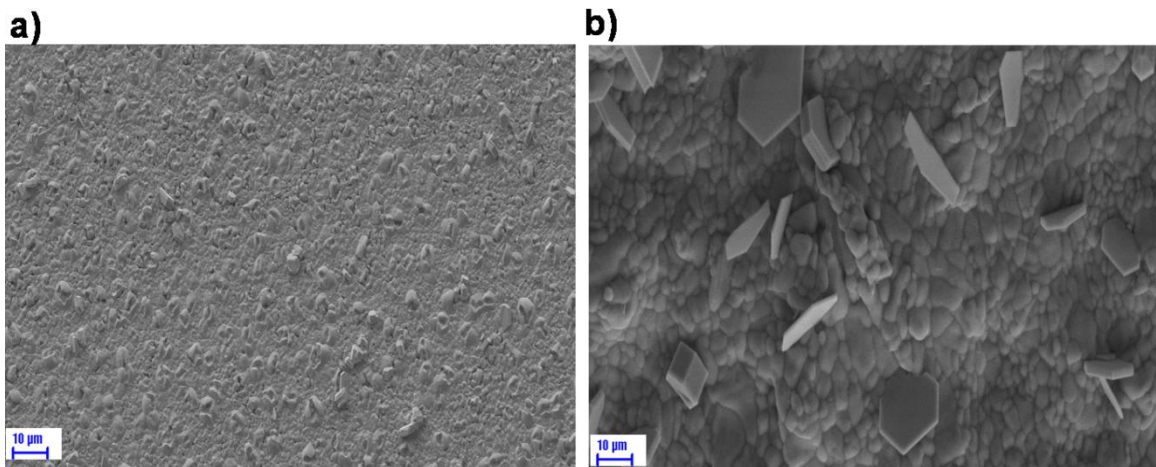


Fig. 7.5. a: the typical morphology of sample 5 and 6, b: the typical morphology of sample 7 and 8

All the samples became laterally homogeneous in composition. Samples 5 and 6 have a generally similar morphology (see Fig. 7.5.a). The circular („cauliflower-like“) grains usually found in CIGS films cannot be found here, therefore a denser, more uniform surface is resulted which is generally considered to yield more efficient

devices. Samples 7 and 8 have a similar morphology (Fig. 7.5b), except for the hexagonal crystallites scattered all over the surface.

The composition of the layers according to the EDS analysis is shown in Table 7.3. The composition of the layers corresponds to that of the CIGS material. As mentioned before, CIGS absorbers are not as sensitive to the precise composition, as e.g. the silicon based technologies. A few percents of differences could still result in functioning devices, but certain qualities may differ. The composition of sample 7 is nearest the ideal CIGS composition.

Sample no./component	Cu	In	Ga	Se
5	35.7%	15.5%	5.1%	43.7%
6	35.5%	15.7%	2.6%	46.1%
7	26.9%	17.8%	6.6%	48.8%
8	16.5%	29.5%	2.5%	51.5%
Ideal composition	25%	17.5-20%	5-7.5%	50%

Table 7.3. The composition of the sequentially evaporated and post selenized CIGS layers

Fig. 7.6. shows the SNMS results and the cross sectional images of the samples. All the layers are built up from two sub-layers with different morphologies: a bottom layer with a finer structure (grain size of a few tens of nanometers), and a top layer with a larger grain size in the micron range. This corresponds to a Ga rich sub-layer at the bottom of the film. In the films where the Cu was sputtered first (see sample 7 and 8 in Fig. 7.6. 3rd and 4th row) this difference is even more prominent. On the other hand the SNMS depth profiles (see Fig. 7.5 first column) show that the Se diffused into the full depth of all the layers, although their elemental distributions along the depth are not homogeneous. To understand the background of this phenomenon, the XRD results need to be analysed.

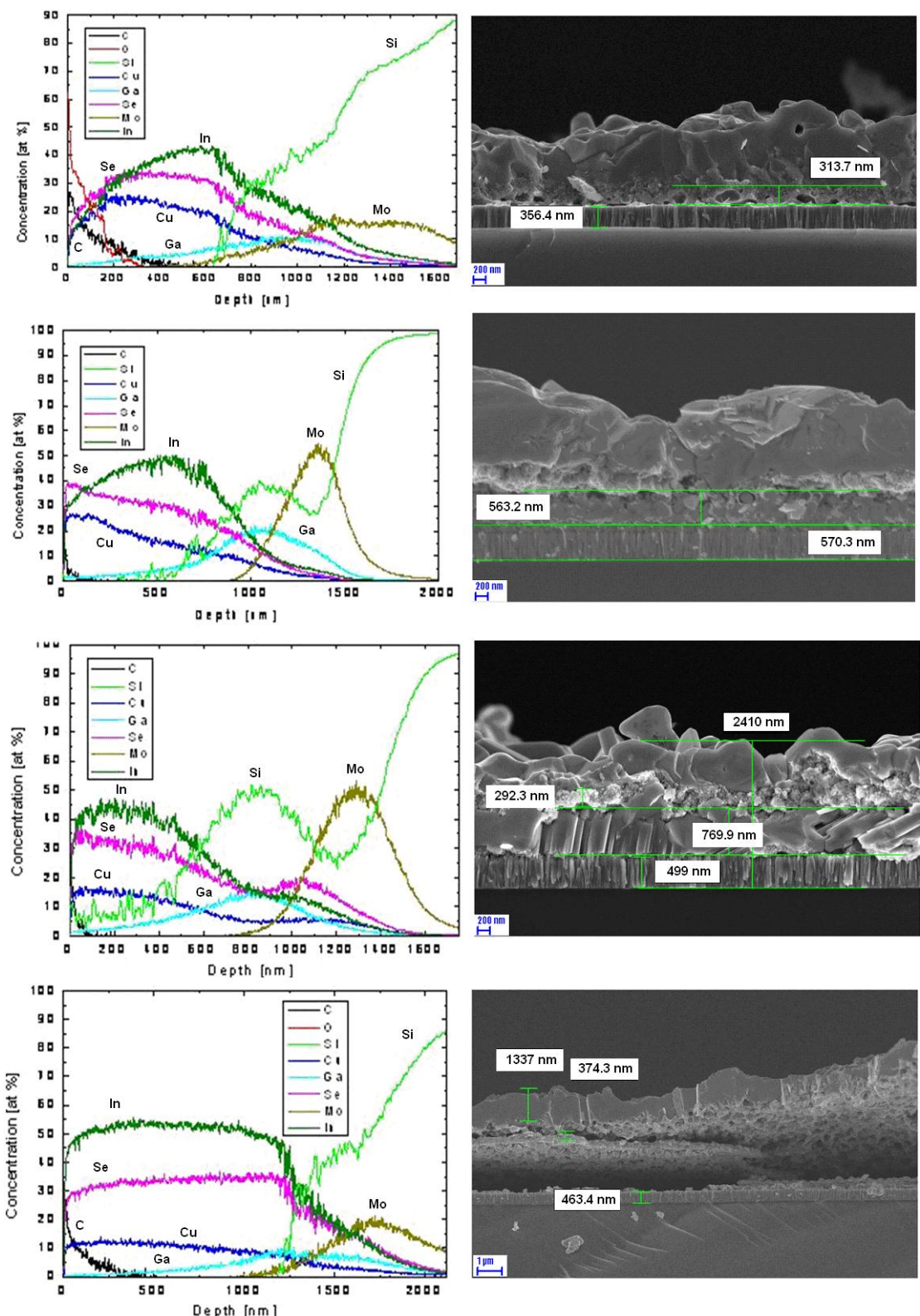


Fig. 7.6. The SNMS Depth profiles (1. column) and the cross sections (2. column) of the samples selenized with Se vapour: 1, 2, 3 and 4 in the 1., 2., 3. and 4. rows respectively.

The XRD experiments (see Fig. 7.7.) showed that all the layers contained chalcopyrite phase, some also had one of the metals in excess. A summary of the crystalline quality of the layers can be seen in Table 7.4.

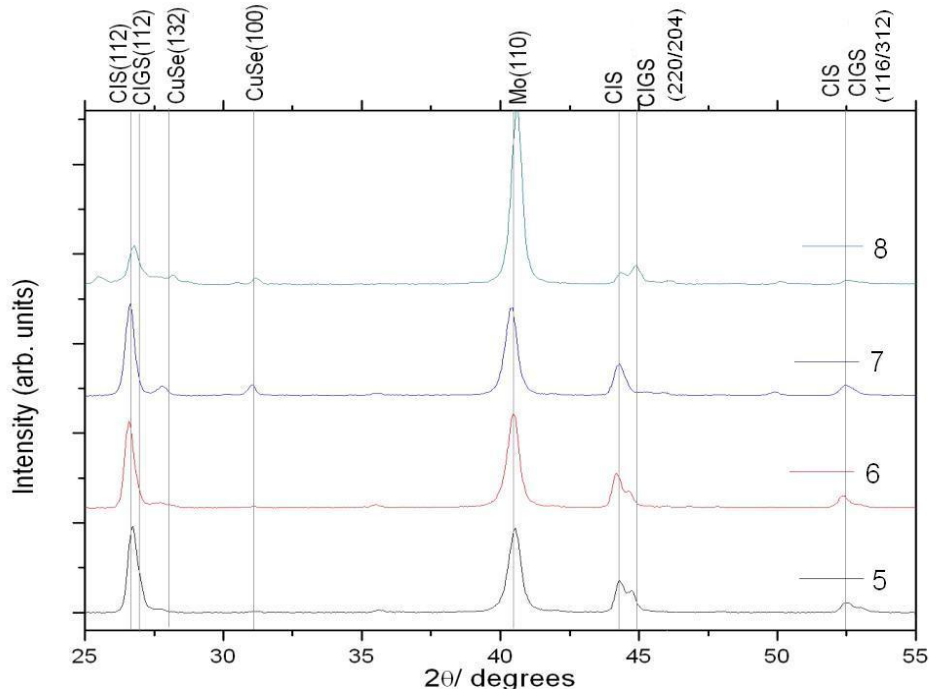


Fig. 7.7. The XRD results of the CIGS layers.

5	Predominantly $\text{CuIn}_{0.7}\text{Ga}_{0.3}\text{Se}_2$ with a little CuInSe_2 phase present.
6	Both CuInSe_2 and $\text{CuIn}_{0.7}\text{Ga}_{0.3}\text{Se}_2$ phases present, the CuInSe_2 phase more dominant than the CIGS.
7	Only one chalcopyrite phase present, that of $\text{CuIn}_{0.9}\text{Ga}_{0.1}\text{Se}_2$ with some hexagonal CuSe.
8	CuInSe_2 and $\text{CuIn}_{0.7}\text{Ga}_{0.3}\text{Se}_2$ phases with a little hexagonal CuSe present.

Table 7.4. The XRD results of the layers.

The absence of binary phases and the presence of the CuInGaSe_2 phase in the case of samples 5 and 6 indicate that the reactions were completed. The two different layers shown in the cross sectional images may be the CIS and the CIGS phases, therefore a phase separation must have taken place with the CIS at the top and the CIGS dominantly at the bottom of the layers. This was also proven as an elemental analysis along the cross sections of the layers showed higher Ga concentration toward the bottom of the layer.

In samples 7 and 8 the CuSe is still present. Therefore the hexagonal phase CuSe is the crystallites seen in the SEM micrographs 7.5.c and d. This statement was also

shown by EDS analysis. As in the case of these samples the copper was sputtered first, this was the bottom layer in the layer structure, which is probably why some CuSe was present in the samples. This layer structure is either less favourable, or it requires a longer annealing time. Sample 8 also showed a separation of the CIGS and CIS phases. It can be seen from the XRD results that in the cases where there is less Ga in the layer than In the phase separation is more pronounced.

XPS measurements were also performed on sample 8. The binding energies were evaluated using the NIST XPS binding energy database, and are summarized in Table 5.

	Se 3d	In 4d 5/2	Cu 2p 3/2
Sample 8	54.4 eV	444.5 eV	932.5 eV
Reference CIGS sample (own measurement)	54.45 eV	444.6 eV	-
Reference [7.1.] CuInSe ₂	54.3-54.5 eV	444.6-444.8 eV	932.1-932.6 eV
Cu metal (own measurements)			932.35 eV
In metal		443.9 eV	
Se	55.2 eV		

Table 7.5. XPS Binding energies of Se, In and Cu measured on sample 8 and on reference samples

The accuracy of our own measurements is in the range of $\pm 0.1\text{eV}$ (similar to the accuracy of ref.[7.1]). The XPS binding energies are in good agreement with the XRD data and show the presence of CuInSe₂ and CuIn_{0.7}Ga_{0.3}Se₂ phases in sample 8.

As a conclusion this selenization method resulted in more homogeneous depth profiles of the layers, and CIGS layers were formed. On the other hand, even the best layers produced by this method contain additional binary or ternary phases.

7.4 Post selenization of flash evaporated metallic layers

In this experiment a simple flash-like evaporation of the metals combined with a number of different selenization times was used.

Fig. 7.8. shows a secondary electron image of the layer prepared by post selenization of flash-evaporated metals. The CIGS films show the cauliflower-like structure mentioned in the literature [2.1.]. The tetragonal shaped crystallites typical of chalcopyrite structure are also apparent in the image.

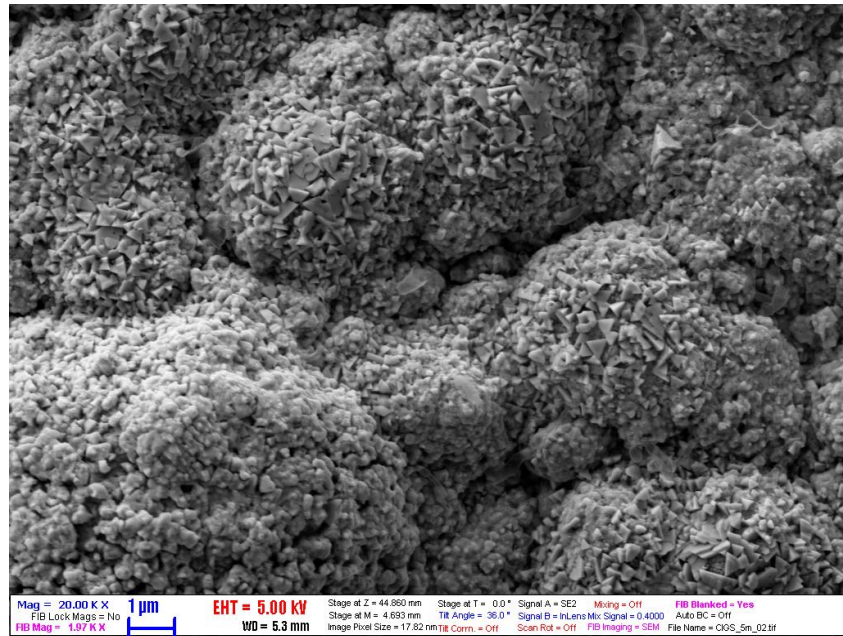


Fig 7.8. The SEM micrograph of the Flash evaporated post selenized (for 15min) layer

Fig. 7.9. shows the SEM images of the CIGS sample selenized at 500° for 15 minutes. The morphology seen in the secondary electron image of Fig 7.9.a shows a much smoother surface than the one in Fig.7.5.a. Systematic examination of the samples showed that already 5 minutes selenization resulted smooth and homogenous layers with -according to the EDS results- a composition that agrees well with the literature required value. Figure 7.9. shows that the element distribution becomes homogenous after 15 minutes of selenization.

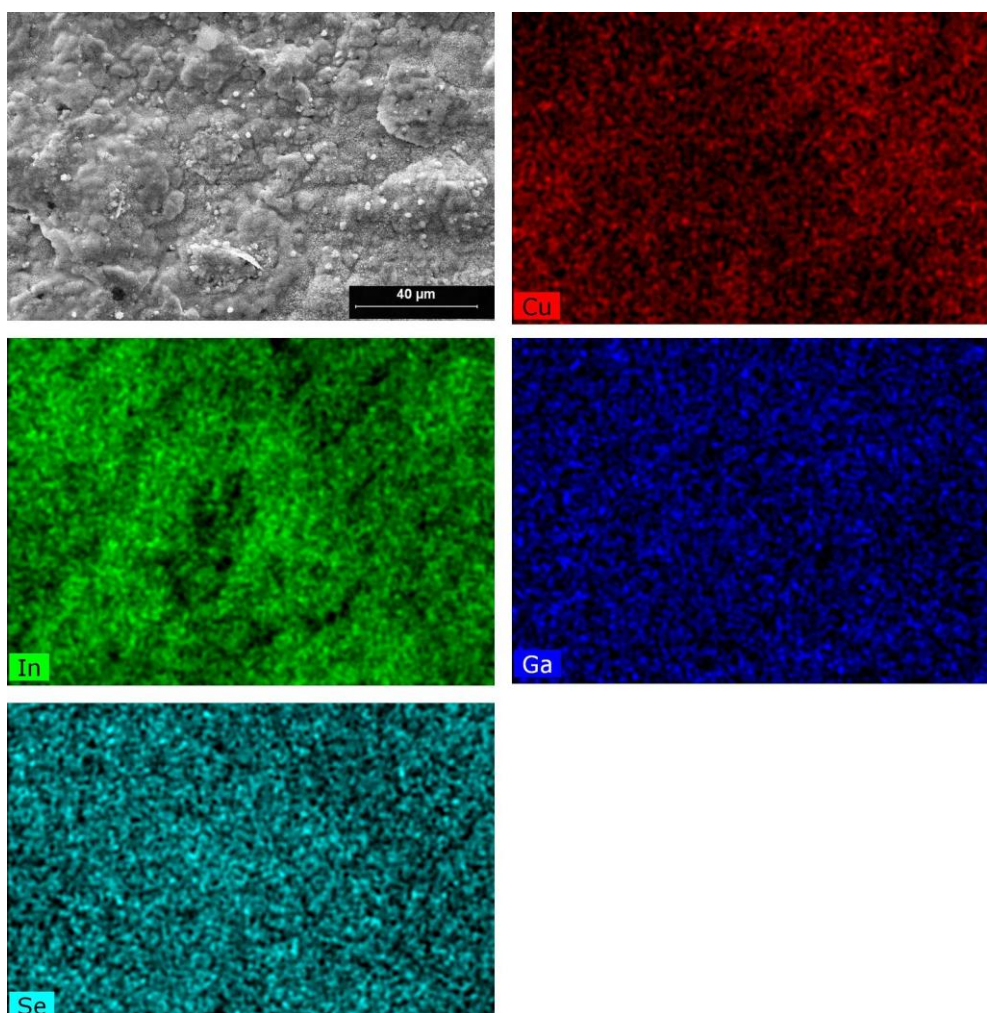


Fig. 7.9. secondary electron image and element distributions of the sample prepared by 15 minutes post selenization of flash evaporated metals.

Fig 7.10. shows the X-ray diffraction results of the flash evaporated and post-selenized samples (sample numbers 9-12). All the samples in the figure were selenized at 500° for different lengths of time between 5 and 20 minutes. It can be seen in fig 7.10.a that all the samples showed only the diffraction peaks for the chalcopyrite structure, no oxides or selenides are visible. Fig 7.9.b is an enlarged part of the previous image, and shows the (204/220) peak of the samples. It is apparent that the only difference depending on the selenization time is the Ga/In ratio. The peak that corresponds to the $\text{CuIn}_{0.7}\text{Ga}_{0.3}\text{Se}_2$ composition has a slightly smaller lattice constant, and the ionic radius of the Ga is smaller within the chalcopyrite crystal. Therefore some caution must be taken, as it is also possible, that the crystal lattice constant has been enlarged by another effect as well.

According to the XRD results the composition of all the samples is between $\text{CuIn}_{0.9}\text{Ga}_{0.1}\text{Se}_2$ and $\text{CuIn}_{0.7}\text{Ga}_{0.3}\text{Se}_2$. The ideal composition of the CIGS solar cells is

$\text{CuIn}_{0.8}\text{Ga}_{0.2}\text{Se}_2$. The samples selenized for 5 and 15 minutes have this ideal composition. The one selenized for 10 minutes has a somewhat lower Ga content, while the 20 minute sample has the composition of $\text{CuIn}_{0.7}\text{Ga}_{0.3}\text{Se}_2$.

It is interesting to note, that the samples prepared by this method show no phase separation. Although the amount of Ga also varies here, every sample contains only one phase, with a given Ga ratio.

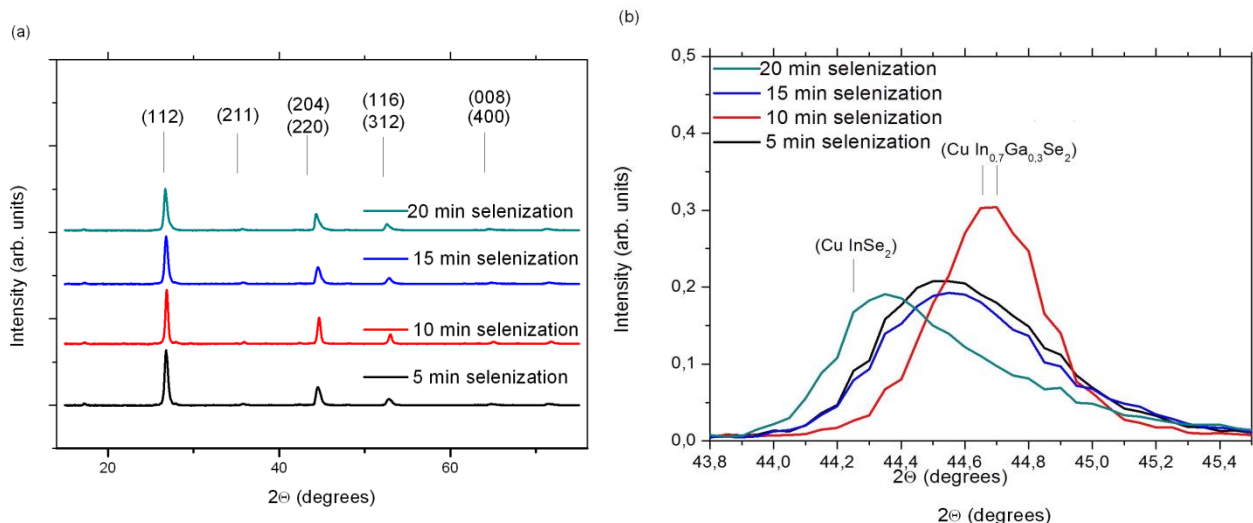


Fig. 7.10. XRD results of the post-selenized CIGS layers at 500°

The SNMS results presented in Fig. 7.11. show the depth profiles of the layers. The surface of these layers is also very rough. As the sputtering speed varies with the changing morphology, and the islands and the surface between them are sputtered simultaneously, a widening of the depth profiles can be seen in the image. Therefore it is only possible to give an approximation of the depth distribution of the elements. It has been mentioned in the literature [2.1.] that the main drawback of the post-selenization method is that the thus created CIGS layers tend to have excess Ga near the back contact of the layers, which decreases the efficiency of the solar cell. The SNMS results of our samples on the other hand showed no sign of this effect, their composition is mostly uniform throughout the film

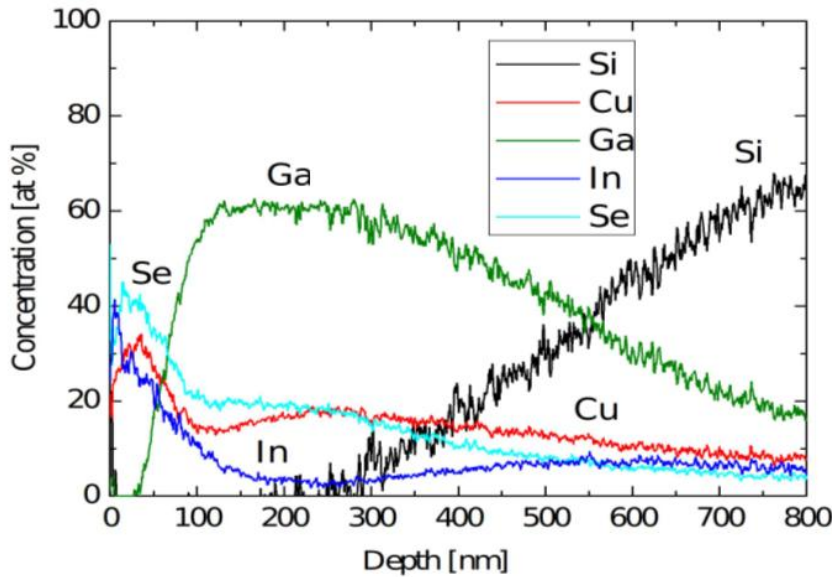


Fig. 7.11 The SNMS depth profile of the Flash evaporated and post-selenized layer

As a conclusion the evaporation order has a decisive effect on the resulting layers in the case of consecutively evaporated layers. The ones with the Cu on top always result in better CIGS layers with both selenization methods. The reason for this phenomenon is probably the better diffusion of both In and Ga in a Cu rich environment. On the other hand the sputtering ensures a better alloying of the components due to the high temperatures during sputtering and that the high energy Cu atoms transfer their energy to the low melting In atoms, resulting in a better mixing. It is interesting that when the In sublayer is above the Ga film more CIS is present. On the other hand CGS phase was never found in the layers, not even when the Ga was on top. The reason for this is that the In atoms diffused towards the Se rich surface in all cases, resulting in a more homogeneous structure. Therefore the optimal sequence is: In, Ga, Cu, and post-selenization with Se vapour.

I found that the evaporation of Se and a subsequent annealing is not sufficient for all the reactions to take place that would result in a homogeneous CIGS layer. The selenization must be performed as an annealing in Se vapour.

A great advantage of the flash evaporation method is its simplicity and cost efficiency. The resulting layers with this method are homogenous CIGS films with the required composition and crystalline structure, the rough morphology has no negative effect on the morphology and structure of the final CIGS layers. The Ga concentration was found to be uniform throughout the whole thickness which makes the fabrication of good quality devices possible. However, as the mechanical stability of the layers was not adequate, the device fabrication has not succeeded yet.

Summary

In my work I studied thin layers of two materials: ZnO and CIGS which are both extremely important for a number of optoelectronic and photovoltaic applications. I examined the dependence of the crystallinity of ALD ZnO on the deposition temperature and the Al doping at the same time. In agreement with the literature I found that the ZnO films on Si and glass are polycrystalline, and have a preferred orientation as a function of the deposition temperature. I determined that the orientation changes from (100) to (001) with the increasing temperature. The effect of the Al doping on the crystallinity at different deposition temperatures has not been studied previously. The Al doping reduces the crystallinity of the layers, decreases the grain size and induces strains in the film. The best crystallinity in doped layers is resulted by a 2 at% Al doping.

At the same time I also studied the effect of Al doping on the resistivity of the films. I found that Al is incorporated in ZnO mostly in the form of Al_2O_3 . The doping efficiency depends on the temperature and results in the best conductivity at 210°C deposition temperature, and 2 at% Al concentration. The carrier concentration has a maximum in this range while the mobility monotonously decreases with the doping. I found no correlation between the resistivity and the orientation and their dependence on the deposition temperature, therefore I concluded that the conductivity is not grain boundary dominated.

Studying the nucleation mechanisms on different substrates I found that ALD ZnO exhibits a layer by layer growth on sapphire and GaN substrates, and an island-like growth on Si. The reason for the latter is a seed formation issue on the SiO_x surface. An extra long first pulse can solve this problem by saturating the surface with smaller islands already in the first nucleation cycle. As the thus achieved films have a smaller surface roughness, the growth of thinner continuous layers is also possible with this method.

I concluded that besides the surface chemical reactions the temperature dependence of the growth rate of ALD ZnO on Si is caused by the orientation. At higher temperatures the steric hindrance of the neighbouring adsorbate molecules results in their reconfiguration in the next closest packing structure. I have also shown that the difference of the growth rates on different substrates is a result of the different morphologies. The layers grown on Si have a higher roughness, therefore a larger specific surface, which yields a higher rate of adsorption.

On GaN the growth always occurs layer by layer and an epitaxial growth is also possible with proper deposition parameters. The growth type on sapphire can be tuned by the deposition temperature.

Using these results I deposited epitaxial ZnO layers and found that the epitaxy is possible on GaN substrates above 270°C deposition temperature. Lower temperature epitaxial growth is also possible by the introduction of an epitaxial buffer layer. All the epitaxial films had high conductivities. This was resulted by the

high mobility due to the excellent crystalline structure and the high carrier concentrations. The latter is caused by the diffusion of Ga atoms into the layer, therefore the Al doping cannot further reduce the resistivity. In the case of the Al doped layers small domains with a different orientation also appeared.

The other focus of my work was to deposit CIGS films with the post-selenization of the metallic components. Two different evaporation methods, and two post-selenization methods have been examined. The effect of the different morphologies and the selenization on the CIGS structure were compared.

The consecutively evaporated layers in my experiments were much thicker than the flash evaporated ones, therefore I had a chance to examine how thick layers could be selenized reliably. Layers with around 1.5 μm thickness can easily be prepared with the post-selenization method, which is ample for solar cell purposes. The order of the evaporation had a decisive effect on the resulting layers in the case of consecutively evaporated layers. The ones with Cu on top always result in better CIGS layers with both selenization methods. This is partly due to the fact that both In and Ga diffuse better in a Cu rich environment, at the same time the elevated temperature during Cu sputtering makes a mixing of the components possible.

It is interesting that when the In sublayer is above the Ga film more CIS is present. On the other hand CGS phase was never found in the layers, not even when the Ga was on top. The reason for this is that the In diffused towards the Se rich surface in all cases, resulting in a more homogeneous structure.

The evaporation of Se and a subsequent annealing appeared to be insufficient for all the reactions to take place that would result in a homogeneous CIGS layer. The selenization must be performed as an annealing in Se vapour.

The optimal sequence of the materials is: In, Ga, Cu, and post-selenization with Se vapour.

I have also developed a Cu(InGa)Se₂ deposition method using flash-like evaporation of the metals followed by post-selenization. The merit of the method is its simplicity and cost efficiency. The resulting layers were homogenous CIGS films with the required composition and crystalline structure, the rough morphology had no negative effect on the morphology and structure of the final CIGS layers. The Ga concentration was uniform throughout the whole thickness of the film, which makes the fabrication of good quality devices possible. However, as the mechanical stability of the layers was not adequate, the device fabrication has not succeeded so far.

Theses

1. I have shown that the ZnO films on Si and glass are polycrystalline, and have a preferred orientation as a function of the deposition temperature. In case of the 120°C substrate temperature, the (100) orientation is dominant, between 180°C and 210° a mixed orientation is typical, above this the (001) orientation dominates. The change of the orientation means that while at lower temperatures the c axis of the ZnO unit cell is parallel to the substrate; in the layers deposited at higher temperatures the c axis is perpendicular to the substrate surface. The Al doping reduces the crystallinity of the layers, decreases the grain size and induces strains in the film. The best crystallinity in doped layers is resulted by a 2at% Al doping.

Thesis 1. was published in:

T1: Structure and morphology of aluminium doped Zinc-oxide layers prepared by atomic layer deposition: Zs. Baji, Z. Lábadi, Z. E. Horváth, I. Bárszny, Thin Solid Films 520 (2012), 4703. IF: 1.89

2. I have studied the Al doping of ALD ZnO using alternative precursor pulse methods. I have shown that the incorporation of Al occurs mostly in the form of Al₂O₃. The doping efficiency depends on the deposition temperature and has its optimum at 210°C and 2 at% Al concentration. The carrier concentration has a maximum of $2.5 \times 10^{20}/\text{cm}^3$ in this range while the mobility monotonously decreases with the doping. The conductivity is not grain boundary dominated.

I have deposited highly conductive epitaxial ZnO layers on GaN substrates by atomic layer deposition for the first time. The layers grown above 270°C are epitaxial and exhibit low resistivity in the order of magnitude of $10^{-4}\Omega\text{cm}$. Lower temperature epitaxial growth is also possible by the introduction of an epitaxial buffer layer. I have shown that the source of this high conductivity is the Ga doping from the substrate. Additional Al doping deteriorates the quality of the epitaxy.

Thesis 2. was published in:

T2: Temperature dependent in situ doping of ALD ZnO: Zs. Baji, Z. Labadi, Z.E. Horvath, M. Fried, B. Szentpali, I. Barsony, JTAC 105 (1) 93-99 (2011) IF: 1.75

Independent citations: 4

T3: Al doped ALD ZnO for CIGS buffer layer, Zs. Baji , Z. Lábadi , M. Fried K. Vad J. Toth and I. Bárszny, Proc. EUPVSEC, 2011, 2992 - 2997 ISBN: 3-936338-27-2 DOI: 10.4229/26thEUPVSEC2011-3DV.2.26

T4: Microscopy of ZnO layers deposited by ALD, B. Pécz, Zs. Baji, Z. Lábadi, and A. Kovacs, Thin Solid Films, accepted (2013) IF: 1.89

3. I have shown that ALD ZnO exhibits a layer by layer growth on sapphire and GaN substrates, and an island-like growth on Si. The reason for the latter is a seed formation

issue on the SiO_x surface which can be overcome by applying a 10-100 times longer first deposition cycle.

I concluded that besides the surface chemical reactions the temperature dependence of the growth rate of ALD ZnO on Si is caused by the orientation. At higher temperatures the steric hindrance of the neighbouring adsorbate molecules results in their reconfiguration in the next closest packing structure.

I have also shown that the difference of the growth rates on different substrates is a result of the different morphologies of the grown layers. The layers grown on Si have a higher roughness, therefore a larger specific surface, which yields a higher rate of adsorption.

Thesis 3. was published in:

T5: Nucleation and Growth Modes of ALD ZnO, Zs. Baji, Zoltán Lábadi, Z. E. Horváth, G. Molnár, J. Volk, I. Bársony, P. Barna, Cryst. Growth Des., 12. (2012) 5615 IF: 4.7

4. I have developed a Cu(InGa)Se₂ deposition method using a flash-like evaporation of Cu In and Ga followed by post-selenization. The resulting layers are homogenous CIGS films with the required composition and crystalline structure. I found that the rough morphology of the precursor layers has no negative effect on the structure and morphology of the final CIGS layers as the Ga concentration was found to be uniform throughout the whole thickness.

In the case of the consecutively evaporated precursor metals I found that the morphology of the deposited metals has a definitive effect on the resulting CIGS structure. Therefore I determined the optimal order of the precursor metals as: In followed by Ga, then by Cu. The reason for this is that the Cu sputtered in the final step ensures the mixing of the precursors due to the Ga diffusion. On the other hand the Ga evaporated before the In results in a phase separation of the CIS and CIGS materials.

The selenization must be performed as an annealing in Se vapour, as the evaporation of Se and a subsequent annealing is not sufficient for all the reactions that would result in a homogeneous CIGS layer to take place.

Thesis 4. was published in:

T6: Post-selenization of stacked precursor layers for CIGS, Zs. Baji, Z. Lábadi, Gy. Molnár, B. Pécz, A. L. Tóth, J. Tóth, A. Csik, and I. Bársony, Vacuum, 92. (2013) 44 IF: 1.2

Partly related to thesis 4.:

T7: Formation of Nanoparticles by Ion Beam Irradiation of Thin Films, Zs. Baji, A. Szanyo, Gy. Molnár, A. L. Tóth, G. Pető, K. Frey, E. Kotai, and G. Kaptay, Journal of Nanoscience and Nanotechnology 12, (2012) 1. IF: 1.4

Conference presentations:

posters:

- Valence band of In and Gold nanoparticles formed by Ar ion irradiation, Zs. Baji, Cs.S. Daróczi, L. Guczi, Gy. Molnár, A. Karacs, G. Pető, EMRS spring, 2007
- Al doped ALD ZnO for CIGS buffer layer, Zs. Baji , Z. Lábadi , M. Fried K. Vad J. Toth and I. Bárszny, EUPVSEC, 2011
- Structure and morphology of aluminium doped Zinc-oxide layers prepared by atomic layer deposition: Zs. Baji, Z. Lábadi, Z. E. Horváth, I. Bárszny, EMRS spring 2011
- Conductive epitaxial ZnO layers by ALD, Zs. Baji, Z. Lábadi, Zs.E. Horváth, I. Bárszny, EMRS spring 2012
- Surface roughness and interface study by Secondary Neutral Mass Spectrometry, R. Lovics, V. Takáts, A. Csik, J. Hakl, G.A. Langer, Zs. Baji, Z. Lábadi, K. Vad , JVC14, 2012

Oral presentations:

- The nucleation and growth modes of ALD ZnO, MOPNA workshop Budapest, 2011
- Ellipsometric characterisation of porous Si covered with ALD ZNO, EMRS spring, 2012

Further publications not closely related to the subject of this work:

1. Investigations into the Impact of the Template Layer on ZnO Nanowire Arrays Made Using Low Temperature Wet Chemical Growth: Erdelyi R, Nagata T, Rogers DJ, Teherani FH, Horvath ZE, Labadi Z, Baji Zs, Wakayama Y, Volk J CRYST GROWTH DES 11: (6)2515-2519 (2011) IF:4.7
Independent citations: 5
2. Thickness and annealing dependent morphology changes of iron silicide nanostructures on Si(001) G. Molnár, L. Dózsa, Z. Vértesy, Zs. Baji, G. Pető, (2012) DOI:10.1002/pssc.201100662, Copyright (c) 2012 WILEY-VCH Verlag GmbH & Co. KGaA, Weinheim
3. Characterization of ZnO structures by optical and X-ray methods, P. Petrik, B. Pollakowski, S. Zakel, T. Gumprecht, B. Beckho, M. Lemberger, Z. Labadi, Zs. Baji, M. Jank, A. Nutsch, Thin Solid films, <http://dx.doi.org/10.1016/j.apsusc.2012.12.035> (2013) IF 1.89

List of abbreviations

- AFM: Atomic force microscopy
ALD: Atomic layer deposition
CIGS: Cu(In,Ga)(Se,S)₂
CIS: CuInSe₂
CGS: CuGaSe₂
CVD: Chemical vapour deposition
DEZ: Diethyl-zinc
EBSD: Electron backscatter diffraction
EDS: Energy dispersive spectroscopy
FWHM: Full width half maximum
V_{Cu} : Copper vacancy
In_{Cu}: In substitution in a copper vacancy
LED: Light emitting diode
DRIE: Deep reactive ion etching
RSM: Reciprocal space mapping
SEM: Scanning electron microscopy
SNMS: Secondary neutral mass spectrometry
TEM: Transmission electron microscopy
TMA: Trimethyl-aluminium
TFT: Thin film transistor
XRD: X-ray diffraction
XPS: X-ray photoelectron spectroscopy

Acknowledgement

I would like to thank my supervisors, Zoltan Lábadi and György Molnár for all the help and support given during my work. István Bárszny, Gábor Pető, Gábor Battistig, János Volk and Péter Barna for the help and all the good advice.

I would like to express my sincere gratitude to all the colleagues who helped me with the measurements presented in my work: Béla Pécz for the TEM, József Tóth for the XPS, Kálmán Vad for the SNMS, Attila Tóth for the SEM, Miklós Fried for the SE, Dr Zsolt Endre Horváth for the XRD, Péter János Szabó for the EBSD, Takahiro Nagata for the RSM measurements.

I am especially grateful to Michael Walker for carefully reading through my thesis and correcting it.

I am honestly grateful to all my colleagues at the MEMS lab not only for their continual support, but also for the wonderful atmosphere in which we are lucky to work day by day.

Most of all I am indebted to my family. Without their support and patience I could not have done this work. I would especially like to thank my wonderful children, who showed patience and understanding well defying their age.

I would also like to thank the financial support of the Hungarian National Science Fund OTKA grant No. NK73424 and the National Development Agency grant TÁMOP-4.2.2/B-10/1-2010-0025.

References

- 1.1. Martin A. Green, Keith Emery, Yoshihiro Hishikawa, Wilhelm Warta, Ewan D. Dunlop, (Solar cell efficiency tables version 39) *Prog. Photovolt: Res. Appl.* 20. (2012)12.
- 1.2. A. Janotti, C.G. Van de Walle, Fundamentals of ZnO as a semiconductor, *Rep.Prog.Phys.* 72 (2009) 126501
- 1.3. D. Hariskos, S. Spiering, M. Powalla, Buffer layers in Cu(In,Ga)Se₂ solar cells and modules, *Thin Solid Films*, 480 (2005) 99.
- 2.1.1. S. Haukka, T. Suntola, Advanced Materials Processing by Adsorption Control, *Interface Science* 5, 119–128 (1997) Kluwer Academic Publishers
- 2.1.2. M. Leskela, M. Ritala, Atomic Layer Deposition Chemistry: Recent Developments and Future Challenges, *Angew. Chem.*, 2003, 42, 5548
- 2.1.3. S.M. George, Atomic Layer Deposition: An Overview, *Chem. Rev.* 110 (2010):111
- 2.1.4. M. Leskela, M. Ritala, Atomic Layer Deposition (ALD) : from precursors to thin film structures
- 2.1.5. M. Ritala, M. Leskela, Atomic Layer Deposition, *Handbook of Thin Film Materials*, edited by H.S. Nalwa, Vol.1. 2002 Academic press
- 2.1.12. M. Ritala, M. Leskela, Atomic Layer Epitaxy in Deposition of Various Oxide and Nitride Thin Films, *JOURNAL DE PHYSIQUE IV Colloque C5*, supplément au Journal de Physique 11, Volume 5, juin 1995
- 2.1.6. J.W. Elam, G. Xiong, C. Y. Han, H. H. Wang, J.P. Birrell, U. Welp, et al. Atomic layer deposition for the conformal coating of nanoporous materials *Journal of Nanomaterials*, Vol. 2006, article ID. 64501, p.1.
- 2.1.7. B. H. Kong, M. K. Choi, H. K. Cho, J. H. Kim, S. Baek, and J.Ho Leec Conformal Coating of Conductive ZnO:Al Films as Transparent Electrodes on High Aspect Ratio Si Microrods, *Electrochemical and Solid-State Letters*, 13 2010 K12-K14
- 2.1.8. J.W. Elam, D. Routkeahvitch, P. P. Mardilovich, S. M. George, Conformal Coating on Ultrahigh-Aspect-Ratio Nanopores of Anodic Alumina by Atomic Layer Deposition, *Chem. Mater.* 2003, 15, 3507.
- 2.1.9. M. Ylilammi, Mono-layer thickness in ALD, *Thin Solid Films* 279 (1996) 124.
- 2.1.10. R. Puurunen, Surface Chemistry of atomic layer deposition: A case study for the trimethylaluminum/water process, *J. Appl. Phys.* 97, (2005) 121301
- 2.1.11. J. Ihanus, M. Ritala, M. Leskela, T. Prohaska, R. Resch, G. Friedbacher, M. Grasserbauer, AFM studies on ZnS thin films grown by atomic layer epitaxy *Appl. Surf. Sci.*, 120, (1997) 43.
- 2.1.14. T. Nam, J.-M. Kim, M.-K. Kim, H. Kim, W.-H. Kim, Low-temperature Atomic Layer Deposition of TiO₂, Al₂O₃, and ZnO Thin Films, *Journal of the Korean Physical Society*, 59 (2011) 452.
- 2.1.15. M. D. Groner, F. H. Fabreguette, J. W. Elam, S. M. George, Low-Temperature Al₂O₃ Atomic Layer Deposition, *Chem. Mater.* 16, (2004) 639
- 2.1.16. J. W. Elami, Z. A. Sechrist, S.M. George, *Thin Solid Films*, 414 (2002), 43.
- 2.1.17. H. Kim, H.-B.-R. Lee, W.-J. Maeng, Applications of atomic layer deposition to nanofabrication and emerging nanodevices, *Thin Solid Films* 517 (2009) 2563.

- 2.1.18 M. Leskelä, M. Kemell, K. Kukli, V. Pore, E. Santala, M. Ritala, Jun Lu, Exploitation of atomic layer deposition for nanostructured materials, Materials Science and Engineering C 27 (2007) 1504.
- 2.1.19 B. Min, J.S. Lee, J.W. Hwang, K.H. Keem, M.I. Kang, K. Cho, M.Y. Sung, S. Kim, M-S. Lee, S.O. Park, J.T.Moon, Al₂O₃ Coating of ZnO nanorods by atomic layer deposition, J. of Crystal Growth, 252 (2003) 565.
- 2.1.20 I. Alessandri, M. Zucca, M. Ferroni, E. Bontempi, L. E. Depero, Growing ZnO Nanocrystals on Polystyrene Nanospheres by Extra-Low-Temperature Atomic Layer Deposition, Crystal Growth and Design 9. (2009) 1258.
- 2.1.21 I.M. Povey, M. Bardosova, F. Chalvet, M.E. Pemble, H.M. Yates, Atomic layer deposition for the fabrication of 3D photonic crystals structures: Growth of Al₂O₃ and VO₂ photonic crystal systems, Surface & Coatings Technology 201 (2007) 9345
- 2.2.1 Zinc Oxide Bulk, Thin Films and Nanostructrues, edited by Chennupati Jagadish and Stephen J. Pearton (2006), Elsevier
- 2.2.2 Ü. Özgür, Ya.I. Alivov, C. Liu, A. Teke, M.A. Reshchikov, S. Dogan, V. Avrutin, S.-j. Cho, H. Morkoc, A comprehensive review of ZnO materials and devices, J. of Appl. Phys. 98. (2005) 041301
- 2.2.3 R.J. Lad, O.D. Funkenbusch, C.R. Aita, Postdeposition annealing behavior of rf sputtered ZnO films, J. Vac.Sci.Technol, 17. (1980) 808.
- 2.2.4 T. Krajewski, E. Guziewicz, M. Godlewski, L. Wachnicki, I.A. Kowalik, A. Wojcik-Glodowska, M.Lukasiewicz, K.Kopalko, V. Osinniy, M. Guziewicz, The influence of growth temperature and precursors' doses on electrical parameters of ZnO thin films grown by atomic layer deposition technique, Microel. J. 40 (2009) 293.
- 2.2.5 K.Kopalko, M. Godlewski, E. Guziewicz, E. Lusakowska, W. Paszkowicz, J. Domagala, E. Dynowska, A. Szczerbakow, A. Wojcik, M.R. Phillips, Monocrystallinte thin films of ZnSe and ZnO grown by atomic layer epitaxy, Vacuum, 74. (2004) 269.
- 2.2.7 V.Talyansky, S.Choopun, R. P.Sharma, T. Venkatesan, M.He, X. Tang, J. Y. X. Li, L. G. Salamanca-Riba, A. A Iliadis,, K. A Jones, Heteroepitaxy of ZnO on GaN and its implications for fabrication of hybrid optoelectronic devices Appl. Phys. Lett. 73, (1998) 348
- 2.2.8 P.S.Nayar, Properties of conducting zinc oxide films prepared by R.F. Sputtering, Journal of Electronic Materials 6 (1982) 967.
- 2.2.9 Yasuhiro Igasaki, Takashi Naito, Kenji Murakami, Waichi Tomoda, The effects of deposition conditions on the structural properties of ZnO sputtered films on sapphire substrates, Applied Surface Science 169. (2001) 512.
- 2.2.10 Ji Zhao, L. Hu, Z. Wang, Z. Wang, H. Zhang, Y. Zhao, X. Liang, Epitaxial growth of ZnO thin films on Si substrates by PLD technique, 280. (2005) 455.
- 2.2.11 A. El-Shaer, A. C. Mofor, A. Bakin, M. Kreye, A. WaagHigh-quality ZnO layers grown by MBE on sapphire 38. (2005) 265.
- 2.2.12 I.A. Kowalik, E. Guziewicz, K. Kopalko, S. Yatsunenko, A. Wójcik-Godłowska, M. Godlewski, P. Dluzewski, E. Lusakowska, W. Paszkowicz, Structural and optical properties of low-temperature ZnO films grown by atomic layer deposition with diethylzinc and water precursorsJ. Cryst. Growth 311. (2009) 1096.
- 2.2.13 H. Zhou, M. Wissinger, J. Fallert, R.Hauschild, F. Stelzl, C. Klingshirn, H. Kalt, Ordered, uniform-sized ZnO nanolaser arrays, Appl. Phys. Lett. 91, (2007) 181112.

- 2.2.14 R. Triboulet, J. Perrière, Epitaxial growth of ZnO films, *Prog. Crys. Growth and Char. Mat.* 47. (2003) 65.
- 2.2.15 S. J. Pearton, D.P. Norton , K. Ip, T. W. Heo, T. Steiner, Recent progress in processing and properties of ZnO Superlattices *Microstruct.* 34 (2003) 3.
- 2.2.16 A. Janotti, C.G. Van de Walle, Oxygen vacancies in ZnO, *Appl. Phys. Lett.* 87.(2005) 122102.
- 2.2.17 D.M. Hofman, A. Hofstaetter, F. Leitet, H Zhou, F. Henecker, B.K. Meyer, Hydrogen: A relevant shallow donor in Zinc Oxide, *Phys.Rev. Lett.* 88. (2002) 4.
- 2.2.18 S.F.J. Cox, E.A. Davis, S.P. Cottrell, P.J.C.King, J.S. Lord, J.M. Gil, H.V. Alberto, R.C.Vilao, J.P. Duarte, N.Ayres de Campos, A. Weidinger, R.L.Lichti, S.J.C. Irvine, Experimental confirmation of the predicted shallow donor hydrogen state in Zinc Oxide, *Phys.Rev.Lett.* 86. (2001) 12.
- 2.2.19 C.G. Van de Walle, Hydrogen as a cause of doping in Zinc Oxide, *Phys.Rev.Lett*, 85. (2000) 5.
- 2.2.20 S.D. Kirby, R.B van Dover, Improved conductivity of ZnO through codoping with In and Al, *Thin Solid Films* 517 (2009) 1958-1960.
- 2.2.21 U. Grossner, S. Gabrielsen, T. M. Borseth, J. Grissenberger, A.Y. Kuznetsov, B.B. Svensson, Palladium Schottky barrier contacts to hydrothermally grown n-ZnO and shallow electron states, *Appl. Phys. Lett.* 85. (2004) 2259.
- 2.2.22 A. Yamada, B.Sang, M.Konagai, Atomic layer deposition of ZnO transparent conducting oxides, *Appl. Surf. Sci.* 112 (1997) 216.
- 2.2.23 J.W. Elam, Z.A. Sechrist, S.M. George, ZnO/Al₂O₃ nanolaminates fabricated by atomic layer deposition: growth and surface roughness measurements, *Thin Solid Films*, 414. (2002) 43.
- 2.2.24 H.C. Chen, M.J. Chen, T.C. Liu, J.R. Yang, M. Shiojiri, *Thin Solid Films* 519 (2010) 536
- 2.2.25 L. Wachnicki, T. Krajewski, G. Luka, B. Witkowski, B. Kowalski, K. Kopalko, J.Z. Domagala, M. Guziewicz, M. Godlewski, E. Guziewicz, Monocrystalline zinc oxide films grown by atomic layer deposition *Thin Solid Films* 518 (2010) 4556
- 2.2.26 J. Lim, K. Shin, H. Woo Kim, C. Lee, Effect of annealing on the photoluminescence characteristics of ZnO thin films grown on the sapphire substrate by atomic layer epitaxy *Materials Science and Engineering B* 107 (2004) 301
- 2.2.27 C.-W. Lin, D.-J. Ke, Y.-C. Chao, L. Chang, M.-H. Liang, Y.-T. Ho, Atomic layer deposition of epitaxial ZnO on GaN and YSZ *Journal of Crystal Growth* 298 (2007) 472
- 2.2.28 E. H. Kim, D. H. Lee, B. H. Chung, H. S. Kim, Y. Kim and S. J. Noh, Low-Temperature Growth of ZnO Thin Films by Atomic Layer Deposition, *Journal of the Korean Physical Society*, 50. (2007) 1716
- 2.2.29 J.Lim, C. Lee, Effects of substrate temperature on the microstructure and photoluminescence properties of ZnO thin films prepared by atomic layer deposition *Thin Solid Films* 515 (2007) 3335.
- 2.2.30 S. J.Lim, S.Kwon, H. Kim, ZnO thin films prepared by atomic layer deposition and rf sputtering as an active layer for thin film transistor, *Thin Solid Films* 516 (2008) 1523
- 2.2.31 A.Wójcik, M.Godlewski, E.Guziewicz, R.Minikayev, W.Paszkowicz, Controlling of preferential growth mode of ZnO thin films grown by atomic layer deposition, *J. Cryst. Growth.* 310 (2008) 284.
- 2.2.32 M.Godlewski, E.Guziewicz, G.Luka, T.Krajewski, M.Lukasiewicz, L.Wachnicki,

- A.Wachnicka, K.Kopalko, A.Sarem, B.Dalati ZnO layers grown by Atomic Layer Deposition: A new material for transparent conductive oxide, Thin Solid Films; 518 (2009) 1145.
- 2.2.33 S.K. Kim, C.S.Hwang, S.-H. K. Park, S.J.Yun, Comparison between ZnO films grown by atomic layer deposition using H₂O or O₃ as oxidant, Thin Solid Films 478. (2005) 103.
- 2.2.34 M. Schuisky, J.W. Elam, S.M.George, In situ resistivity measurements during the atomic layer deposition of ZnO and W thin films
- 2.2.35 B.-Y.Oh, J.H.Kim, J.-W. Han, D-S. Seo, H. S. Jang, H.-J. Choi, S.-H. Baek, J H. Kim, G-S. Heo, T.-W. Kim, K.-Y. Kim, Transparent conductive ZnO:Al films grown by atomic layer deposition for Si-wire based solar cells, Curr. Appl. Phys. (2011) 1 Doi: 10.1016/j.cap.2011.06.017
- 2.2.36 H. Saarenpaa, T. Niemi, A Tukiainen, H. Lemmetyinen, N. Tkachenko, Aluminum doped ZnO films grown by atomic layer deposition for organic photovoltaic devices, Sol En. Mater, 94 (2010) 1379.
- 2.2.37 J.W.Elam, S.M. George, Growth of ZnO/Al₂O₃ alloy films using atomic layer deposition techniques, Chem.Mater, 15. (2003) 1020.
- 2.2.38 J. Han, P.Q.Mantas, A.M.R.Senos, Effect of Al and Mn doping on the electrical conductivity of ZnO, J. Eur. Ceram. Soc. 21. (2001) 1883.
- 2.2.39 C. H. Ahn, H.Kim, H.K. Cho, Deposition of Al doped ZnO layers with various electrical types by atomic layer deposition, Thin Solid Films; 519 (2010) 747.
- 2.2.40 C.R.Kim, J.Y. Lee, J.H. Heo, C.M. Shin, T.M. Lee, J. H. Park, H.Ryu, J.H Chang, C.S. Son, Effects of annealing temperature and Al₂O₃ buffer layer on ZnO thin films grown by atomic layer deposition, Curr . Appl. Phys. 10. (2010) s298.
- 2.2.41 S.Yang, B.H. Lin, W.R. Liu, J.H.Lin, C.C.Chang, C.H. Hsu, W.F. Hsieh, Structural characteristics and annealing effect of ZnO epitaxial films grown by atomic layer deposition, Crystal growth and design, 9. (2009) 5184.
- 2.2.42 C.H Ahn, C.H. Woo, S.Y.Hwang, J.Y.Lee, H.K, Cho, H.J.Cho, G.Y.Yeom, Influence of active layer thickness and annealing in zinc oxide TFT grown by atomic layer deposition, Surf. Interface Anal. 42. (2010) 955.
- 2.2.43 G. Luka, L. Wachnicki, B.S. Witkowski, T.A.Krajewsi,R.Jakiela, E.Guziewicz, M. Godlewski, The uniformity of Al distribution in aluminium-doped zinc oxide films grown by atomic layer deposition, Mat. Sci. Eng. B, 176. (2011) 237.
- 2.3.1 K.L. Chopra, S.R. Das, Thin Film Solar Cells, Springer, 1983
- 2.3.2 M.E.Beck, R. Butcher, I. Repins, N. Gomez, B. Joshi, R.G. Wendt, J.S.Britt, CIGS module development on flexible substrates, Proc. of the 29th IEEE Photovoltaic Specialists Conference (2002) 575
- 2.3.3 T. Nakada, T. Kume, T. Mise, A. Kunioka, Superstrate-type Cu(In,Ga)Se₂ thin film solar cells with ZnO buffer layers, Jpn. J. Appl. Phys. 37. (1998), 499.
- 2.3.4 R. Klenk, M. C. Lux-Steiner, Chalcopyrite based solar cells in Thin Film Solar Cells Fabrication, Characterization and Applications, Edited by Jef Poortmans and Vladimir Arkhipov, Wiley, 2006
- 2.3.5 N.Cooray, K. Kushiya, A. Fujimaki, D. Okumura, M. Sato, M. Ooshita,O. Yamase, Optimization of Al-doped ZnO Window Layers for Large-Area Cu(InGa)Se₂-Based Modules by RF/DC/DC Multiple Magnetron Sputtering, Jpn. J. Appl. Phys., 38. (1999) 6213

- 2.3.6 N.G. Dhere, Present status and future prospects of CIGSS thin film solar cells, *Sol En Mat Sol Cells*, 90(2006) 2181
- 2.3.7 J.H. Scofield, S. Asher, D. Albin, J. Tuttle, M. Contreras, D. Niles, R. Reedy, A. Tennant, R. Noufi, Sodium diffusion, selenization and microstructural effects associated with various molybdenum back contact layers for CIS-based solar cells, *Proc. of the 24th IEEE Photovoltaic Specialists Conference* (IEEE, New York, 1995), 164.
- 2.3.8 C. Sutichai, S. Takeshi, Y. Akira, K. Makoto, Cu(InGa)Se₂ thin film solar cells with high resistivity ZnO buffer layers deposited by atomic layer deposition, *Jpn. J. Appl. Phys.* 38. (1999) 4989.
- 2.3.9 X. Donglin, L. Jangzhuang, X. Man, Z. Xiujuan, Electrodeposited and selenized CIGS thin films for solar cells, *J. non crystalline solids* 354. (2008) 1447.
- 2.3.10 U. Rau, H.W. Schock, Electronic properties of Cu(In,Ga)Se₂ heterojunction solar cells—recent achievements, current understanding, and future challenges, *Appl. Phys. A* 69, (1999) 131.
- 2.3.11 R. A. Mickelsen, W.S. Chen, High photocurrent polycrystalline thin-film CdS/CuInSe₂ solar cell, *23 Appl. Phys. Lett.* 36. (1980) 371
- 2.3.12 T. Dullweber, G. Hanna, U. Rau, H.W. Shock, A new approach to high-efficiency solar cells by band gap grading in Cu(InGa)Se₂ chalcopyrite semiconductors, *Sol. En. Mat and Sol. Cells*, 67. (2001) 145.
- 2.3.13 G. Hanna, A. Jasenek, U. Rau, H.W. Schock, Influence of the Ga-content on the bulk defect densities of Cu(In,Ga)Se₂, *Thin Solid Films*, 387. (2001) 71.
- 2.3.14 W. Liu, J.-G. Tian, Q. He, F-Y. Li, C.-J. Li, Y. Sun, Effect of metallic precursors on the thin film thickness and reaction resistances in the selenization process, *Curr. Appl. Phys.* 11. (2011) 327.
- 2.3.15 Miguel A. Contreras , Manuel J. Romero, R. Noufi, Characterization of Cu(In,Ga)Se₂ materials used in record performance solar cells, *Thin Solid Films* 511 – 512 (2006) 51
- 2.3.16 P. Jackson, D. Hariskos, E. Lotter, S. Paetel, R. Wuertz, R. Menner, W. Wischmann, M. Powalla, New world record efficiency for Cu(In,Ga)Se₂ thin-film solar cells beyond 20%, *Prog. In Photovolt* 19 (2011) 894.
- 2.3.17 M.A. Contreras, B. Egaas, K. Ramanathan, J. Hiltner, A. Swartzlander, F. Hasoon, R. Noufi, Progress toward 20% efficiency in Cu(In,Ga)Se₂ polycrystalline thin-film solar cells, *Prog. Photovolt.* 7 (1999) 311.
- 2.3.18 M. S. Sadigov, M. Ozkan, E. Bakaksiz, M. Altunbas, A.I. Kopya. Production of CuInSe₂ thin films by a sequential processes of evaporation and selenization, *J. Mat science* 34. (1999) 4579.
- 2.3.19 F. Kang, J. Ao, G. Sun, W. He, Y. Sun, Structure and photovoltaic characteristics of CuIn Se₂ thin films prepared by pulse-reverse electrodeposition and selenization process, *Journal of Alloys and compounds* 478 (2009) L25.
- 2.3.20 M.Kaelin, D. Rudmann, F. Kurdesau, H. Zogg, T. Meyer, A.N. Tiwari, Low-cost CIGS solar cells by paste coating and selenization, *Thin solid* 480 (2005) 486
- 2.3.21 G. Norsworthy, C.R. Leidholm, A. Halani, V.K. Kapur, R. Roe, B.M. Basol, R. Matson, CIS film growth by metallic ink coating and selenization *Sol En. Mat& Solar cells* 60. (2000) 127.
- 2.3.22 D.L. Schultz C.J. Curtis, A. Cram, J.L. Alleman, A. Mason, R.J. Matson, J.D.Perkins, D.S.

- Ginley, Cigs films via nanoparticle spray deposition attempts at densifying a porous precursor, proc of the 26th IEEE, new york,1997 p.483
- 2.3.23 C.-Y. Su, W.-H. Ho, H.-C. Lin, C.-Y. Nieh, S.-C. Liang, The effects of the morphology on the CIGS thin films prepared by CuInGa single precursor, Sol. Energy Mater. Sol. Cells, 95 (2011) 261-263
- 2.3.24 O.F. Gremenok, E.P. Zaretskaya, V.B. Zalesski, K. Bente, W. Schmitz, R.W. Martin, H. Moller, Preparation of Cu(In,Ga)Se₂ thin film solar cells by two-stage selenization processes using N₂ gas, Sol En Mat &Sol Cells, 89 (2005) 129
- 2.3.25 S. D. Kim, H. J. Kim, K. H. Yoon, J. Song, CIS film growth by metallic ink coating and selenization, Sol En Mat &Sol Cells 62. (2000) 357.
- 2.3.26 E.P. Zaretskaya et al. Thin Solid films 515 (2007) 5848
- 2.3.27 J. Hedström, H. Ohlsen, M. Bodegard, A. Kylnér, L. Stolt, D. Hariskos, M. Ruckh, H.W. Schock: In Proc. 23rd IEEE Photovolt. Spec. Conf. (IEEE, New York 1993) p. 364
- 2.3.28 O. Volobujeva, J. Kois, R. Traksmaa, K. Muska, S. Bereznev, M. Grossberg, E. Mellikov Influence of annealing conditions on the structural quality of CuInSe₂ thin films, Thin Solid Films 516 (2008) 7105
- 2.3.29 N.Dhere, K.W. Lynn, Culn_{1-x}Ga_xSe₂ thin film solar cells by two-selenizations process using Se vapour, Sol En Mat &Sol Cells 41. (1996) 271.
- 2.3.30 E.P. Zaretskaya et al., Properties of Cu(In,Ga)(S,Se)₂ thin films prepared by selenization/sulfurization of metallic alloys, Thin Solid films 515 (2007) 5848
- 2.3.31 F.B.Dejene, The structural and material properties of CuInSe₂ and Cu(In,Ga)Se₂ prepared by selenization of stacks of metal and compound precursors by Se vapor for solar cell applications, Sol. En. Mat. and Sol. Cells 93. (2009) 577.
- 2.3.32 R. Kamada, W. N. Shafarman, R.W. Birkmire, Sol. En. Mat. and Sol. Cells 94 (2010) 451
- 2.3.33 M. Sugiyama, A. Kinoshita, M. Fukaya, H. Nakanishi, S.F. Chichibu, Growth of single-phase CuInGaSe₂ photo-absorbing alloy films by the selenization method using diethylselenide as a less-hazardous Se source, Thin solid films 515 (2007) 5867
- 2.3.34 W. Liu, J.-G. Tian, Q. He, F.-Y. Li, C.-J. Li, Y. Sun, In-situ electrical resistance measurement of the selenization process in the CuInGa-Se system, Thin Solid Films 519 (2010) 244
- 2.3.35 M. Sugiyama, F.B.Dejene, A. Kinoshita, M. Fukaya, V. Alberts, H. Nakanishi, S.F. Chichibu, Use of diethylselenide for the preparation of CIGS films by selenization of metal precursors premixed with Se, Phys. Stat. Solidi C, 3. (2006) 2543.
- 2.3.36 V. Probst, W. Stetter, W. Riedl, H. Vogt, M. Wendl, H. Calwer, S. Zwigart, K.-D. Ufert, B. Freienstein, H. Cerva, F.H. Karg, Rapid CIS-process for high efficiency PV- modules: development towards large area processing, Thin Solid Films, 387 (2001) 262.
- 2.3.37 S.Y. Kim, J.H. Kim, Fabrication of CIGS thin films by using spray pyrolysis and post-selenization, J. Korean Phys. Soc, 60. (2012) 2018.
- 2.3.38 E. Ahmed, A. Zegadi, A.E. Hill, R.D. Pilkington, R.D. Tomlinson, W. Ahmed, Thermal annealing of flash evaporated Cu(InGa)Se₂ thin films, J Mat. Proc. Technol. 77. (1998) 260.
- 2.3.39 T.W. Kim, Y.-B. Kim, S.I. Song, C.-W. Jung, J.-H. Lee, Characteristics of CIGS thin films prepared by RF sputtering employing CIGS single target, Proc. SPIE 8110, Thin film Solar Technology III 811008 (2011)

- 2.3.40 AC. Rastogi, K.S. Balakrishnan, R.K. Sharma, K. Jain, Growth phases during electrochemical selenization of vacuum deposited CuIn metal layers for the formation of semiconducting CuInSe₂ films Thin Solid Films, 357 (1999) 179.
- 4.1 S. Kohiki, M. Nishitani, T. Negami, T. Wada, X-ray photoelectron spectroscopy of CuInSe₂ Phys. Rev. B 45. (1992) 9163,
- 5.1 S. Haukka, A. Roots, J. Phys. Chem. 1994, 98, 6.
- 5.2 X. Wang, S. M. Tabakman, H. Dai, J. AM. CHEM. SOC. 2008, 130, 8152
- 5.3 H. Alles, J. Aarik, J. Kozlova, A. Niilisk, R. Rammula V. Sammelselg, Graphene - Synthesis, Characterization, Properties and Applications, Edited by Jian Ru Gong, ISBN 978-953-307-292-0, InTech, 2011. DOI: 10.5772/20801
- 6.1 V.J. Norman, The diffusion of aluminium and gallium in zinc oxide, Australian Journal of Chemistry 22(2) (1969) 325.